Claudia Kieler, BSc

Biological Activity of a Pt(II) Metallacycle Aimed at Targeting G-Quadruplex Nucleic Acids

MASTER'S THESIS

to achieve the university degree of

Diplom-Ingenieurin

Master's degree programme: Biotechnology

submitted to

Graz University of Technology

Supervisor

Ao.Univ.-Prof. Dipl.-Ing. Dr.techn. Murkovic, Michael

Institute of Biochemistry

Graz, October 2019

MEDIZINISCHE UNIVERSITÄT WIEN

The Master's Thesis was conducted at the

Medical University of Vienna

Department of Medicine I
Institute of Cancer Research

Applied and Experimental Oncology

And was supervised by

Univ. Prof. Dr. Walter Berger

Dr. Alessio Terenzi

AFFIDAVIT

I declare that I have authored this thesis independently, that I have not used other than the declared sources/resources, and that I have explicitly indicated all material which has been quoted either literally or by content from the sources used. The text document uploaded to TUGRAZonline is identical to the present master‘s thesis.

Date	Signature

Abstract

G-quadruplexes (G4) are structurally very polymorphic non-canonical DNA/RNA secondary structures, which can readily form in guanine-rich sequences both *in vitro* and *in vivo*. As their location was found to be non-random and enriched in biologically relevant sites of the genome, such as telomeres, oncogene promoters as well as 5' and 3' untranslated regions (UTRs), G4s attracted increasing attention during the last years as novel promising targets for anticancer therapy. Thus, the rational design of small molecule ligands selective for G4s has become a promising strategy in the development of potential antitumor agents. Amongst them, metal-based compounds have emerged as particularly strong and selective G4 binders. Based on a recent report of a self-assembly strategy of Pt_2L_2 boxes aimed at targeting G-quadruplex structures, a new, improved Pt_2L_2 metallacycle displaying intrinsic fluorescence was synthesized.

The aim of this study, thus, was to explore the biological applicability of this Pt_2L_2 compound for potential antitumor therapy and investigate its intracellular behavior. Moderate cytotoxic effects and anti-proliferative activity were observed in different human cancer cell models. Live cell imaging and confocal laser scanning microscopy (CLSM) further revealed that this compound is stable in the intracellular milieu, taken up by cancer cells and delivered to the nucleus displaying a strong blue fluorescence. This fluorescence signal was more resistant to UV photobleaching in nucleoli, nuclear substructures known to be particularly rich in G4-forming sequences, which indicates that the Pt_2L_2 metallacycle can detect both double-stranded and G-quadruplex DNA structures, but has a higher affinity for G4s. Immunostaining with a G4-selective antibody further proved that the Pt_2 compound shares the identical final molecular target. Competition assays showed that the metallacycle replaces other well-established G4 ligands. Moreover, photophysical changes including fluorescence quenching and increased absorption were observed upon G4 binding, indicating, once again, that the compound displays increased selectivity for G4s compared to dsDNA. Finally, via whole genome gene expression microarray and gene set enrichment analysis (GSEA) it was revealed that the Pt_2 compound indeed targets G4 regulated genes, especially genes located in chromosomal regions enriched for G4 structures.

Summing up, we were able to show that the novel Pt_2L_2 metallacycle is a promising candidate for targeting and detecting G-quadruplex DNA/RNA structures in cancer cells and aids in the development of new G4-selective Pt-based anticancer compounds.

Zusammenfassung

G-Quadruplexe (G4) sind strukturell sehr polymorphe DNA/RNA Sekundärstrukturen, die sich in Guanin-reichen Abschnitten sowohl *in vitro* als auch *in vivo* formen können. Diese Motive bilden sich nicht zufällig, sondern vor allem an biologisch relevanten Stellen des menschlichen Genoms, wie etwa in Telomeren, Promoterregionen von Onkogenen sowie in 5'- und 3'-untranslatierten Regionen (UTRs). Durch diese Entdeckung haben G4s in den letzten Jahren sehr viel Aufmerksamkeit als potenzielles Angriffsziel für die Krebstherapie auf sich gezogen. Deshalb ist vor allem das rationale Design von G-Quadruplex-selektiven Liganden Gegenstand aktueller Forschungsstrategien in der Entwicklung neuer Krebsmedikamente. Darunter haben sich insbesondere metallhaltige Verbindungen als äußerst starke und selektive G-Quadruplex Liganden herauskristallisiert. Basierend auf einer kürzlichen Veröffentlichung über neu entwickelte, speziell auf G-Quadruplex Strukturen abgezielte Pt_2L_2 Metallacyclen, wurde ein neuer, verbesserter Komplex synthetisiert, der darüber hinaus auch fluoreszierende Eigenschaften aufweist.

Das Ziel dieser vorliegenden Arbeit war es, die biologische Anwendbarkeit dieser Pt_2L_2 Verbindung für die Krebstherapie zu erforschen und das Verhalten im intrazellulären Milieu zu untersuchen. Dabei wurden moderate zytotoxische und antiproliferative Auswirkungen auf unterschiedliche humane Krebzellmodelle beobachtet. Darüber hinaus wurde mittels Lebendzell- sowie konfokaler Laser-Scanning-Mikroskopie nachgewiesen, dass der Pt_2L_2-Komplex im intrazellulären Milieu stabil bleibt, von Krebszellen aufgenommen wird und sich im Zellkern anreichert. Dabei emittiert er eine deutliche, blaue Fluoreszenz, welche nach UV Photobleichung vor allem in Nucleoli, G-Quadruplex-reichen Substrukturen im Inneren des Zellkerns, erhalten bleibt. Dies weist darauf hin, dass der Platinum-Komplex sowohl doppelsträngige wie auch G-Quadruplex DNA erkennt, jedoch stärker an G-Quadruplex Strukturen bindet. Mittels Immunfärbung mit einem G4-selektiven Antikörper konnte zudem belegt werden, dass beide Verbindungen dasselbe molekulare Endziel teilen. Durch Kompetitionsassays wurde außerdem deutlich, dass die untersuchte Pt_2L_2 Verbindung auch andere bekannte G4-Liganden verdrängt. Darüber hinaus wurden photophysikalische Veränderungen wie Fluoreszenzlöschung und verstärkte Absorption speziell durch die Bindung von G-Quadruplex Strukturen festgestellt, was erneut darauf hinweist, dass der Ligand selektiver mit G-Quadruplex gegenüber doppelsträngiger DNA interagiert. Zuletzt wurde in dieser Arbeit der Einfluss des Pt_2L_2-Komplexes auf Genexpressionsebene untersucht, wobei festgestellt wurde, dass dieser vor allem Gene in G4-reichen chromosomalen Regionen beeinflusst.

Zusammenfassend konnte in dieser Studie gezeigt werden, dass der Pt_2L_2-Komplex ein vielversprechender Kandidat für den Nachweis von G-Quadruplex DNA/RNA Strukturen in

Krebszellen ist und die Entwicklung von neuen G4-selektiven, platinbasierten Krebsmedikamenten vorantreiben kann.

“It is through science that we prove, but through intuition that we discover.”

» Henri Poincaré «

Acknowledgements

First and foremost, I would like to express my deepest gratitude equally to both of my supervisors, Walter Berger and Alessio Terenzi. I could not have imagined having better advisors and mentors by my site during this master's thesis. I greatly benefited from Walter's immense knowledge, helpful advices, unwavering guidance and support even on the most stressful days. I was deeply inspired by his way of doing science, his handling of unexpected results, his outstanding enthusiasm and particularly by himself and his way of leadership. Similarly, I want to thank Alessio for his throughout positive attitude, his empathy and enormous support. Without him this thesis, and especially this paper, would have never been possible. Thanks for always believing in me and encouraging me, even when I was sometimes a little pessimistic.

I would like to extend my sincere thanks to Michael Murkovic, my supervisor at the TU Graz, who enabled me to perform this thesis in Vienna.

Thanks to Carina for being my mentor, introducing me into the world of cancer research and especially for correcting this thesis.

I am also deeply indebted to Bernhard, probably the most patient person I have ever met, for his enormous support and sharing his knowledge with me throughout my whole research time.

Furthermore, I am very grateful for the huge assistance of Christine, who prepared thousands of metaphase chromosomes with me, was always interested in my experimental outcomes and brightened me up with chocolate in stressful situations.

I very much appreciate the effort of Johannes and Gerald, who helped a completely lost master student to understand the complexity of microscopes.

Special thanks to Mira, for all the nice lab-talks, the most delicious cake recipes and especially for all the help during this hell of revisions!

Moreover, this journey would not have been possible without the assistance of my family and friends, especially my father, who supported me unconditionally throughout my whole life and my brother, the one of my family I can share my passion for research with and who recommended this research group to me.

Special thanks to Julian, for always believing in me even when I wasn't and bringing me food into the lab when I had to stay for night shifts.

I want to thank Veronika and August for always being there for me and giving me the opportunity to escape the hustle and bustle of Vienna and write large parts of this thesis in an idyllic and vacation-like atmosphere.

Finally, I am also very grateful for all the other great group members of this research team I was not able to mention, their continuous support and help whenever I had questions, the team spirit and for all the (of course strictly after-work) schnapps!! ;)

Table of Contents

1 Introduction

1.1 Cancer Incidence and Mortality

Cancer constitutes one of the leading causes of death worldwide, with an estimated 18.1 million new cases and 9.6 million deaths in 2018 [1,2]. Globally, 1 in 5 men and 1 in 6 women will be diagnosed with cancer during their lifetime and 1 in 8 men as well as 1 in 11 women will eventually die from the disease or disease-related consequences, making cancer research of crucial importance in the development of effective cancer treatment and prevention strategies [3]. As evaluated by the WHO in 2015, cancer represents the first leading cause of premature mortality in 48 out of 172 countries and the second leading reason for death in further 43 countries (Figure 1) [1].

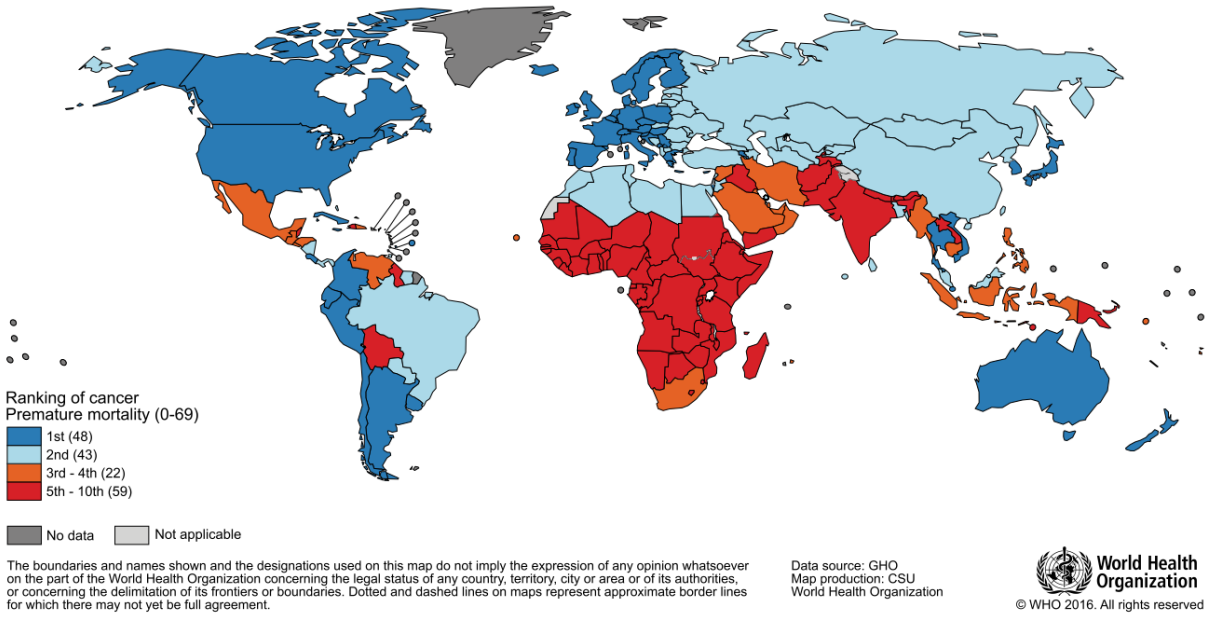

Figure 1: World map illustrating the ranking list for cancer as a cause of premature death (before age 70) [1]**.**

Cancer incidence and mortality is increasing dramatically worldwide. In Austria, the number of newly diagnosed cancers is predicted to increase until the year 2030 by 14% (Figure 2A). Similar is expected for cancer-related deaths in Austria until 2030, with an expected increase of 16% (Figure 2B) [4].

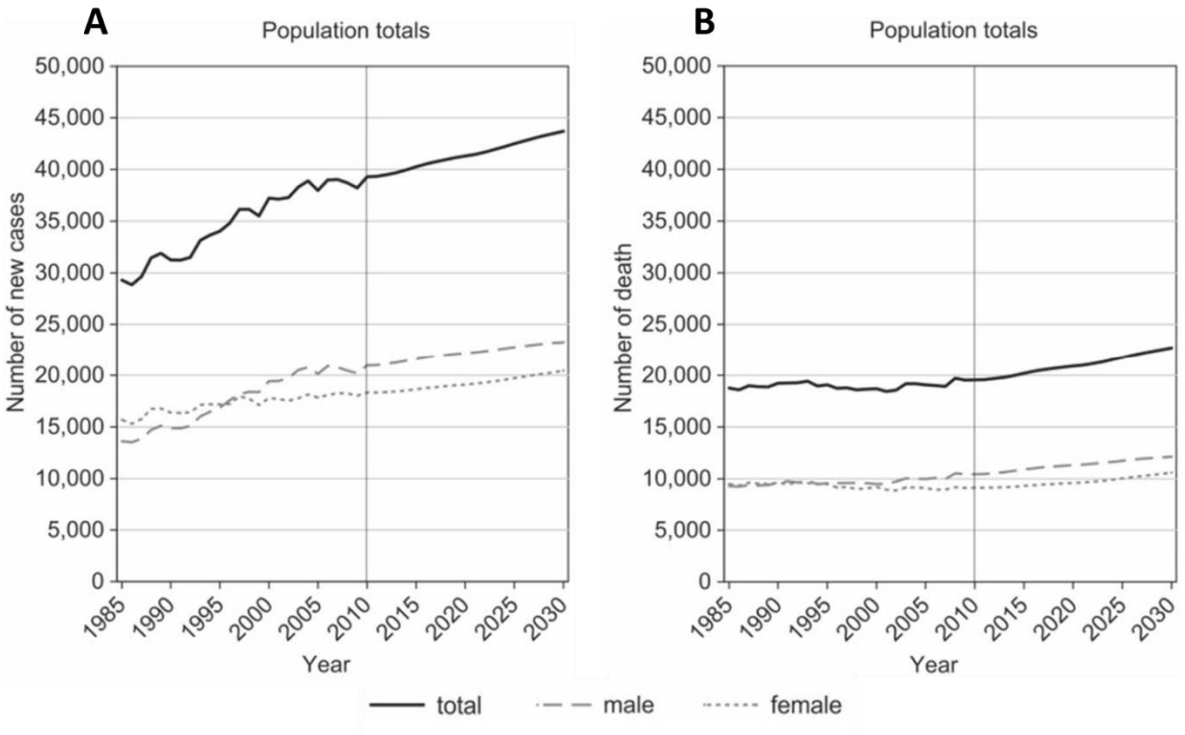

Figure 2: Cancer incidence and mortality is predicted to increase in Austria until 2030. (A) The number of newly diagnosed cancer cases is expected to rise by 14%. **(B)** Similarly, the number of cancer-related deaths is estimated to grow by 16%. Adapted from Klotz et al., 2019 [4]**.**

Globally, women are slightly less affected by cancer compared to men, with 9.5% fewer newly diagnosed cases (9.5 million vs. 8.6 million) and 22% less cancer-related deaths (5.4 million vs. 4.2 million) in 2018 [1]. In men, lung cancer is the most often diagnosed cancer type, representing also the leading cause for mortality. The second most frequent type of cancer in males is prostate cancer, followed by colorectal cancer. Regarding mortality however, liver cancer is the second leading reason for cancer-associated deaths in men, followed by stomach cancer. Among females, breast cancer constitutes both the dominating diagnosed cancer and reason for death, with colorectal and lung cancer following (Figure 3). However, these statistics vary considerably depending on the country, economic condition and lifestyle [1].

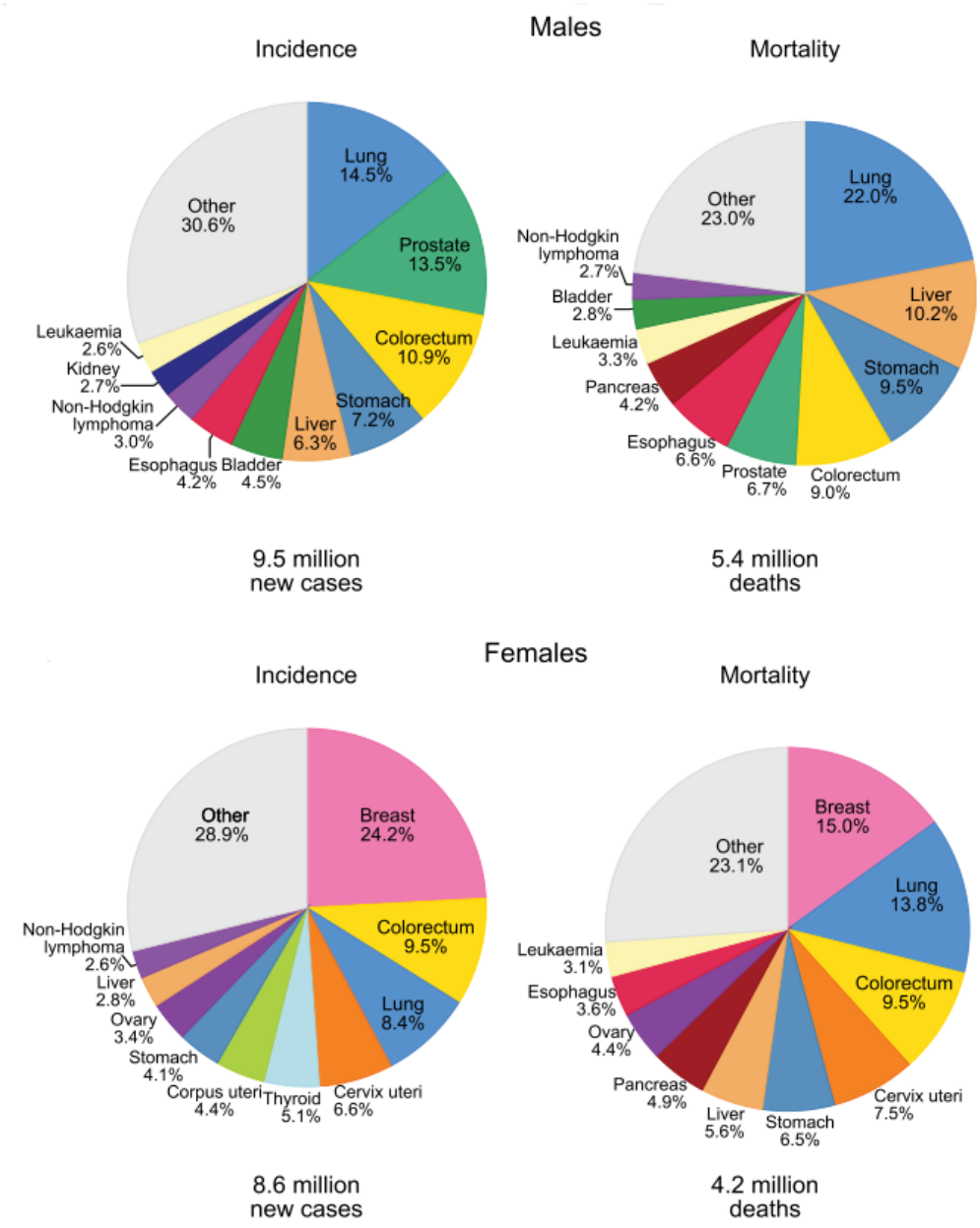

Figure 3: Global incidence and mortality regarding to cancer types in males (upper pie charts) and females (lower pie charts) in 2018 [1]**.**

1.2 Etiology of Cancer

Cancer as a broad term comprises more than 100 different diseases collectively characterized by unregulated proliferation of cells that can form in almost any part of the body. Moreover, cancer cells can invade adjacent tissue or metastasize through the blood and lymph systems to distant sites, the leading cause for approximately 90% of cancer-related deaths [5,6]. The basic steps in the process of carcinogenesis resemble in all types of the disease, which is believed to be a complex, multistep process across long periods of time, consisting of three major stages: (1) tumor initiation, (2) promotion and (3) progression. Carcinogenesis is initiated by the abnormal proliferation of a single mutated cell, which might evolve spontaneously or result from exposure to a carcinogen [7]. A tumor eventually develops through successive rounds of mutations or epigenetic alterations and proliferations, including both inactivation of tumor suppressor genes and activation of oncogenes [8]. Some of the mutations may provide selective advantages, such as an increased growth or decreased death rate, resulting in progeny dominating the tumor population. This process is also known as "clonal evolution", which continues throughout tumor progression, leading to increasingly malignant sub-populations (Figure 4) [9,10].

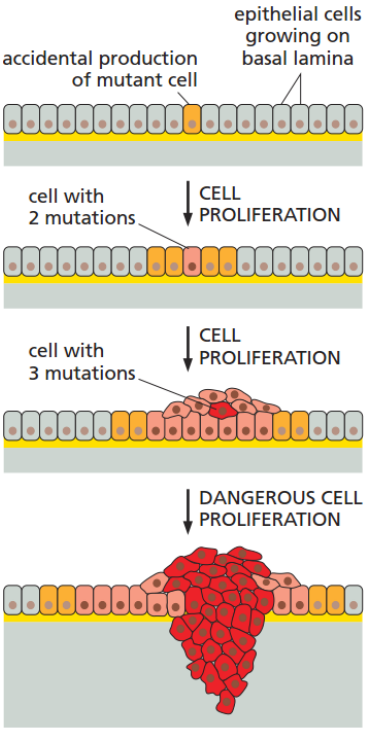

Figure 4: Process of clonal evolution. Carcinogenesis is a multistep process derived from a single mutated cell and comprises three main stages: tumor initiation, promotion and progression. Tumors are formed through successive cycles of mutation and clonal selection [10].

Depending on the growth aggressiveness of tumors, two broad subtypes can be distinguished. Benign tumors display localized growth without invading adjacent tissues, whereas malignant tumors can invade surrounding tissues and metastasize. Only malignant tumors are correctly referred to as cancer (Figure 5) [10].

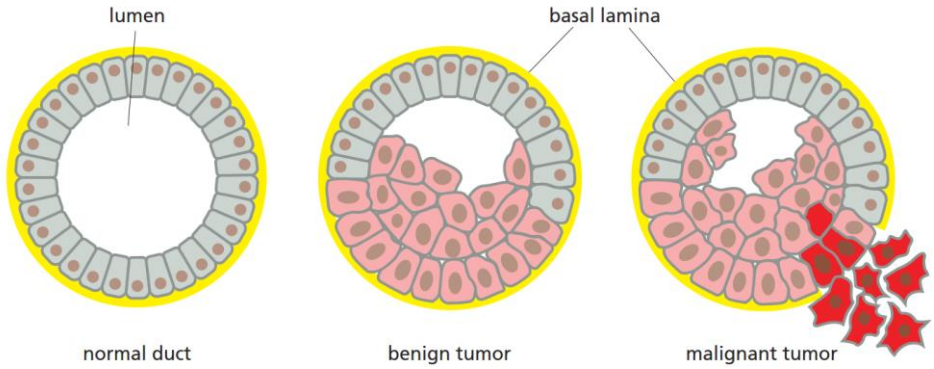

Figure 5: Differences between benign and malignant tumors. While the growth of benign tumors is locally confined, malignant tumors can invade adjacent tissues and metastasize to distant sites through blood and lymph systems [10].

Moreover, the process of carcinogenesis is considerably dependent on the surrounding extracellular matrix and stromal cells, collectively referred to as tumor microenvironment (TME). TME is composed of normal connective tissue comprising non-malignant cells such as endothelial cells forming blood and lymphatic vascular networks, cancer associated fibroblasts (CAFs), neuroendocrine cells, immune cells, inflammatory leukocytes and the extracellular matrix (Figure 6) [10–14].

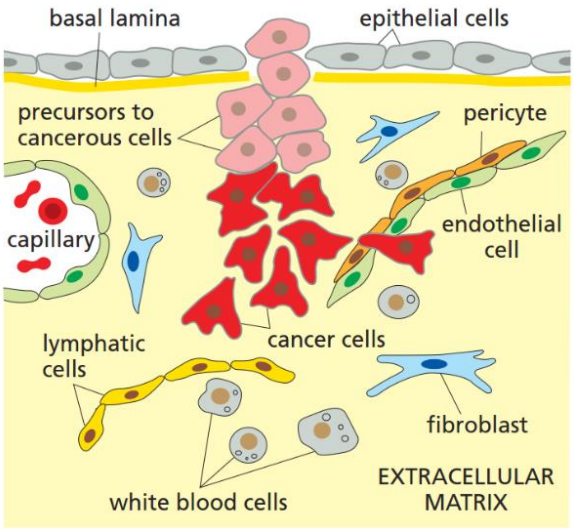

Figure 6: Tumor microenvironment. Stromal cells and extracellular matrix play a substantial role in the development of a malignant tumor [10].

Two-way communication between the stroma and tumor cells support the growth and invasion of the tumor via the secretion of signaling molecules such as growth factors, chemokines, interleukins and matrix metalloproteinases, rendering the tumor dependent on its specific stromal cells [13,15,16].

1.3 Hallmarks of Cancer

As cancer develops over time, non-malignant cells acquire properties during clonal evolution, which direct their transformation into malignant cells (Figure 7) [17,18].

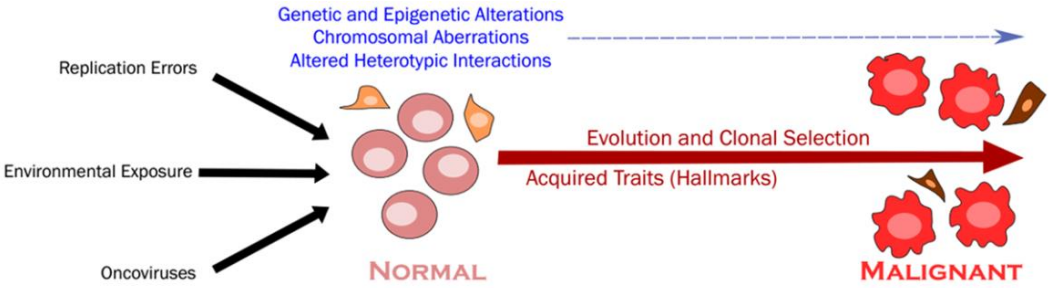

Figure 7: Transformation process of healthy into malignant cells. During carcinogenesis, non-malignant cells acquire in the course of clonal evolution certain traits which promote their malignancy [18]**.**

These genetic changes can be grouped into key biological properties, the so-called "Hallmarks of Cancer", which were first postulated by Hanahan and Weinberg in 2000, comprising six distinct characteristics (1-6) [17]:

(1) Sustaining proliferative signaling
(2) Evading growth suppressors
(3) Resisting cell death
(4) Enabling replicative immortality
(5) Inducing angiogenesis
(6) Activating invasion and metastasis

Even though this concept was widely accepted, substantial progress in cancer research and increasing knowledge lead to considerable criticism over time [19–21]. In 2010, an article in *Nature Reviews Cancer* i.a. argued that a hallmark of cancer should per definition only apply to malignant tumors, yet five of the six proposed hallmarks are also attributable to benign tumors. Only "invasion and metastasis" would refer to a trait distinguishing malignant from benign tumors [21]. In 2011, Hanahan and Weinberg therefore revised their proposed hallmarks and added two further hallmarks (7,8) as well as two enabling characteristics (9,10) involved in the pathogenesis of cancer cells, the so-called "next generation of cancer hallmarks" (Figure 8) [22]:

(7) Reprogramming of energy metabolism
(8) Avoiding immune destruction
(9) Genome instability and mutation
(10) Tumor-promoting inflammation

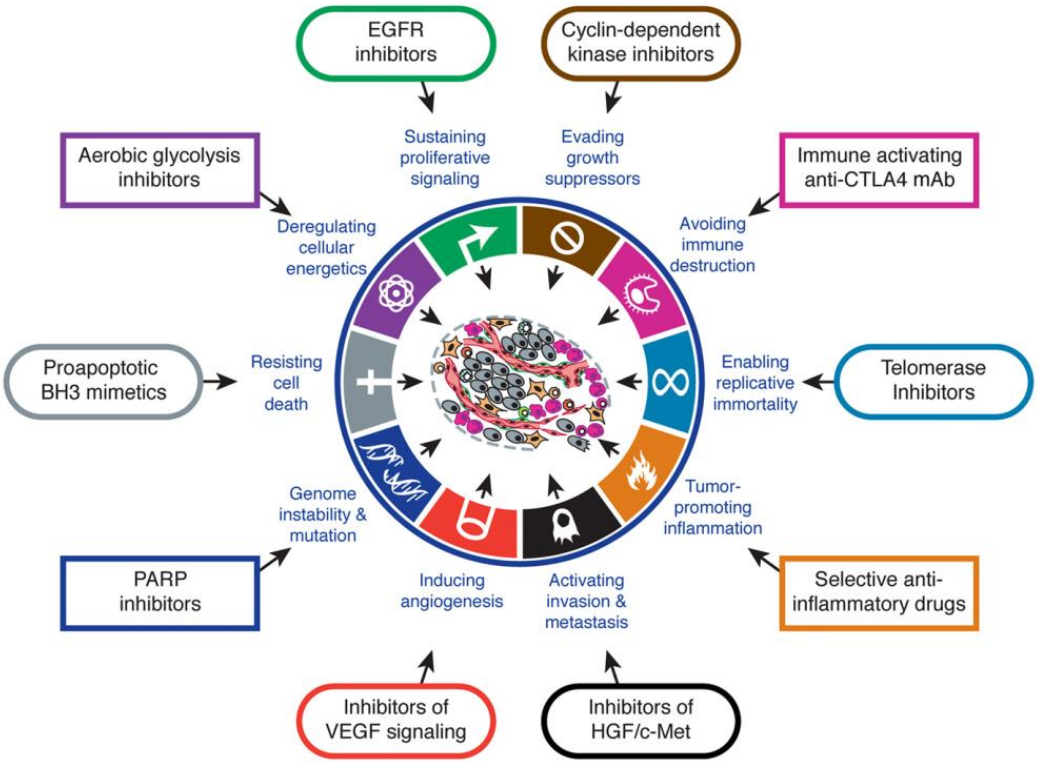

Figure 8: Ten hallmarks of cancer in correlation with their possible therapeutic targeting options [22]**.**

1.4 Risk Factors and Prevention

Even though cancer incidence is highest among adults older than 65 years, every age group can be affected [23]. Many intrinsic and non-intrinsic risk factors increase the probability of developing cancer. While intrinsic risk factors such as random DNA replication errors cannot be prevented, non-intrinsic risk factors are at least partially controllable. These include endogenous risk factors, such as biological age, inherited genetic defects, genetic susceptibility, gender, altered hormone levels as well as exogenous risk factors including exposure to radiation, viruses, chemicals and several lifestyle-related factors (Figure 9) [24]. Endogenous risk factors are to some extent modifiable, for example sex steroid hormones are involved in development of prostate and breast cancers and are i.a. affected by other exogenous factors such as diet or physical activity, rendering this factor partially modifiable [24,25]. Among exogenous factors, smoking constitutes the biggest lifestyle-related risk factor, responsible for approximately 20%-30% of all cancer cases [26]. Thus, through lifestyle changes and vaccinations the risk for developing cancer can at least partly be reduced [27].

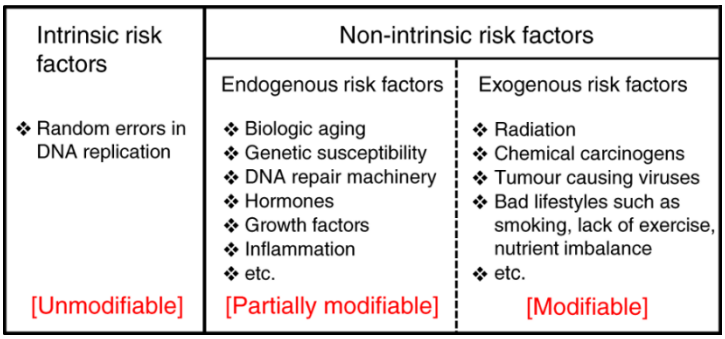

Figure 9: Risk factors for cancer can be divided in intrinsic and non-intrinsic factors. While intrinsic risk factors are unmodifiable, non-intrinsic risk factors including endogenous and exogenous risk factors are at least to some extent modifiable [24].

1.5 Classification

Cancers can be classified according to the type of cell the tumor originates from, such as [28,29]:

- **Carcinoma**

  Cancers that arise from epithelial cells, constituting the cells on the inner and outer surfaces of the body forming a defensive barrier, are called carcinomas. This group represents the most frequent type of cancer (~85%). Depending on the origin of the various epithelial cells further subtypes exist:

  - **Adenocarcinoma**: derives from glandular epithelial tissue.
  - **Basal cell carcinoma**: originates from small round cells at the bottom of the epidermis, the outer layer of the skin, and represents the predominant type of skin cancer [30].
  - **Squamous cell carcinoma (epidermoid carcinoma)**: develops from epithelial cells which can be found in the outer section of the epidermis, the linings of hollow organs as well as the respiratory and digestive tracts [30].
  - **Transitional cell carcinoma**: derives from the transitional epithelium found in the organs of the urinary system.

- **Sarcoma**

  Sarcomas arise from connective tissues, which includes fibrous tissues, fat, cartilage, bone and blood vessels.

- **Haematological (blood) cancer**

  Lymphoma

  Cancer originating from lymphocytes (type of leukocytes, the white blood cells), important cells for the adaptive immune systems, which include B lymphocytes (B cells) and T lymphocytes (T cells). While B cells are involved in the humoral immunity (antibody-mediated), T cells are responsible for cell-mediated immunity [31]. Two main subtypes of lymphomas are described:

  - **Hodgkin Lymphoma**: B cell lymphoma arising from giant, multinucleated cells with an abnormal morphology, known as Reed-Sternberg cells [32].
  - **Non-Hodgkin Lymphoma**: comprises a group of lymphomas, formed from B or T cells.

  Leukemia

  Cancer that arises from blood-forming cells of the bone marrow.

  Multiple Myeloma

  Cancer originating from plasma cells, antibody-producing white blood cells.

- **Melanoma**

  Cancer forming in melanocytes. These melanin-producing cells are located in the skin, eye and internal organs.

- **Germ cell tumor**

  Cancer derived from germ cells, the reproductive cells (egg and sperm cells).

- **Blastoma**

  Cancer developed from precursor cells. Blastoma is usually used as suffix and cancers are termed according to the location, such as [33]:

  - Medulloblastoma (brain tumor)
  - Hepatoblastoma (liver tumor)
  - Nephroblastoma (kidney tumor)
  - Retinoblastoma (tumor of the eye's retina)

1.6 Cancer Treatment

The choice of treatment depends on different parameters, including the cancer type, its location, disease progression as well as age and health conditions of the patient. Before 1950, surgery was the only prevailing option available for treating cancer, however only a fraction of the patients could have been cured. After 1960, radiotherapy was introduced for local control of lesions. Over time it was discovered that the combination of both methods is most effective [34]. Nowadays, many different therapy options exist, including chemotherapy, surgery, radiotherapy, immunotherapy, hormone treatments and targeted therapy [35].

1.6.1 Surgery

Ephraim McDowell paved the way for surgical treatment in 1809 by performing abdominal surgery of an ovarian tumor and proofing that cancer can be cured this way [36]. In 1894, William Halsted introduced radical mastectomy for breast cancer, which had the most incisive impact on surgical treatment of cancer [37]. This technique involved the *en bloc* resection of surrounding breast tissue to eradicate all cancer cells and became known as the “Halsted mastectomy”, later on “the cancer operation” or “the complete operation”, as it was the most commonly performed operation for the removal of all types of cancers [38,39]. However, complete removal of all malignant cells is often not feasible and recurrence a major issue, making adjuvant (supplementary therapy after primary treatment) and neoadjuvant (adjuvant therapy before primary treatment) therapies important (Figure 10) [40].

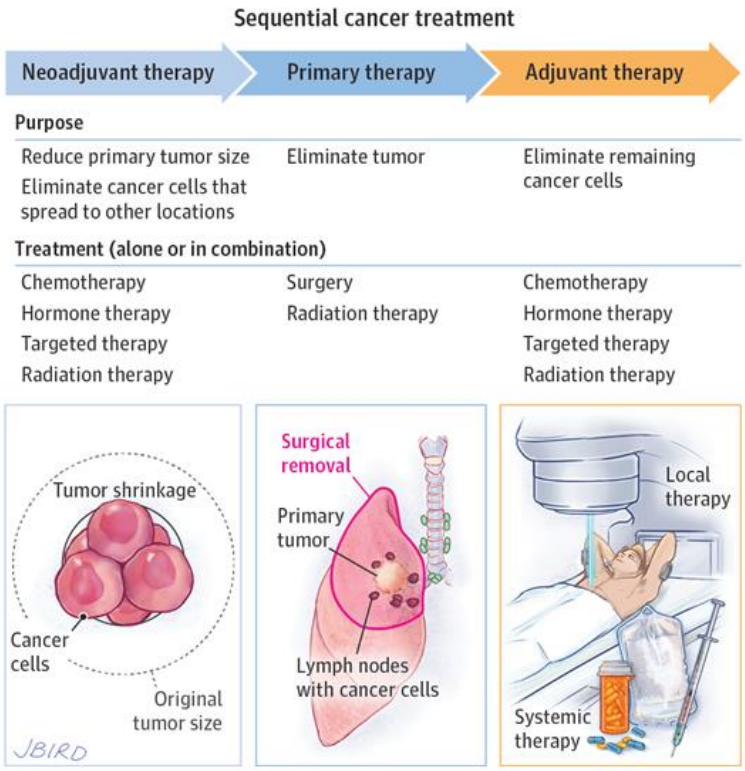

Figure 10: Neoadjuvant and adjuvant therapies can help to improve the effectiveness of the primary treatment [40]**.**

1.6.2 Radiotherapy

Besides surgery, radiotherapy is the other main treatment applied for the therapy of localized tumors and was responsible for 29% of all cured patients in 2016 [41]. Radiation therapy aims at interfering with the cell division potential of cancer cells by exerting high-energy ionising radiation which damages DNA either directly or indirectly through generation of free radicals, inducing single strand breaks (SSBs) and double strand breaks (DSBs) (Figure 11) [42,43]. However, radiation therapy is non-specific and affects also healthy cells, which is why the radiation dose needs to be tightly controlled and unintended exposure to surrounding tissue should be minimized [42,44–46].

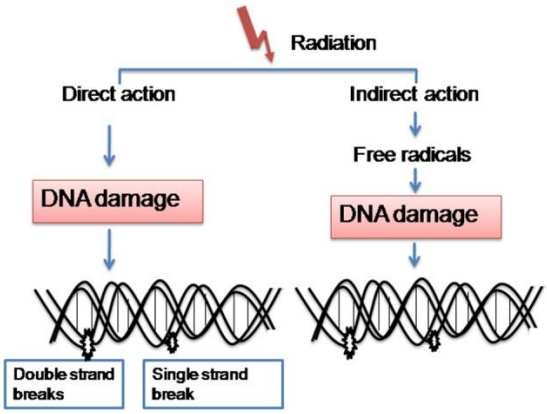

Figure 11: Effects of radiation therapy. DNA is damaged either directly or indirectly via production of free radicals resulting in SSBs and DSBs [43].

1.6.3 Hormone Therapy

Hormone treatment, also referred to as endocrine therapy, is employed for the treatment of hormone-dependent cancers such as breast, endometrial, ovarian and prostate cancers. It aims at manipulating the endocrine system through administration of exogenous hormones such as hormone analogues (e.g. corticosteroids, somatostatin, progestins) and inhibitors of hormone synthesis (e.g. degarelix, exemestane) or hormone receptors (e.g. estrogen receptor modulators such as tamoxifen or androgen receptor inhibitors like flutamide) [47]. Hormone-mediated therapy is often used together with other treatment strategies (Figure 10) and can be used for neoadjuvant or adjuvant therapy. It however often entails unwanted side-effects such as hot flashes, digestive problems, oedema, fatigue, weight gain, depressions, thrombosis or osteoporosis [47–50].

1.6.4 Immunotherapy

Immunotherapy approaches to manipulate the immune system and reducing tumor-mediated suppression of anticancer immune responses. This treatment regimen managed to progress from a simple innovative strategy to huge clinical success [51]. Science magazine even awarded immunotherapy as “Breakthrough of the Year” and a “turning point in cancer” in 2013 [52]. In immune-mediated therapy two key approaches can be distinguished, active and passive immunization (Figure 12) [53]. Active immunotherapy involves mobilization of the adaptive immune system to directly fight cancer cells by targeting tumor antigens, which can be achieved via vaccination, immune checkpoint inhibitors or oncolytic viruses [51]. Of special interest are so-called neoantigens, tumor-specific antigens resulting from somatic mutations acquired during carcinogenesis which are not expressed on non-malignant cells, making this approach more tumor-specific and minimizing adverse effects. This strategy is especially effective in tumors exhibiting a high mutational burden [54,55]. Passive immunotherapy on the other hand aims at enhancing the anti-tumor response of patients with an unresponsive immune system, which can be achieved via the administration of monoclonal antibodies, lymphocytes or cytokines [8,51].

Even though immunotherapy yielded already great success in the clinics, major drawbacks still emerge. Besides being a cost-intensive therapy, patients’ treatment response cannot be predicted and varies substantially. Therefore, the identification of new biomarkers is required to personalize immunotherapy and improve therapy efficacy [55,56].

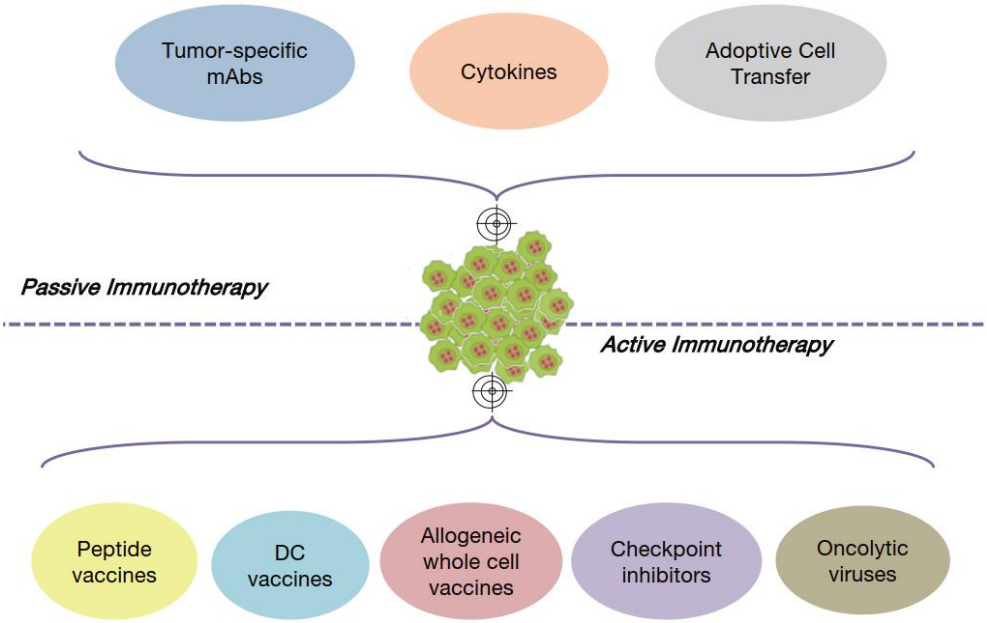

Figure 12: Active and passive immunotherapy. While active immunotherapy directs the adaptive immune system to destroy cancer cells via vaccines, immune checkpoint inhibitors or oncolytic viruses, passive immunotherapy stimulates the anti-tumor response of a patient's weak immune system via administration of mAbs, cytokines or lymphocytes [51].

1.6.5 Targeted Therapy

Targeted therapy increases the efficacy and specificity of the treatment, concomitantly reducing side-effects to healthy cells. In this approach, specific targets of interest are identified and drugs are developed that either directly act on these targets or that selectively deliver agents to these destinations. This can be realized by means of monoclonal antibodies, small molecule inhibitors, immunotoxins or drug nanocarriers [57–59]. A prominent example is tamoxifen, the first targeted drug approved by the FDA in 1970, which selectively blocks estrogen receptor (ER) and is therefore utilized for the treatment of estrogen receptor-positive breast cancer [60]. Moreover, the treatment of melanoma was revolutionized by introduction of tyrosine kinase inhibitors (TKIs) targeting the BRAF kinase such as vemurafenib and dabrafenib [61]. For therapy of non-small cell lung cancer (NSCLC), epidermal growth factor receptor (EGFR) inhibitors such as erlotinib or gefitinib are highly effective [62].

1.6.6 Chemotherapy and DNA as a Target in Anticancer Therapy

Chemotherapy is referred to the administration of chemicals or drugs aimed at killing or inhibiting the growth of cancer cells. As these agents are largely unspecific, also non-malignant cells are damaged, resulting in severe side-effects like nausea, vomiting, hair loss, fatigue or fever. Administration is most frequently achieved by intravenous infusion, however also other forms such as oral, subcutaneous or intramuscular routes are described, depending on type and stage of the tumor [63,64]. Chemotherapeutic drugs can be either used alone or in combination with other above-mentioned therapies and often display DNA-damaging properties. In fact, even before the double helical structure of DNA was discovered in 1953 by Watson and Crick [65], DNA has already been targeted by anticancer compounds [66]. Among them, several agents have been identified, including antimetabolites, intercalators and alkylation agents. Antimetabolites have similar structures to metabolites and impair nucleic acid synthesis either by depleting the supply of nucleotides or by incorporation of chemically modified nucleotides [67]. Methotrexate as an example falls into this category by being a folate antagonist and inhibiting dihydrofolate reductase (DHFR), which blocks the synthesis of the crucial DNA building blocks purines and pyrimidines and thus can inhibit growth and proliferation of cancer cells [68]. Intercalators such as actinomycins on the other hand interact reversibly with the double helix by inserting an aromatic ring system between the base-pairs of DNA, and thereby inhibit DNA replication in cancer cells [69]. Alkylation agents interact non-specifically with DNA and block the replication machinery by causing bulky DNA adducts or crosslinked DNA, depending on whether they are monofunctional or bifunctional. A well-known example for bifunctional alkylating agents are nitrogen mustards, the first DNA damaging compounds used for the treatment of cancer, which impair replication fork progression and lead to apoptotic cell death [70,71].

1.6.6.1 DNA-Targeting Metal Complexes

Until 1960, chemotherapy drugs used in the clinics to treat cancer were based exclusively on organic compounds. A fortunate coincidence by Dr. Barnett Rosenberg in 1965 [72] led to the discovery of the anticancer properties of an already 1844 synthesized metal compound by Michele Peyrone [73] - later known as cisplatin - which ushered in a new area of DNA-targeting drugs. Since then, metal-based chemotherapy agents, especially platinum compounds, have become an essential part of modern cancer therapy - to about 50 % of all patients, platinum drugs are administered during their treatment [74]. Around 1.29 billion US$ of platinum-based anticancer drugs are sold worldwide today and, according to a new GIR (Global Info Research) study, the global market is expected to

reach 1650 million US$ by 2024 [75]. Three platinum-containing drugs have been approved by the U.S. Food and Drug Administration (FDA) for treating cancer and entered worldwide clinical use: cisplatin, carboplatin and oxaliplatin [76]. Cisplatin is referred to as first generation of platinum drugs. Second and third generation originate from cisplatin, having modified leaving groups (corresponding to the two chloride ligands), or amine groups. Second generation agents include a change in either one of these groups, with carboplatin being a representative having substituted leaving groups. In third generation platinum drugs both groups are replaced, like it is the case for oxaliplatin (Figure 13) [77].

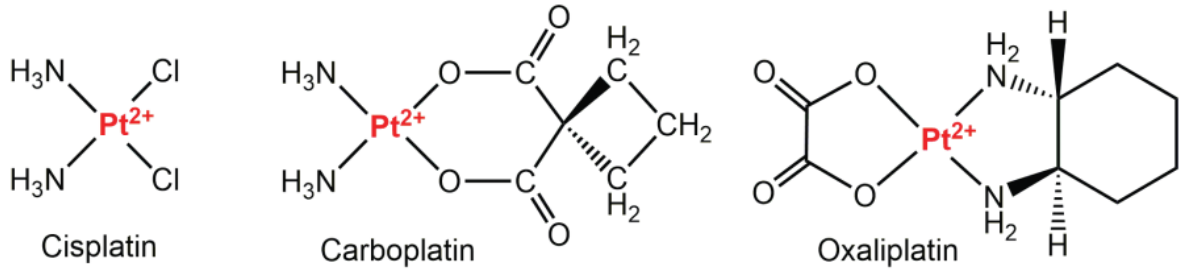

Figure 13: Chemical structures of the three worldwide approved platinum-based anticancer agents [78]**.**

An overview about the milestones in the era of anticancer platinum drugs until 2007 is given in Figure 14.

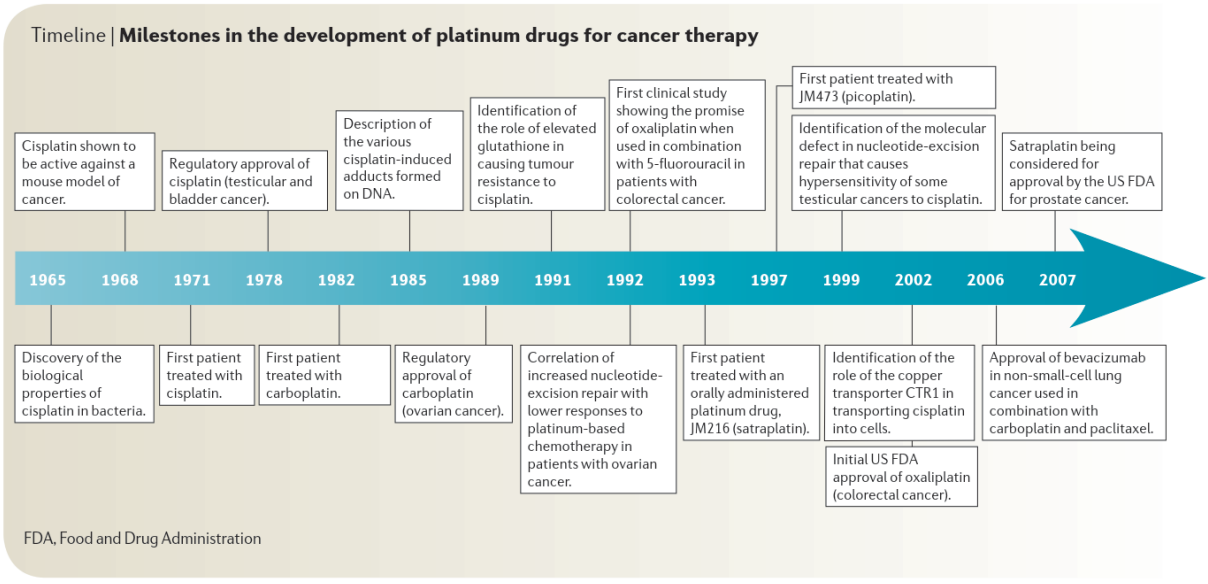

Figure 14: Timeline highlighting the history milestones of platinum drugs in cancer treatment until 2007 [79]**.**

1.6.6.1.1 Cisplatin

Cisplatin [(SP-4-2)-diamminedichloridoplatinum(II)], a square-planar Pt^{2+} coordination compound, was approved in 1978 by the FDA under the brand name Platinol® [80] and counts to the most widely used chemotherapy agents worldwide for the treatment of a variety of solid tumors including lung, testicular, ovarian, head and neck, bladder, colon, breast, gastric, esophageal, cervical cancer, melanoma, lymphomas and others [77,81]. It is especially promising in the case of testicular cancer, with an excellent prognosis for cure rates exceeding 90% and reaching nearly 100% for early-stage disease [82]. Upon administration, cisplatin enters the cells either through passive diffusion or active transport mediated by copper transporter-1 (CTR1) and exerts its antitumor effects through various mechanisms. The most acknowledged one is mediated by its ability to crosslink with the purine bases on DNA, forming DNA adducts, blocking DNA synthesis and interfering with DNA repair mechanisms. This results in DNA damage, which activates DNA damage responses (DDR) and triggers activation of several signal transduction pathways (Figure 15). Cisplatin-DNA adducts are mainly repaired via nucleotide excision repair (NER). DDR is largely regulated by p53 and c-Abl (Abelson tyrosine kinase). P53 is stabilized through phosphorylation by ataxia-telangiectasia mutated (ATM) or ATM- and Rad3-related (ATR) kinases and entails several effects such as activation of p21 leading to cell cycle arrest, or degradation of FLIP (FLICE-like inhibitory protein) and inactivation of antiapoptotic protein Bcl-XL (B-cell lymphoma-extra large) promoting apoptosis. Moreover, cisplatin-induced damage is also recognized by mismatch repair (MMR) system, which interacts with c-Abl, inducing activation of p73 and MAPK (mitogen-activated protein kinase) pathway (ERK [extracellular-signal regulated kinases], JNK [c-Jun N-terminal kinases] and p38) [83]. In the event of defective repair or excessive DNA damage, apoptosis is eventually induced (Figure 15) [83–85].

However, adverse effects and the risk of relapsing are limiting the applicability and effectiveness of cisplatin in clinics. Due to nonspecific targeting of genomic DNA, cisplatin also damages non-malignant cells, inducing nephrotoxicity, ototoxicity, hepatotoxicity, neurotoxicity, gastrointestinal toxicity and cardiotoxicity in patients [81,85–87]. Furthermore, intrinsic or acquired resistance to cisplatin constitutes another critical drawback. Acquired resistance to cisplatin may evolve from different mechanisms, such as increased drug degradation, reduced influx or elevated efflux of cisplatin (e.g. ATP-binding cassette [ABC] mediated drug efflux), enhanced DNA repair, reactivity with glutathione and metallothioneins leading to GS-X pump mediated drug export or through microRNA-214 (miR-214) targeting the PTEN/Akt (phosphatase and tensin homolog/protein kinase B) pathway (Figure 15) [77,83,88–90]. Hence, combination therapies with other chemotherapeutics (e.g. vinblastine, bleomycin or doxorubicin), natural products (e.g. melittin from honey bee venom or capsaicin from chili peppers) or targeted agents (e.g. C-75, a fatty acid synthase inhibitor) are

currently explored to overcome resistance and minimize side effects of cisplatin [91–97]. Moreover, development of cisplatin analogs have become an emerging field of research, with only two (carboplatin and oxaliplatin) having been approved worldwide and a few having entered clinical trials [78,98].

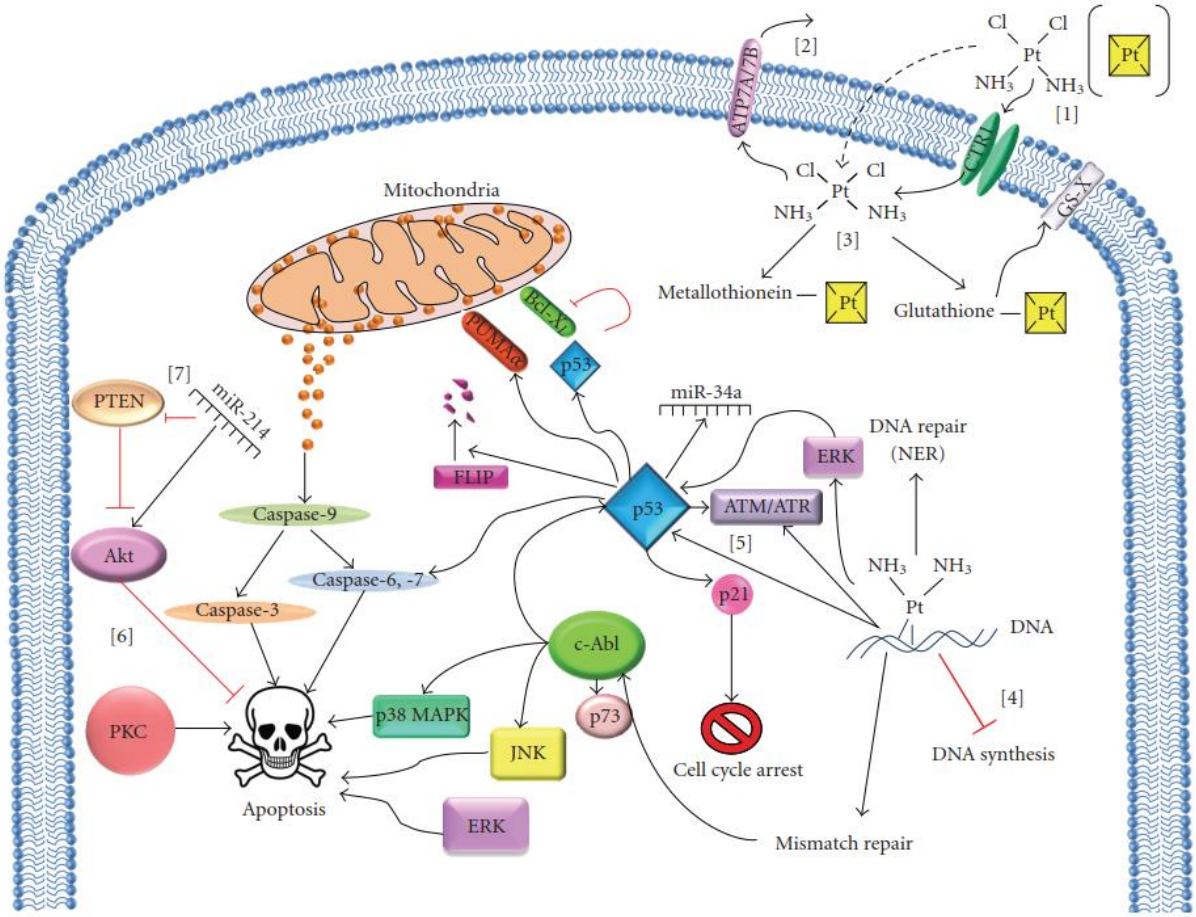

Figure 15: Cisplatin-mediated signal transduction pathways [83]**. [1]** Cisplatin enters cells either via passive diffusion or by active transport through CTR1. **[2]** Cisplatin export is mediated by ATP7A and ATP7B. **[3]** Besides DNA, cisplatin also binds to glutathione and metallothionein, with the assembly leaving the cell via the GS-X pumps. **[4]** Upon interaction with DNA, cisplatin causes DNA damage due to crosslinking the purine bases on DNA and thereby forming DNA adducts, which intereferes with DNA synthesis and activates DDR. **[5]** These adducts are repaired via NER, while the cell cycle is arrested to supply efficient time for DNA repair. DDR is mediated primarily through p53 and c-Abl. P53 is stabilized through phosphorylation of ATM or ATR, which are activated upon DNA damage. P53 entails several effects, including p21 activation which leads to cell cycle arrest or degradation of FLIP and binding to Bcl-XL, which promotes apoptosis. Cisplatin-induced damage is moreover recognized by MMR, which interacts with c-Abl, inducing activation of p73 and MAPK pathway (ERK, JNK and p38), eventually leading to apoptosis. **[6]** Further involved in apoptosis pathway are PKC, ERK and Akt kinases. **[7]** miR-214 promotes cell-survival and resistance to cisplatin via binding to 3'UTR of PTEN, leading to inhibition of PTEN and activation of Akt.

1.6.6.1.2 Carboplatin

Carboplatin [cis-diammine-cyclobutanedicarboxylato-platinum (II)] was the second platinum complex approved by the FDA in 1989 under the brand name Paraplatin® [99] and is used for treatment of ovarian, lung, head and neck cancers. Carboplatin differs from cisplatin by its leaving group,

possessing a less labile cyclobutane-decarboxylate group instead of the chloride ligands, which entails a decreased reactivity and a slower DNA binding [82]. Thus, reduced adverse effects have been described, especially the lack of nephrotoxicity, neurotoxicity and ototoxicity, which is the reason for the better tolerability of carboplatin compared to cisplatin [100]. However, a severe constraint limiting the application of carboplatin is its myelosuppressive effects, appearing in 20–40% of patients if conventional doses are administered and in more than 90% of patients receiving high doses. The main symptoms of carboplatin-induced myelosuppression include thrombocytopenia (low platelet count) and neutropenia (low neutrophil count), leading to anemia and predisposing to opportunistic bacterial and/or fungal infections such as *Pseudomonas aeruginosa* or *Candida albicans* [82,101].

1.6.6.1.3 Oxaliplatin

Oxaliplatin [(trans-R,R-cyclohexane-1,2-diamine)oxalatoplatinum(II)], the third and last platinum agent that received full approval by the FDA in 2004 under the trade name Eloxatin® [102], represents one of the mainstay chemotherapeutic drugs in gastrointestinal cancers. It is used as adjuvant treatment for colon cancer in combination with fluorouracil and leucovorin or folinic acid [103]. Belonging to the third generation of platinum agents, it is composed of a platinum atom complexed with an oxalate ligand as leaving group and a diaminocyclohexane (DACH) moiety instead of the amine groups present in cisplatin. The DACH ligand is reported to provide a greater cytotoxicity of the drug compared to the other two approved platinum agents, and additionally prevents cross-resistance with them [82,104]. Further advantages of Oxaliplatin include the ease of administration and reduced side effects, however it has shown to induce moderate myelotoxic effects and cause peripheral neuropathy [104,105].

1.6.6.2 Limitations

Even though targeting DNA for anticancer therapy can be effective, several drawbacks exist. Especially the lack of selectivity, resulting in severe adverse toxicity effects to non-malignant cells as well as the risk of secondary cancer development and acquired resistance are limiting the clinical applicability of DNA-damaging agents. Therefore, the primary objective is to enhance the selectivity of the anticancer compounds and minimize concomitant side effects. This has drawn interest towards targeting non-canonical DNA-structures which are predominant in cancer cells. Especially, one unusual DNA structure that attracted attention to become a promising target for anticancer therapy is the G-quadruplex (G4) [106].

1.7 G-Quadruplex DNA as a Novel Target for Anticancer Drugs

In 1910, long before the discovery of the double helical structure of DNA [65], the Norwegian scientist Ivar Bang already reported the gel formation potential of concentrated solutions of guanylic acids [107]. However, it took more than 50 years, until it was revealed that this phenomenon is attributable to helix formation by the guanylic acid [108], proposing the key structural component of a G-quadruplex, known today as G-quartet or G-tetrad.

1.7.1 Structure

G-quartets are very stable cyclic planar arrangements of four guanines held together through eight Hoogsteen hydrogen bonds, which can transiently self-associate within G-rich regions of single-stranded DNA or RNA (Figure 16A). Two or more G-quartets pile on top of each other through π–π stacking and are connected by loops that arise from intervening sequences, assembling the four-stranded G-quadruplex structure (Figure 16B) [109–111]. Depending on the characteristics of the loops and the overall topology, G-quadruplexes furthermore possess four grooves of variable dimensions, contrary to the double helix exhibiting only two [112].

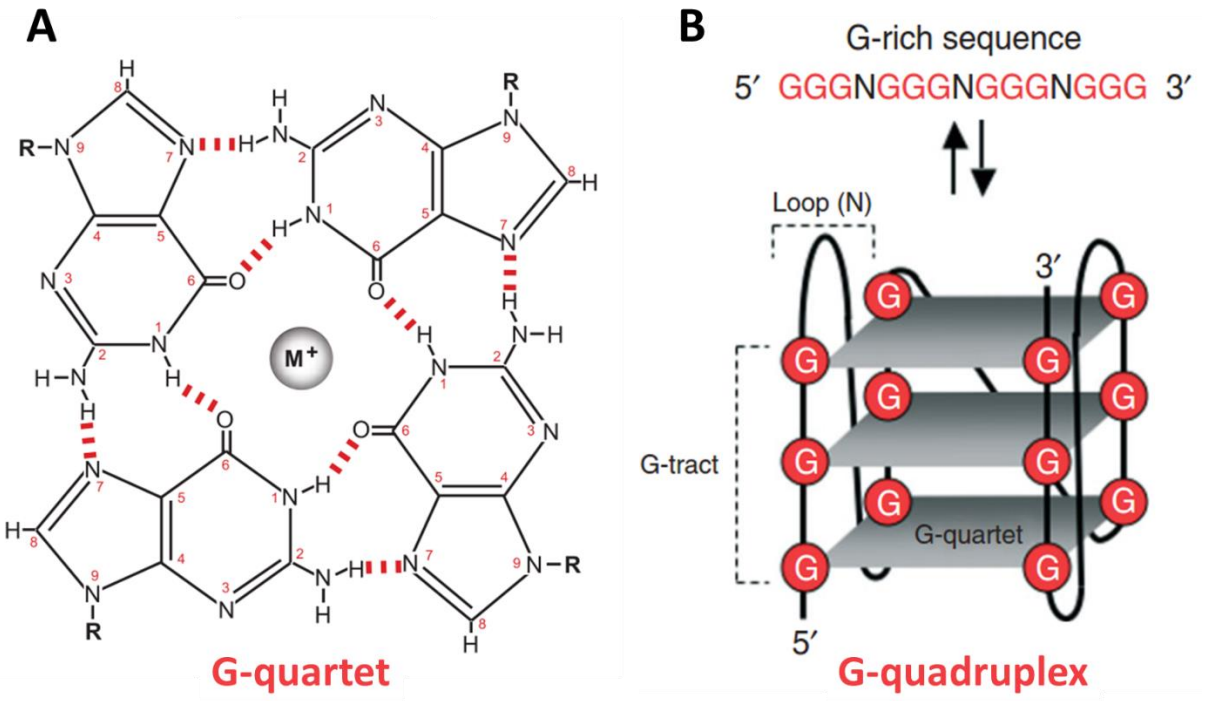

Figure 16: Structure of a G-quadruplex. (A) Schematic representation of a G-quartet, the basic constituent of a G-quadruplex, consisting of four guanine bases held together through Hoogsteen hydrogen bonds (red dashed lines) and stabilized by a central monovalent cation (M^+) [109]. **(B)** G-rich sequence that self-associates into an intramolecular G-quadruplex consisting of three π–π stacked G-quartets connected by loops [113].

The formation of G4s is further driven by monovalent cations, especially Na^+ and K^+, which bind non-specifically to the negatively charged phosphate backbone, thereby reducing the electrostatic repulsions of inwardly pointing guanine oxygens and stabilizing the G-tetrad stacks [114]. Since K^+ and Na^+ represent the predominant cations *in vivo*, physiological buffer conditions promote G4 assembly [111,115].

G-quadruplexes display considerable structural polymorphisms, including the number of strands involved (intramolecular or intermolecular folding), the backbone strand polarity (parallel or anti-parallel), the glycosidic torsion angle (*syn* or *anti,* Figure 17), the type of the loop (propeller, diagonal, edgewise), the groove dimension (narrow, medium, wide), the G-tract length as well as the nature of the ion channel [116–118].

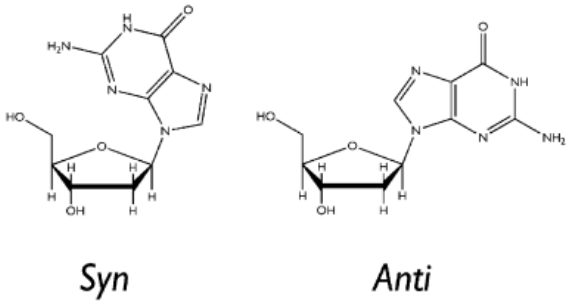

Figure 17: Glycosidic torsion angles. Rotation of the bond between the guanine base and the sugar distinguishes *syn* and *anti* conformation [119].

G-quadruplex structures are formed intramolecularly within one single strand of DNA/RNA (unimolecular) or intermolecularly between two, three or four individual strands (bi-, tri-, or tetramolecular, Figure 18) [87,120].

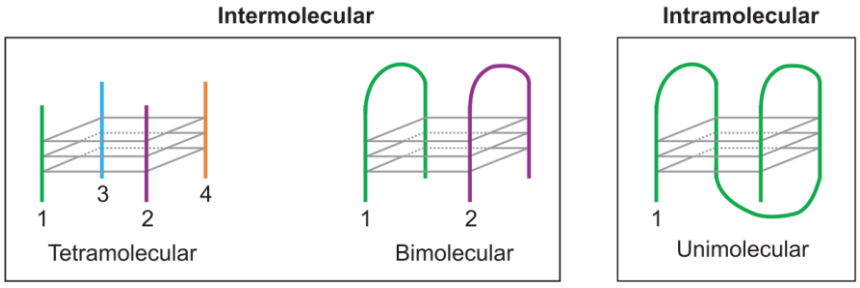

Figure 18: Depending on the number of strands, intermolecular or intramolecular G-quadruplexes are differentiated [109]**.**

Parallel G-quadruplexes are composed of four DNA strands, all having the same orientation, and each G-tetrad guanine exhibiting the identical glycosidic bond *anti* conformation (*anti-anti-anti-anti*). In anti-parallel G-quadruplexes, both *syn* and *anti* guanines are present and at least one strand runs in a

different direction. Depending on the number of oppositely oriented strands, one can distinguish between two strands running in the reverse direction (*syn-syn-anti-anti* or *syn-anti-syn-anti*) or three strands being parallel and one facing the contrary side (*syn-anti-anti-anti* or *anti-syn-syn-syn*), which is further classified as the hybrid-type (3+1) (Figure 19) [116,121].

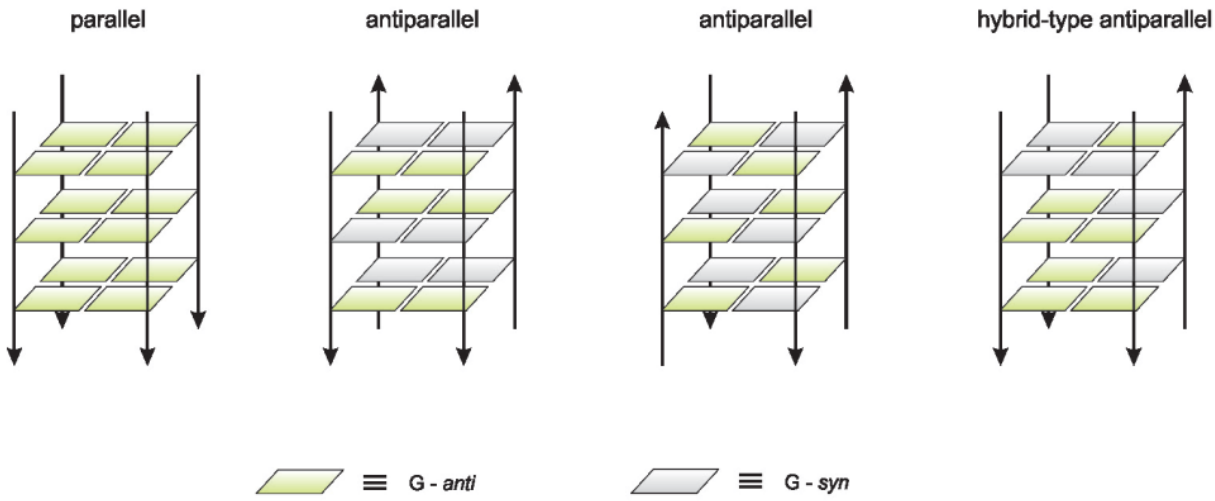

Figure 19: Different topologies of tetramolecular G-quadruplexes. Depending on the strand orientation parallel, antiparallel and hydrid-type antiparallel G4s exist [116].

Adjacent parallel G-strands are connected by propeller-type loops (also called double-chain-reversal), whereas anti-parallel strands are joined either by diagonal loops, which link two opposite antiparallel strands, or via edgewise (lateral) loops, which connect two adjacent antiparallel strands (Figure 20) [116,122,123]. The length as well as the base composition of the loop influence considerably the stability of the G4s; short loops with the presence of numerous pyrimidine bases exhibit the largest stability [124,125].

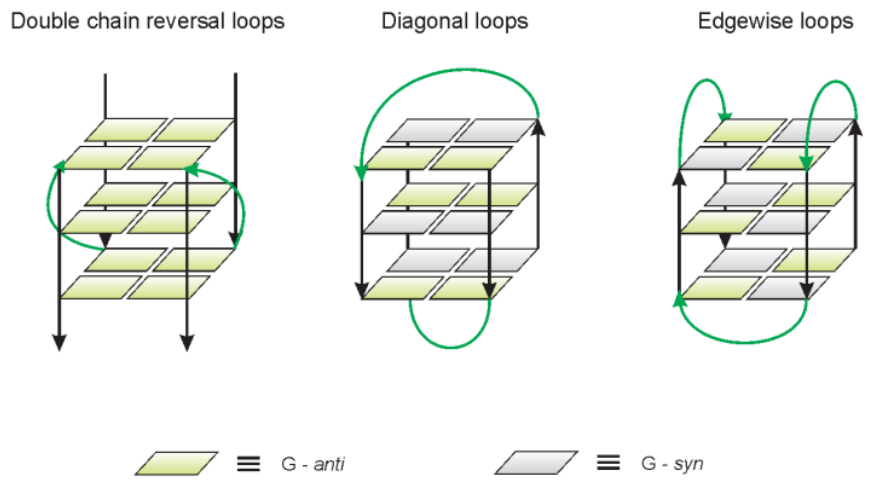

Figure 20: Different types of loops connect the G-quartets within a G-quadruplex [116]**.**

G-quadruplexes formed within DNA sequences can exhibit all different topologies. RNA G-quadruplexes on the contrary can only adopt the parallel conformation. This is because RNAs possess a ribose sugar with a 2'-hydroxyl group instead of a deoxyribose sugar in DNA, which sterically prevents the glycosidic bond *syn*-conformation, the basic requirement for antiparallel topology. Furthermore, the 2'-hydroxyl group strongly increases the thermodynamic stability and leads to a more compact and less hydrated structure compared to DNA G4s (Figure 21) [126,127].

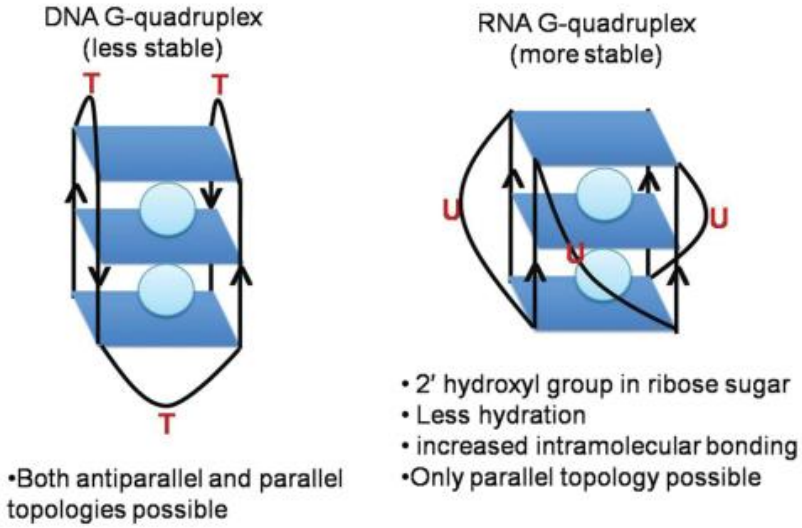

Figure 21: Dissimilarities between DNA and RNA G-quadruplexes [127]**.**

1.7.2 Characterization of G-Quadruplexes

In order to study G-quadruplex structures, a wide variety of different approaches are available (Table 1). These include biophysical techniques such as atomic force microscopy (AFM), fluorescence resonance energy transfer (FRET), circular dichroism (CD), UV spectroscopy, electrospray ionization mass spectrometry (ESI-MS) or surface plasmon resonance (SPR) as well as biochemical methods like various enzymatic and chemical procedures [128]. X-ray crystallography and nuclear magnetic resonance (NMR) are techniques which allow the structural study of G-quadruplex with exceedingly high resolution [129]. Furthermore, computational tools such as Quadparser or G4LDB can be used for instance to predict the existence of G-quadruplexes in DNA/RNA sequences or to study quadruplex–ligand interactions [130–132].

Table 1: Examples of methods frequently utilized to investigate G-quadruplexes (adapted from Kaushik et al., 2016 [128]).

S. No.	Type of technique	Examples
1.	Biophysical	**Single molecule measurements** (Atomic force microscopy, AFM; Scanning electron microscopy, SEM; Laser tweezers, Fluorescence resonance energy transfer, FRET) **Mass spectrometry** (Electrospray ionization mass spectrometry, ESI-MS) **Hydrodynamics** (Electrophoresis; Sedimentation equilibrium analysis), **Thermodynamic methods** (Melting; Differential scanning calorimeter, DSC), **Spectroscopy** (Circular dichroism, CD; Vibrational circular dichroism, VCD; UV-Vis; Infrared, IR; Raman; Fluorescence; Surface plasmon resonance, SPR)
2.	Biochemical	**Enzymatic methods** (Polymerase stop assay, Dnase I footprinting, *In situ* immunoblotting) **Chemical methods** (Dimethyl sulfate footprinting, ^{125}I-radioprobing, click reaction)
3.	High resolution	X-ray crystallography, Nuclear magnetic resonance (NMR)
4.	Computational/ Bioinformatics/ Databases	Quadparser, Quadfinder, QGRS mapper, QuadBase, QuadDB, Quadpredict, G4LDB

No universal technique exists which provides thorough knowledge about every aspect of G-quadruplexes and G4-ligand interaction. As each method provides a different piece of information, a combination of complementary approaches should be used [133].

1.7.2.1 Circular Dichroism (CD)

CD is one of the most simple and powerful tools commonly used to study the conformation of G-quadruplexes. It is a spectroscopic technique arising from the unequal absorption of right and left circularly polarized light, permitting fast and relatively inexpensive determination of the type of quadruplex fold of short as well as long DNA/RNA molecules [134,135]. Due to the structural polymorphisms of G-quadruplexes, different G4 structures exhibit unique CD spectral signatures. CD bands at 260 nm are characteristic for parallel quadruplexes and bands at 295 nm suggest antiparallel quadruplexes [133,136]. Being a very sensitive technique, it requires only low amounts of material (25 mg are sufficient) and allows working concentrations of DNA even below 20 mg/ml [137]. CD provides qualitative data about ligand interactions. For further quantitative information about kinetic or thermodynamic parameters usually other techniques like SPR or UV-Vis molecular absorption spectroscopy have been used so far [87,133,138].

1.7.2.2 UV-Visible Spectroscopy (UV-Vis)

UV-Vis spectroscopy represents a frequently used method to investigate G-quadruplex-ligand interactions and stability of G4s [133]. Furthermore, folding/unfolding kinetics of G-quadruplexes can be studied in solution by measuring the changes in absorbance at 295 nm [139]. With the application of titration experiments also information including binding constants or stoichiometric parameters can be identified [133].

1.7.2.3 Fluorescence Resonance Energy Transfer (FRET)

FRET enables structural analysis of G-quadruplexes and investigates folding transitions as well as effects of ligand interactions in a non-destructive way [140–142]. Fluorescence resonance energy transfer, also sometimes referred to as Förster resonance energy transfer as it was first examined by Theodor Förster in 1946 [143], describes the distance-dependent process of radiationless energy transfer from an excited donor molecule to an acceptor through weak dipol-dipol interactions, thereby effecting an increase in the emission of the acceptor and a simultaneous decrease of the donor's fluorescence [122,140,142]. The sample nucleic acid sequence has to be labelled with two different fluorophores, which are covalently attached to the 5' and 3' ends [133,140]. Frequently fluorescein (FAM) and tetramethylrhodamine (TAMRA) are used as a FRET pair. The crucial prerequisite for the suitability of fluorophores is that the acceptor's absorption spectrum has to overlap at least 30% with the emission spectrum of the donor (Figure 22a) [142,144,145].

Furthermore, the donor has to be in a correct parallel orientation to the acceptor and in close proximity (10-80 Å), corresponding to a radius unapproachable for other techniques (Figure 22b,c) [141,145,146].

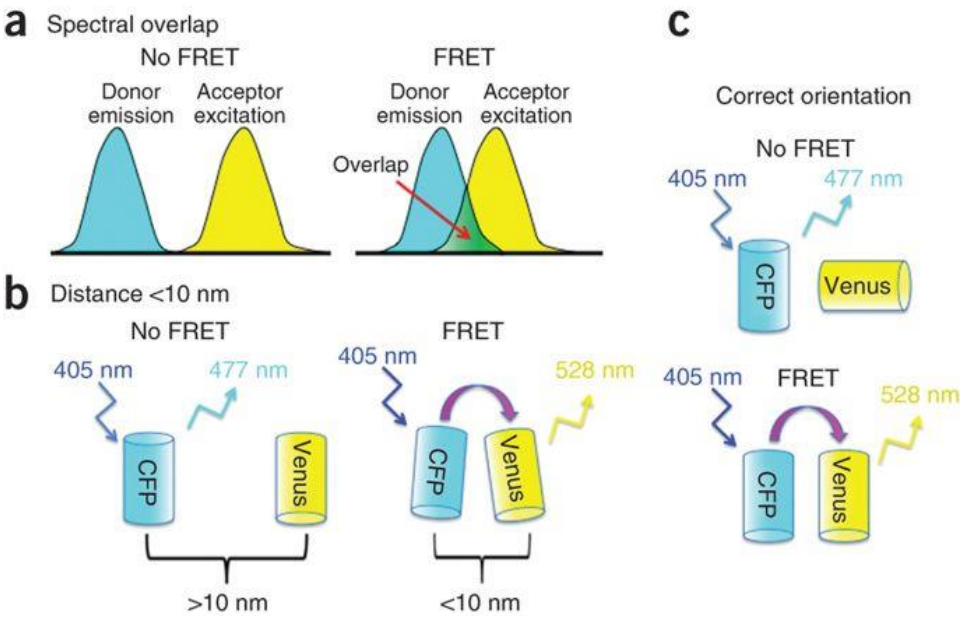

Figure 22: Requirements for efficient FRET. (a) The absorption spectrum of the acceptor needs to overlap with the donor's emission spectrum. (b) The donor must be within a distance of 10-80 Å to the acceptor. (c) Only if the dipoles are in a correct parallel orientation FRET can take place. [144]

Alterations in the donor-acceptor distance lead to a change in the energy transfer efficiency, thereby enabling to observe structural changes within G-quadruplexes or dynamics upon ligand interaction in solution [147].

1.7.2.4 X-Ray Crystallography

Single-crystal X-ray diffraction is a fundamental method for investigating G-quadruplex structures providing the highest resolution. Besides three-dimensional structures of G4s, the location of central alkali metal ions and hydration patterns can be revealed as well [116]. As the name implies, this technique depends on crystallization of the sample and concomitant exposure to X-ray beams, resulting in a diffraction pattern. By rotating the crystal, the intensities and angles of the diffracted beams can be determined and Fourier transformed to create a 3D image of the electron density within the crystal (Figure 23) [148].

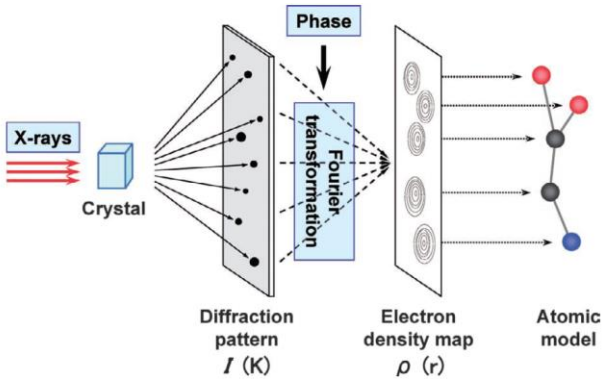

Figure 23: Single crystal X-ray analysis [149]**.**

This technique is not restricted by the molecular weight of the sample, the major bottleneck however constitutes the requirement of highly-ordered 3D crystals [150,151]. Furthermore, only information about the structure in the condensed, crystal state is obtained, which can differ considerably from the dynamic structure under physiological conditions. Therefore, X-ray crystallography is recommended to be employed as a complementary method to other biophysical and/or biochemical techniques [128,152].

1.7.2.5 Nuclear Magnetic Resonance (NMR)

NMR is a high-resolution technique to investigate dynamics of interactions including binding of ligands or folding/unfolding of G4s. The main advantage over X-ray crystallography is the opportunity to observe the samples in their physiological state in solution [116,128,153]. Therefore, the samples need to be highly purified and concentrated without aggregating [116]. The structural polymorphism of G-quadruplexes furthermore may lead to the presence of multiple species which can strongly affect the measurements. With the use of altered sequences adopting only a single conformation in solution this problem can be solved [112,154].

1.7.3 Biological Relevance

For a long time it was assumed that G-quadruplexes represent only a structural curiosity witnessed *in vitro*; as this field of research gained increasing knowledge however, it was demonstrated that these noncanonical structures also readily form *in vivo* and indeed exhibit important biological functions [111]. G4s are ubiquitous present and can be found not only in humans, but also in animals, plants, bacteria and viruses [155–161]. Recently, Chambers et al. unveiled with a high-resolution sequencing-based method that the human genome contains 716,310 putative G4 forming sequences [162]. Most importantly, these structures were shown to be non-randomly located: G-quadruplexes colocalize with functionally significant sites of the genome such as telomeres, gene promoters, both 5' and 3' untranslated regions (UTRs) or replication origins and are evolutionary conserved between species, emphasizing once again their biological significance [163,164]. In the course of extensive studies, G4s have shown to influence pivotal processes such as DNA replication, transcription, gene expression, epigenetic regulation as well as telomere maintenance and thus are considered attractive targets for the development of new anticancer agents [111,165].

1.7.3.1 Telomeres

The highest number of G-quadruplexes is reported to exist in human telomeres, where also the very first biologically meaningful G4 has been identified [111,166]. Telomeres are specialized nucleoprotein complexes which cap the ends of mammalian chromosomes and prevent them from being identified as sites of DNA damage by the DSB repair machinery and DNA damage response (DDR) enzymes, thereby protecting them from degradation and end-to-end fusion [167]. Human telomeric DNA is composed of 5-25 kb of the repetitive hexamer (TTAGGG), terminating in a 35-600 nt single stranded overhang at the 3'end, which can readily form G-quadruplexes due to its enriched guanine content [168,169]. Telomere-mediated protection is provided by the shelterin complex (also called telosome), a six-protein assembly comprising telomeric repeat-binding factors TRF1 and TRF2, TRF1-interacting nuclear factor 2 (TIN2), Ras-related protein 1 (RAP1), protection of telomeres protein 1 (POT1) as well as POT1- and TIN2-organizing protein TPP1 [170]. Shelterin is associated with telomeric DNA repeats and inhibits DNA damage sensors such as Poly ADP-ribose polymerases (PARPs) as well as the Phosphoinositide 3 (PI3)-like ATM and ATR kinases. Additionally, DSB repair through homologous recombination (HR) as well as nonhomologous end-joining (NHEJ) is impeded [170,171]. The homodimeric proteins TRF1 and TRF2 associate specifically with the ds-telomeric DNA region, while POT1 binds ss telomeric DNA. TRF2 blocks activation of the ATM kinase and assists in masking chromosomal ends by creating a large lariat-like secondary structure termed telomeric loop

(t-loop), formed through strand invasion of the 3' single stranded overhang into homologous duplex telomeric regions, concurrently replacing the duplex telomeric G-rich strand and forming a displacement loop (D-loop) (Figure 24) [172–176].

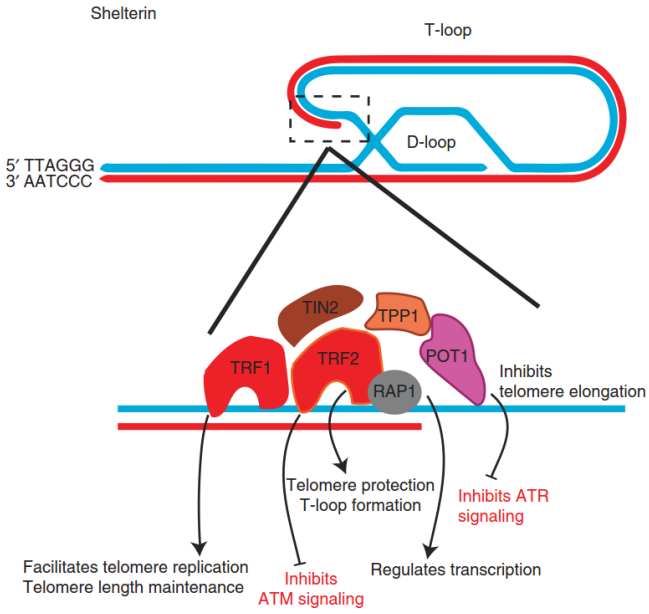

Figure 24: Association of the telomere with its hexameric shelterin complex. Adapted from Roake and Artandi, 2017 [172].

In human somatic cells, telomeric DNA is subjected to a gradual shortening of 50-200 bases with every cell division owing to the end-replication problem [168,177–179]. When the telomere length hits a critical limit, the chromosomal ends become exposed and consequently the cellular DNA-damage machinery gets activated, engaging tumor-suppressor proteins p53 and Rb1 (retinoblastoma 1) to induce apoptosis or replicative senescence [172]. This phenomenon was already observed in 1961, when L. Hayflick suggested that human cells can only divide approximately 50 times before reaching their replicative capacity, known today as the Hayflick limit [180]. In p53 and Rb-deficient cells however, telomere shortening continues beyond the senescence barrier, eventually leading to crisis, an event characterized by massive cell death and severe chromosomal instability due to fusion events generating dicentric chromosomes and initiating breakage-fusion-bridge (BFB) cycles [167,172,181,182]. However, sometimes malignant cells can persevere crisis to achieve limitless replication potential, which is accomplished through so called "Telomere Maintenance Mechanisms (TMMs)" (Figure 25) [183].

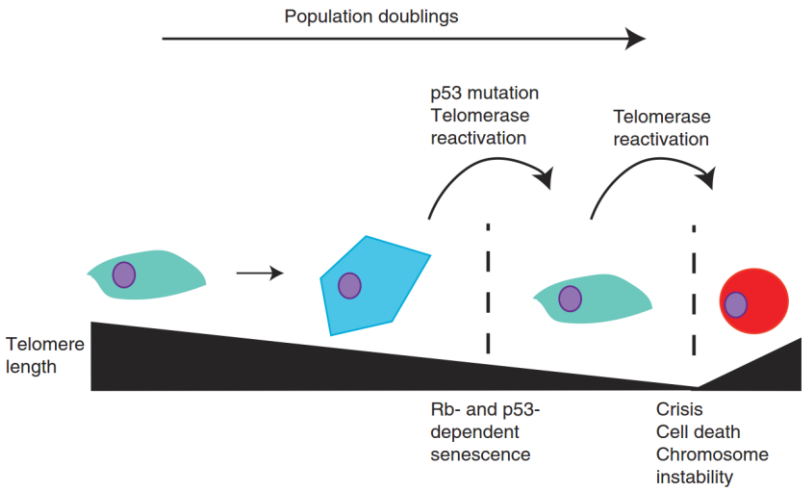

Figure 25: Telomeres act as a mitotic clock. With each cell division, telomeric DNA is exposed to a progressive shortening until the cellular DNA-damage machinery is recruited, which induces apoptosis or replicative senescence through p53 and Rb1. Lack of these two tumor-suppressors or upregulation of telomerase allow the cells to circumvent senescence and divide further, eventually reaching a point of extensive telomere dysfunction called crisis. Through reactivation of telomerase or ALT, cells can survive and acquire the ability of limitless replication, the fourth hallmark of cancer [172].

For a long time, it was supposed that in 85% of cancer cells, telomere length is maintained through activation of the enzyme telomerase, while 15% of cells use a telomerase independent mechanism known as alternative lengthening of telomeres (ALT), which is based on homologous recombination [184–186]. In 2017 though, Barthel et al. provided evidence that only 73% of 6,835 investigated cancers upregulate telomerase and 5% use the ALT pathway [187]. The residual 22% did not show activation of any of these two mechanisms, suggesting that certain tumor cells are either able to acquire immortality without any of these two TMMs or that a third, still undiscovered process exists. Moreover, co-existence of ALT and telomerase mechanisms as well as the potential of certain tumor cells to switch between them was reported [183,188,189].

Telomerase is a RNA-dependent DNA polymerase that utilizes its catalytic component, called hTERT in human, to reverse transcribe the template region of its own RNA subunit (termed hTR or hTERC) onto the 3' end of the telomeric DNA. For *in vivo* functionality, this holoenzyme requires association with further components such as the auxillary protein dyskerin and H/ACA ribonucleoproteins (RNP) including NHP2, NOP10, and GAR1 (Figure 26) [190]. Telomerase is recruited from Cajal bodies to telomeres through TCAB1 (Telomerase CAjal Body protein 1), which is mediated by the shelterin component TPP1 [173,191].

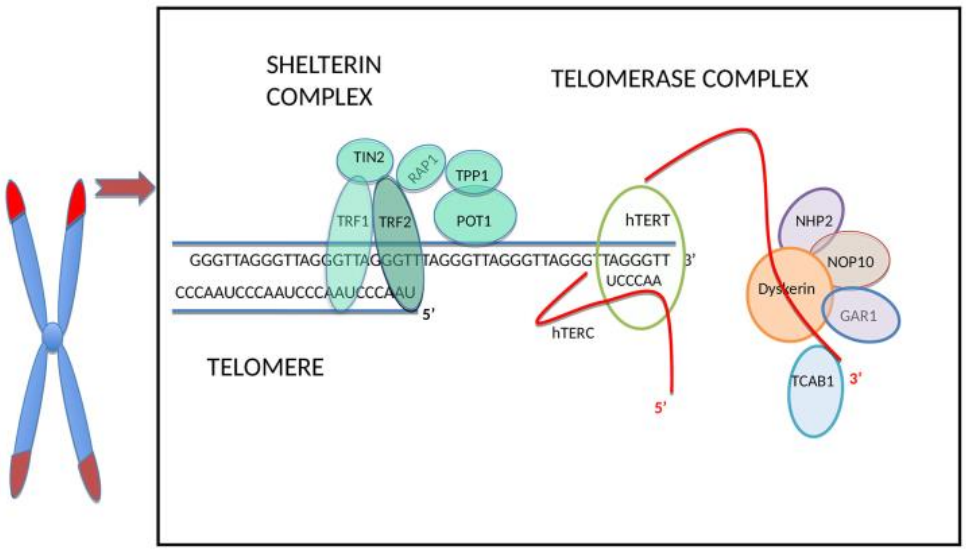

Figure 26: Interplay between telomere and telomerase complex [190]**.**

In non-malignant somatic cells, telomerase activity is absent due to downregulation of hTERT. Therefore, pharmacological targeting of telomerase represents a promising target in anticancer therapy with minor suspected cytotoxic side effects to healthy cells [192,193]. Exceptions include embryonic stem cells, germ-line cells, activated lymphocytes and other highly proliferative cells, where telomerase is also active [194,195]. However, as telomere length of these cells diverges significantly to those of cancer cells, the attrition to a critical level takes much longer and thus would not hinder telomerase-targeted therapy [193].

One way to inhibit telomerase activity can be achieved via stabilization of G-quadruplex structures formed in the 3'-single-stranded overhang of telomeric DNA. Promoting the formation of G-quadruplexes and stabilizing these structures with small molecule ligands can impede telomerase activity and effect apoptosis in cancer cells [196–198]. Importantly, G-quadruplex-interactive ligands were shown to inhibit the ALT pathway as well, avoiding potential drug resistance via switching between telomere maintenance mechanisms (Figure 27) [193,199].

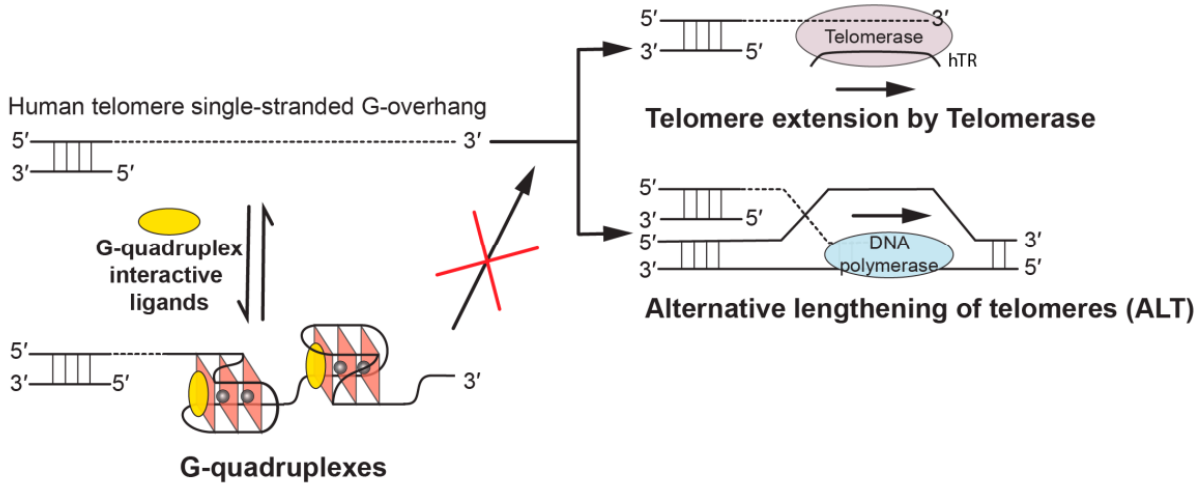

Figure 27: Inhibition of both telomere maintenance mechanisms via stabilization of telomeric G-quadruplexes using small molecule ligands [199]**.**

1.7.3.2 Oncogene Promoters

Besides telomeres, human gene promoters have been shown to be a further region particularly abundant in G-quadruplex sequences. Huppert et al. discovered with the Gene Ontology (GO) database [200] that especially genes depending on tight control involved in vital processes such as development, cell differentiation and neurogenesis possess putative quadruplex sequences (PQS) in their promoter regions [119]. Furthermore it was revealed via the bioinformatics tool quadparser (Table 1) that 42.7% of human gene promotors contain at least one quadruplex motif, whereas the number of PQS in proto-oncogenes even accounts for 69% [201]. Whereas telomeric G4 forming regions are already accessible in a single-stranded form, G-rich sections in gene promoter sequences are impeded with their C-rich complementary strands due to the double-stranded character of genomic DNA, which renders assembly of a G-quadruplex structure decisively more challenging and a competition with the duplex Watson-Crick pairing [202]. Therefore, a prerequisite for G4 formation is local strand separation, which takes place at transcription initiation, where duplex DNA is opened transiently to form a transcription bubble, exposing single-stranded regions capable of forming G-quadruplexes [203,204]. These G4 structures within promoter regions have shown to regulate the expression of genes in both positive and negative directions and can thus act as a molecular switch to modulate transcription (Figure 28) [119,204].

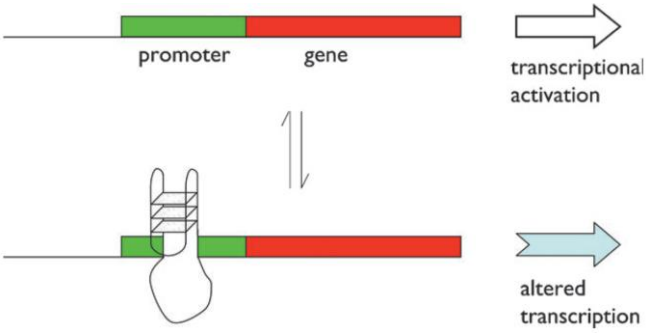

Figure 28: G4 formation in promoter regions serves as a molecular switch to modulate transcription [119]**.**

More precisely, depending on the position of the G-quadruplex different scenarios exist: G4s upstream of the transcription start site (TSS) positively influence transcription when they aid in recruiting or binding specific transcription factors, while they have a negative impact when G4s act as a steric block to transcription, hindering binding of the RNA-Polymerase II (RNAP II) or transcription factors (Figure 29i) [198,204,205]. G4 structures downstream TSS on the other hand can act as transcriptional enhancers, when they are found in the coding strand, maintaining the template strand in its single stranded form and thus promoting transcription re-initiation. When located in the template (non-coding) strand, G4s may hinder recognition of RNAP II or stall its progression (Figure 29ii), acting as transcriptional repressors [198,204,205]. Additional stabilization with a small molecule ligand promotes G4 folding and shifts the equilibrium towards G4s [119].

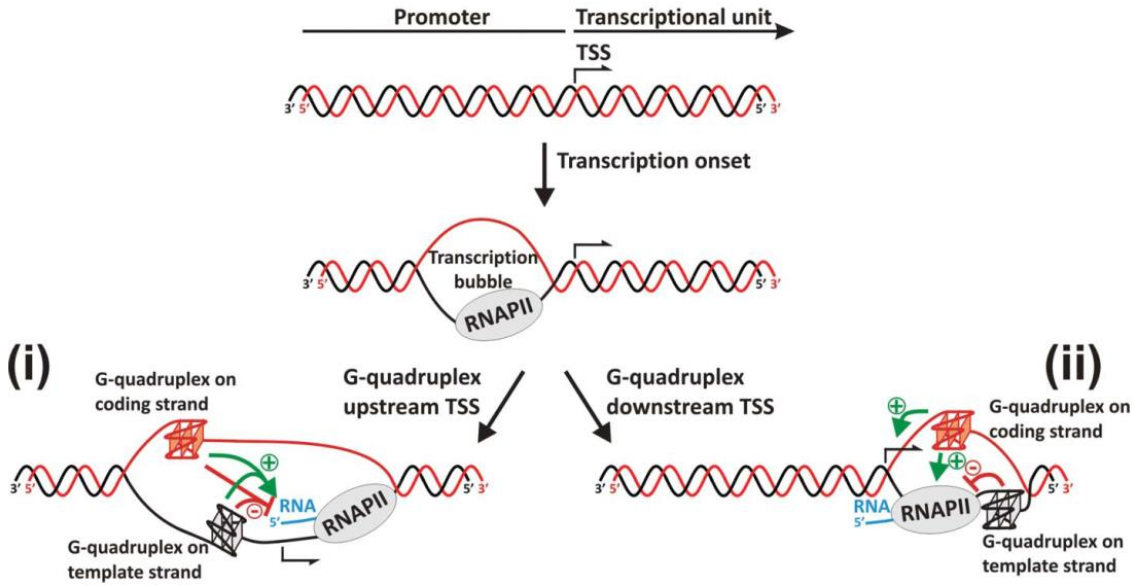

Figure 29: Influence of G-quadruplex structures on transcriptional level. G4s can be formed either **(i)** upstream or **(ii)** downstream of the transcription start site (TSS) and influence transcription in both positive and negative directions [204].

While tumor-suppressor genes barely contain putative G4 forming motifs in their promoter regions, promoters of proto-oncogenes are very abundant in PQS [206]. Noteworthy, these include genes that are linked to the six originally described hallmarks of cancer discussed in Chapter 1.3, such as c-MYC, c-KIT and KRAS (self-sufficiency), pRB (insensitivity), Bcl-2 (evasion of apoptosis), VEGF-A (sustained angiogenesis) hTERT (limitless replication potential) and PDGF-A (tissue invasion and metastasis) (Figure 30) [207,208].

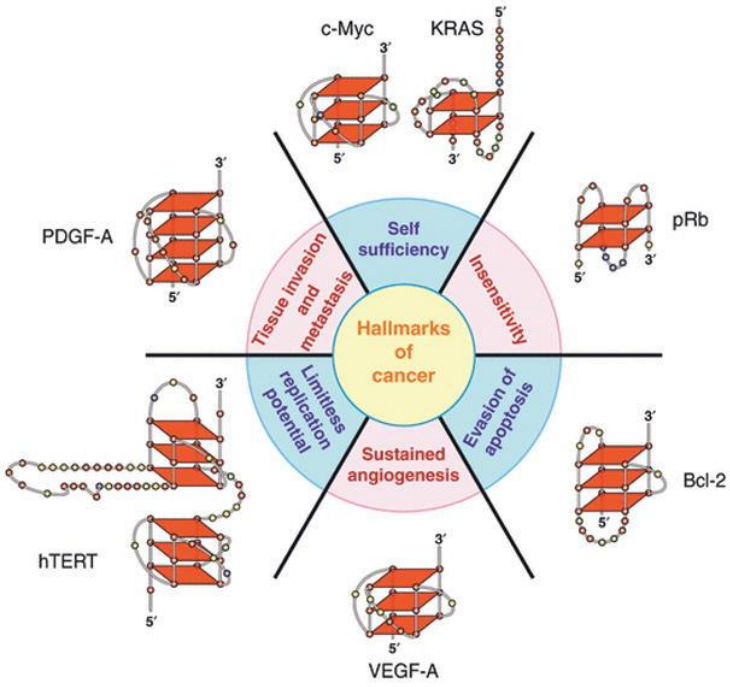

Figure 30: The six original hallmarks of cancer linked to important proto-oncogenes exhibiting G-quadruplex sequences in their promoter regions [207]**.**

An extensively studied model for transcriptional enhancement represents the c-KIT promoter, which possesses a G-rich consensus site (5'-GGGCGGG-3') for the transcription factor SP1 (specificity protein 1), able to readily form G4 structures. This G4 motif has been identified as a high-affinity binding site for SP1, facilitating the recruitment of the transcription factor and thereby enhancing transcription (Figure 31) [205]. Similarly, the KRAS promoter comprises a G-rich tract termed 32R that concurs with a nuclease hypersensitivity region and a consensus sequence of 5'-GGG(A/C)GG-3' for the transcription factor MAZ (Myc-associated zinc finger protein). Via stabilization of the 32R G-quadruplex structure binding of MAZ can be facilitated and overall transcription efficiency improved. In contrast, interference of the G4 assembly has been documented to reduce KRAS transcription (Figure 31) [205,209–211].

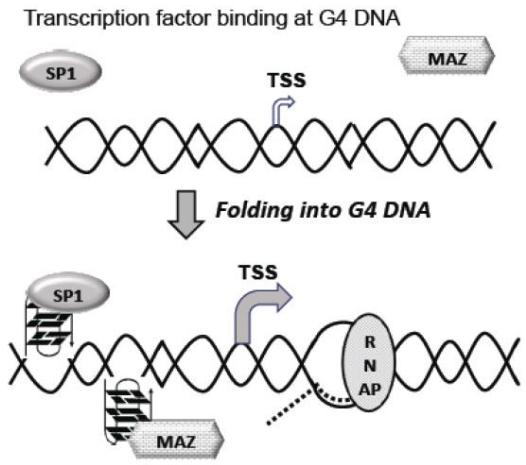

Figure 31: G-quadruplexes can enhance transcription by facilitating transcription factor binding. The c-KIT promoter region contains a G-rich consensus sequence for transcription factor SP1, which enhances its binding efficiency upon G4 formation. Similar can be observed for KRAS promoter and transcription factor MAZ [205]**.**

1.7.4 Targeting G4s with Small Molecules

As G-quadruplexes are involved in several physiologically and pathologically relevant processes, targeting these non-canonical secondary structures has been considered a promising strategy in anticancer drug development. Therefore, intensive research has been directed toward the design of G-quadruplex interactive ligands and a considerable number of small molecule ligands have been developed over the past two decades [212,213]. In addition to stabilizing G-quadruplex structures, these ligands should be selective for quadruplex over duplex DNA, which remains a very complex and challenging tasks due to the structural polymorphisms of G4s [154]. In general, ligands can be discriminated by their different binding modalities, which include external binding via stacking on G-tetrads, intercalation between G-quartets as well as nonspecific interaction with grooves or loops (Figure 32) [214].

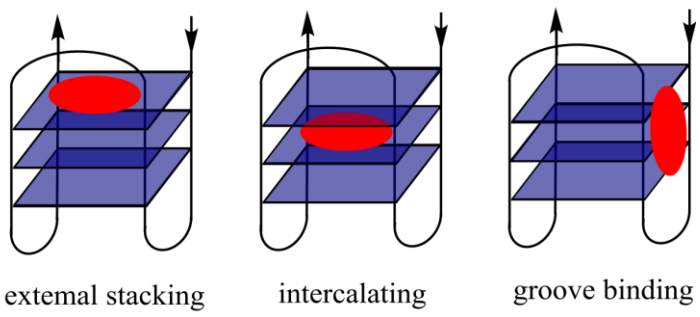

Figure 32: Different binding modes of G-quadruplex ligands [214]**.**

Intercalation is considered as a rather unlikely scenario due to the pronounced rigidity of G4 structures and the concomitant high energy demand required to unstack two quartets and displace the stabilizing central cation. Accordingly, external π–π stacking on top or bottom of a G4 is energetically more favourable and thus the most commonly observed and best characterized mode of G4 ligand binding [122]. To realize this, ligands are frequently designed to exhibit large planar aromatic surfaces subjected to interact preferably with the big hydrophobic G-tetrad surface. As this impairs the ligand's water solubility, protonable substituents are added around the aromatic core to improve the hydrophilicity of the ligand. This can be achieved via *in situ* protonation, aromatic N-methylation or the imbedding of a central metal [215]. Well-established examples include ligands such as TMPyP4 [216–218], BRACO-19 [219–221], BMVC4 [222] or Pyridostatin (PDS) [223,224], but also neutral ligands like Telomestatin [225] have been developed (Figure 33) [198,215,226]. Interestingly, for BRACO-19 all three binding modes have been reported [227].

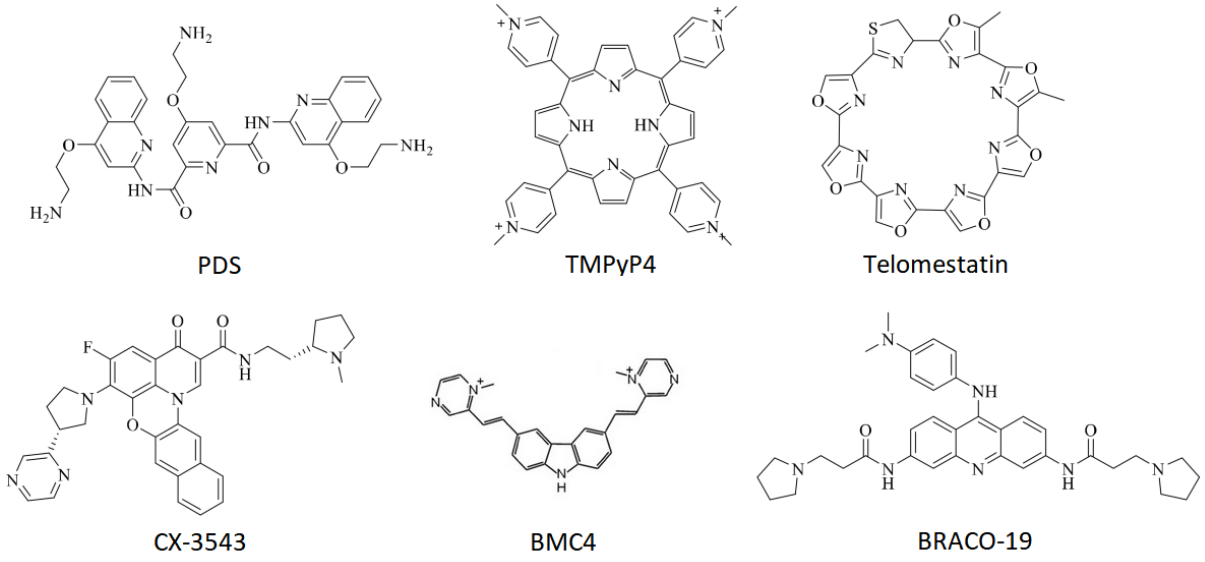

Figure 33: Chemical structures of well-established G-quadruplex ligands. Adapted from Sun et al., 2019 [198].

1.7.4.1 Quarfloxin (CX-3543)

To date only one G4 ligand – Quarfloxin (also called CX-3543) – has advanced to phase II clinical trials for neuroendocrine and carcinoid tumors (ClinicalTrials.gov Identifier: NCT00780663) [228], even though unsuccessful owing to excessive albumin binding [229]. Quarfloxin is believed to act through disrupting the interaction between nucleolin and G4 in the ribosomal DNA (rDNA) template in the nucleolus, which causes relocalization of nucleolin from the nucleus into the nucleoplasm, where it binds to c-MYC G4 and blocks transcription, resulting in apoptosis of tumor cells (Figure 34) [230].

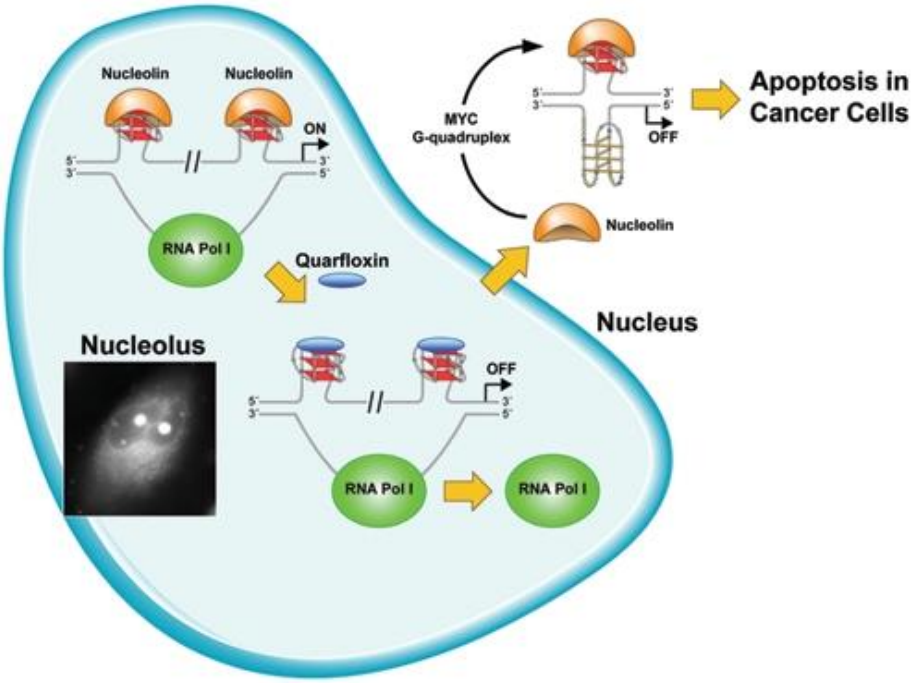

Figure 34: Quarfloxin exerts its anticancer activity through redistribution of nucleolin into the nucleoplasm, leading to downregulation of c-MYC expression and apoptosis [230]**.**

1.7.4.2 Pyridostatin (PDS)

Pyridostatin is a small molecule based on a *N*,*N*'-bis(quinolinyl)pyridine-2,6-dicarboxamide scaffold, exhibiting a planar electron-rich aromatic surface and rotable bonds, which enables the ligand to cope with the structural polymorphisms of G4 structures and to π–π stack on G-quartets (Figure 35) [212,231].

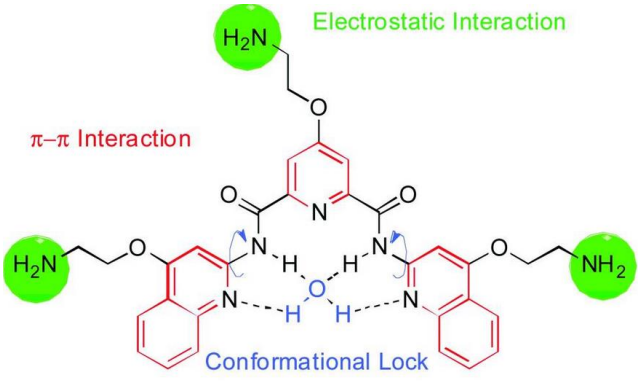

Figure 35: Structural characteristics of pyridostatin [231]**.**

PDS is highly selective for G4s over duplex DNA and to interact with human cancer cell telomeres, modifying the integrity of the shelterin complex through POT1 uncapping and inducing ATR-mediated DDR [212,223,232].

1.7.4.3 TMPyP4

The cationic porphyrin 5,10,15,20-tetra(N-methyl-4-pyridyl)porphyrin (TMPyP4) represents one of the best studied G4 ligands, with the ability to stabilize both parallel and antiparallel G-quadruplexes. A big disadvantage however poses its low selectivity for G4s regarding duplex DNA, which could be a result of the side arm substituents being too small [212,233]. The G4 ligand downregulates c-myc expression and inhibits telomerase by blocking hTERT expression [212,217]. TMPyP4 further acts through activation of p38 MAPK, a major signaling pathway involved in apoptosis of tumor cells, resulting in *in vivo* antitumor activity of human cervical cancer cells [234–236]. Moreover, TMPyP4 has shown to alter cell adhesion and migration as a side effect [237,238].

1.7.5 Fluorescent Probes for G-Quadruplex Recognition

In addition to G4 stabilizing ligands, G4 interacting probes exhibiting fluorescence properties have emerged in the last years, providing a pivotal opportunity to further elucidate the biological role of G-quadruplexes *in vivo*. In general, visualization of G-quadruplexes can be achieved by different methods, including immunofluorescence, *in situ* fluorescence tagging of G-quadruplex ligands or intrinsically fluorescent small molecule G4 ligands [239]. The very first G-quadruplex specific antibody, Sty49, was developed in 2001 and used to visualize G-quadruplex structures in protozoa [240]. In 2013, Biffi et al. developed a new G4-specific antibody, BG4, from a Sanger phage display library for direct visualization of DNA and RNA G-quadruplexes in fixed human cells and metaphase chromosomes, which is commercially available and opens new avenues in the study of G-quadruplexes in human cancer cells (Figure 36) [241,242].

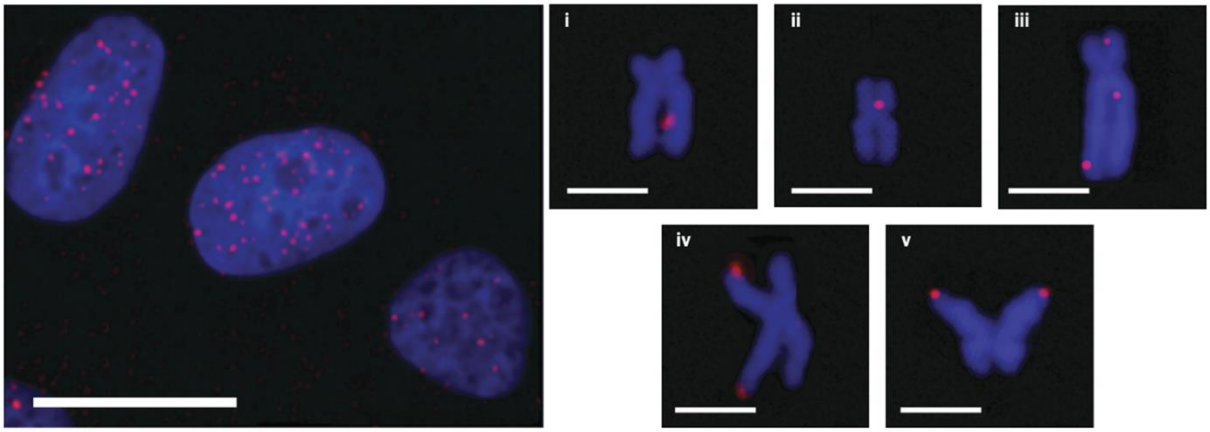

Figure 36: Visualization of G4 structures in human cancer cell nuclei and metaphase chromosomes with the G4 selective antibody BG4. Adapted from Biffi et al., 2013 [241]**.**

Only one year later, Henderson et al. developed 1H6, another monoclonal antibody used for detection of DNA G-quadruplex structures [243]. In 2017 however, the author expressed a note of concern mentioning that 1H6 also cross-reacts with adjacent thymidines in ssDNA [244,245]. Furthermore, so-called "light up" and "light off" probes have evolved, which exhibit either a strong fluorescence increase or quenching upon interaction with G-quadruplexes (Figure 37). "Light up probes" are the better choice, resulting in less false-positive signals. Most importantly, these sensors enable the investigation of G-quadruplexes in living cells, contrary to immunofluorescence, which is limited to fixed cells due to insufficient cell-permeability of antibodies [120,246,247].

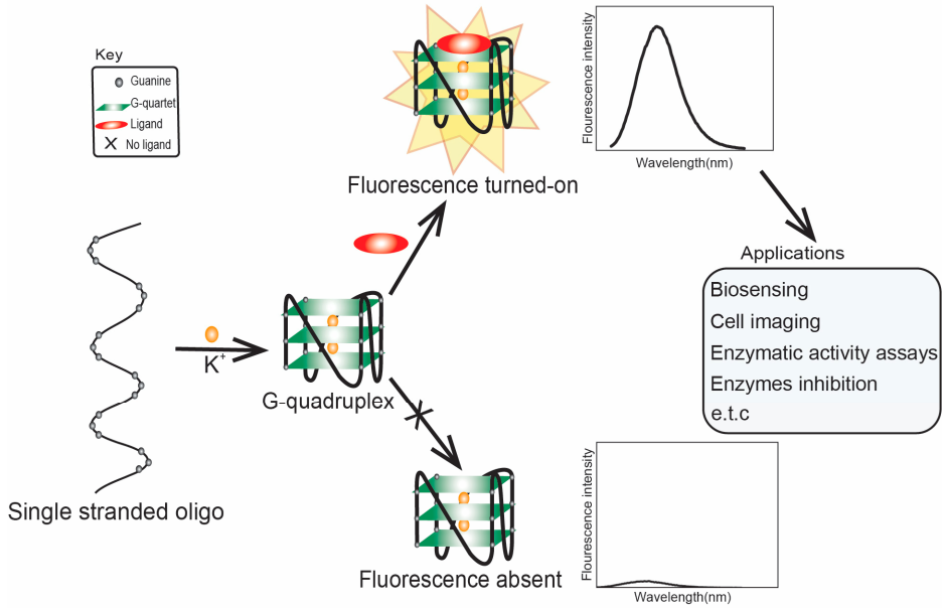

Figure 37: G4 selective light-up probes. Upon interaction with G-quadruplex structures fluorescence is "switched on", enabling detection of G4s in living cells [247]**.**

An excellent probe should display several desired characteristics, such as low self-fluorescence, strong fluorescence-enhancement upon G4 binding, pronounced selectivity for G4 over duplex or other types of DNA, sufficient membrane permeability to access living cells, low tendency for off-target binding to minimize background noise, minor cytotoxicity and phototoxicity as well as distinct photostability. Hence, it is not surprising that up to now a perfect G4 visualization probe does not exist and much effort is still required for the design of new, improved fluorescence probes [120]. Moreover, it still needs to be clarified whether prevalent G4 visualization tools can recognize single G-quadruplexes or only regions of tightly clustered G4s [248]. Most G4 selective fluorescence probes, similar as the G4 ligand Quarfloxin mentioned earlier, were reported to localize inside the membrane-less nucleoli within the cell nucleus. The nucleolus is the site of ribosome biogenesis and composed of rDNA, rRNA (ribosomal ribonucleic acid) as well as nucleolar proteins, with rDNA being

especially rich in GC sequences and prone to form G-quadruplex structures [249,250]. An example for a well-established and commercially available "light up" probe which also localizes in the nucleoli is Thioflavin T (ThT), a benzothiazole dye which selectively recognizes DNA and RNA G-quadruplexes (Figure 38) [251,252].

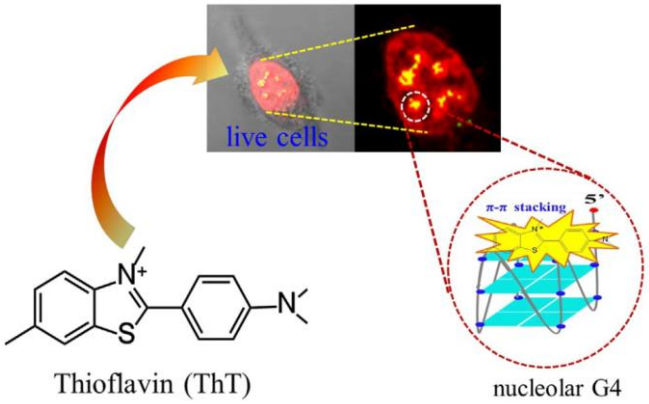

Figure 38: Molecular structure and light-up effect of Thioflavin T (ThT) in nucleolar G-quadruplexes [251]**.**

Interestingly, the G4-selective antibody BG4 was originally described to generate punctate staining pattern all over the nucleus and cytoplasm in paraformaldehyde (PFA)-fixed cells (Figure 36 and Figure 39, left picture) [241]. However, recent studies by Laguerre et al. showed that after methanol (MeOH) fixation the antibody preferentially labels nucleoli as well (Figure 39, right picture) [253,254].

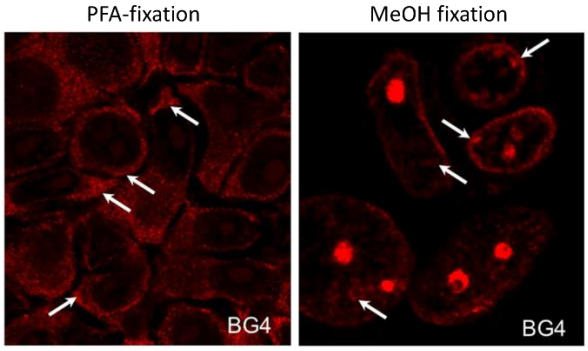

Figure 39: BG4 antibody staining depends on the fixation method. While in PFA fixed cells a diffuse punctate staining pattern inside the nucleus and cytoplasm is observable, MeOH fixed cells reveal a clear-cut labelling of nucleolar regions. White arrows are not relevant in this context. Adapted from Laguerre et al., 2016 [254].

1.8 Aim of the Study

G-quadruplexes aroused considerable interest during the last years as innovative anticancer targets based on their impact on several regulatory biological processes, such as telomere maintenance, DNA replication, transcription and gene expression, rendering the rational design of G4 targeting small molecule ligands a promising approach for the development of new anticancer agents. Based on a recent report of self-assembled Pt_2L_2 boxes targeting G-quadruplex structures [255], a new improved version with fluorescence properties was synthesized, lacking biological studies.

Hence, the goal of this study was to investigate the practicability of this newly synthesized compound for anticancer therapy. Therefore, the impact of the Pt_2L_2 metallacycle on tumor and non-malignant cell viability, proliferation and cell cycle were tested with MTT-based as well as clonogenic assays and flow cytometry. Differences between the Pt_2L_2 assembly and the free ligand were determined to investigate potential cellular dissolution of the platinum complex into its basic constituents. Furthermore, the in-solution fluorescence characteristics and drug uptake kinetics of the Pt_2 metallacycle were studied within the intracellular milieu and its specific emissive behavior determined via lambda emission fingerprinting and flow cytometry. Moreover, cellular uptake and in-cell localization of the drug was explored in (i) living cells (ii) fixed cells as well as (iii) human metaphase chromosomes, exploiting different microscopy techniques including live cell imaging, fluorescence microscopy, CLSM as well as airyscan super-resolution microscopy. Specific organelle markers were used to elucidate the final target of the compound. The cellular distribution pattern was further compared with that of a G4 selective antibody and competition with other well-known G4 ligands as well as G4-unselective, standard chemotherapeutics was investigated. Furthermore, the impact of the compound on G4 regulated genes was assessed via whole genome gene expression microarray and the results compared to the effects of other well-established G4 ligands.

2 Material and Methods

2.1 Cell Culture

All cell lines used during this project were cultured in T25 and T75 cell culture flasks in their respective growth media (Table 2) supplemented with 10% fetal bovine serum (FBS, Sigma-Aldrich, Missouri, USA) without the addition of antibiotics or antimycotics and incubated in a humidified atmosphere at 37°C and 5% CO_2. Every cell line was passaged twice a week and constantly monitored with a Zeiss PrimoVert microscope (Carl Zeiss microscopy, Germany).

Table 2: Overview of the different cell lines used in this project

Cell line	Disease	Tissue	Growth medium	Source
U2OS	Osteosarcoma	Bone	IMDM (Sigma-Aldrich)	ATCC
MCF-7	Adenocarcinoma	Mammary gland, breast	DMEM (Sigma-Aldrich)	ATCC
T98G	Glioblastoma multiforme	Brain	MNP (Sigma-Aldrich)	ATCC
U373MG	Glioblastoma astrocytoma	Brain	MNP (Sigma-Aldrich)	ATCC
VM-1	Melanoma	Skin	RPMI 1640 (Sigma-Aldrich)	ICR
HaCaT	Keratinocytes, non-malignant	Skin	RPMI 1640 (Sigma-Aldrich)	Prof. Fusenig, DKFZ Heidelberg
HLF	Fibroblasts, non-malignant	Lung; pneumothorax	RPMI 1640 (Sigma-Aldrich)	ICR

VM: Vienna Melanoma
IMDM: Iscove's Modified Dulbecco's Medium
DMEM: Dulbecco's Modifies Eagle's Medium
MNP: Modified Eagle's Medium supplemented with 0.2% Na-pyruvate and 1% non-essential amino acids
RPMI: Roswell Park Memorial Institute
ATCC: American Type Culture Collection
ICR: Institute for Cancer Research, Vienna
DKFZ: Deutsches Krebsforschungszentrum, Heidelberg

2.2 Cell Viability and Proliferation Analyses

2.2.1 Cell Viability Assay (MTT)

Background

Cell-based assays can be used to assess the activity of anticancer compounds on different cell lines and to determine their effect on cell proliferation and cell viability. The most commonly used viability assay is the colorimetric 3-(4,5-dimethylthiazol-2-yl)-2,5-diphenyltetrazolium (MTT) assay, which was developed by Tim Mosmann in 1983 [256]. MTT is a water-soluble tetrazolium salt, which is positively charged and can easily penetrate viable cells. Cellular oxidoreductase enzymes in their active metabolism further lead to a NADH-dependent cleavage of the MTT's tetrazolium ring into an insoluble purple colored formazan product (Figure 40). Dead cells lose this ability, which is why the color formation serves as a suitable indicator for the amount of viable cells [257,258]. The color intensity of the formazan product is quantified colorimetrically by measuring at 450nm and 620nm as a reference wavelength using a plate reading spectrophotometer.

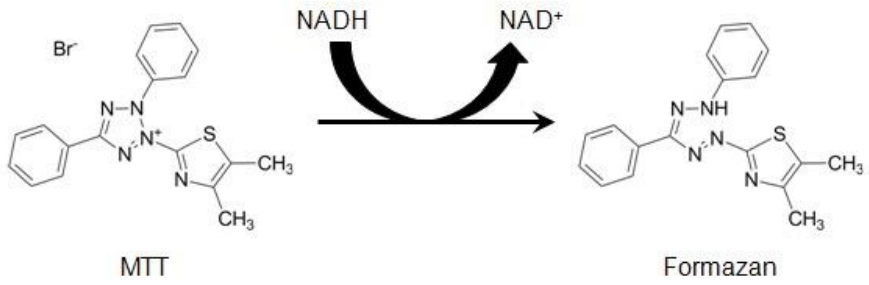

Figure 40: NADH-dependent reduction of MTT to formazan. The ability to cleave the tetrazolium ring of the MTT into a purple colored formazan is a marker for the viability of cells and can be measured colorimetrically [258].

Procedure

2-3 x 10^4 cells were seeded in 100 µl respective growth media (Table 2) in 96-well plates. After overnight attachment in a humidified atmosphere at 37°C and 5% CO_2, cells were treated in triplicates with 100 µl of the investigated anticancer compounds in successively increasing concentrations. After 72h drug exposure under standard cell culture conditions, cells were checked under the microscope (Zeiss PrimoVert microscope, Carl Zeiss microscopy, Germany) and the number of viable cells was determined by MTT-based assay following manufacture's guidelines (EZ4U, Biomedica, Vienna, Austria). After an incubation time of 0.5 to 3 h, depending on the cell line and their metabolic activity, the color intensity of the formazan product was measured

spectrophotometrically at 450 nm and 620 nm as a reference wavelength (Tecan infinite 200 pro, Lifesciences, Switzerland or Asys Expert Plus Microplate Reader, Biochrome Camborne, Cambridge, UK). The activity of the compounds was calculated using the software GraphPad Prism 5.0 (La Jolla, CA, USA) and expressed as half maximal inhibitory concentrations (IC_{50}) values.

2.2.2 Clonogenic Assay

Background

The clonogenic assay, also known as colony forming assay, was firstly described in 1956 [259]. It is based on the ability of a single cell to form a colony, which per definition consist of a minimum of 50 cells. The assay is therefore a simple and frequently used technique to assess the impact of anticancer compounds on the proliferation of tumor cells [260].

Procedure

Cells were seeded at very low cell densities of $1x10^3$ (U2OS) and $2x10^3$ (MCF-7) per ml in their respective growth media in 24-well plates and incubated overnight under standard culture conditions. On the next day the plates were checked for single cells in all wells using the Zeiss PrimoVert microscope (Carl Zeiss microscopy, Germany), treated with the investigated drugs in different concentrations and incubated for 7 days. Afterwards cells were washed with phosphate-buffered saline (PBS) and fixed with prechilled methanol for at least 20 minutes at 4 °C. Following another PBS-washing step, cells were stained with crystal violet (0.1 mg/ml) for a few minutes. Excess crystal violet dye was removed by washing with H_2O. After air-drying of the plates pictures of each well were taken (Nikon Digital Camera D3200, Minato, Tokyo, Japan). The plates were additionally scanned on the Typhoon scanner (Typhoon TRIO Variable Mode Imager, GE Healthcare Life Sciences). By calculating the integrated area densities with the ImageJ 1.51f software (Wayne Rasband, National Institutes of Health, USA), colony growth was determined. Data illustration was performed using GraphPad Prism 5.0 software (La Jolla, CA, USA).

2.3 Flow Cytometry

2.3.1 Flow Cytometric Fluorescence Intensity Measurements

Background

Flow cytometry represents a popular cell analysis technique to count and sort cells in a heterogeneous fluid mixture. In a flow cytometer, a cell suspension is funneled through the center of a narrow, fast flowing liquid stream where one cell at a time is passed through a laser light beam. With the help of electronic detectors, fluorescence emission signals and any deviation from the light path, also known as scattering, are measured (Figure 41) [261,262].

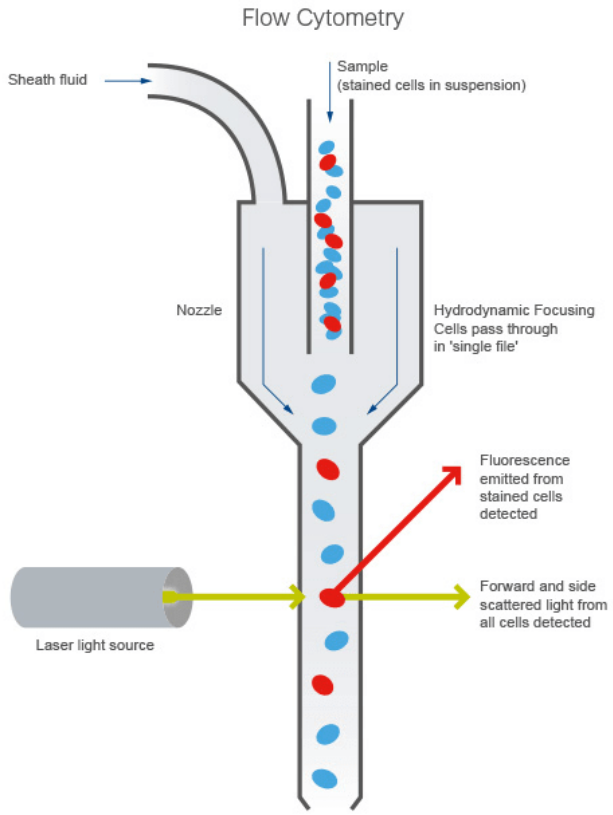

Figure 41: Flow cytometer. Once the cell suspension enters, it is focussed hydrodynamically by sheath fluid through a nozzle so that only one cell at a time is passed through a laser light beam [263].

The light scatter along the path of the laser is defined as the forward scatter (FSC) and provides information about the size of the cell. The scatter at a 90° angle is referred to as the side scatter (SSC), which in contrast describes the internal complexity of the cell (Figure 42). The combination of these two measurements already enables to a certain extend the differentiation of cells within a heterogeneous population [261,262].

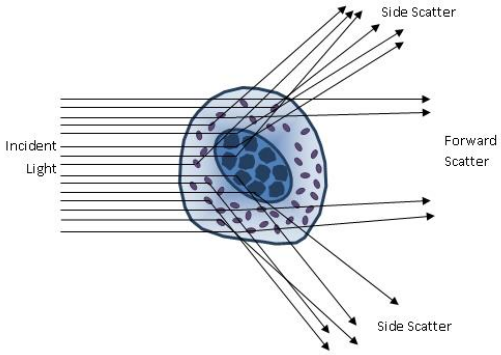

Figure 42: Light scattering. The forward scatter correlates to the cell size, while the side scatter describes the granularity of the cell [262]**.**

Procedure

Untreated cells or cells pretreated with varying concentrations of a G-Quadruplex stabilizer ($TMPyP_4$) for 24h under standard cell culture conditions were trypsinized and centrifuged with 240g for 8 minutes. After removing the supernatant cells were resuspended in 300µl FACS (fluorescence-activated cell sorting)-PBS and incubated protected from light with the investigated drugs in different. Fluorescence intensity measurements were carried out after 5 min and after 60 min drug incubation with flow cytometry (FACS Calibur – Becton Dickinson, Palo Alto, CA) and analysed using Flowing Software 2.5.1 (Perttu Terho, Turku, Finland). Data illustration and statistical analysis were performed with GraphPad Prism 5.0 software (La Jolla, CA, USA).

For drug uptake measurements, untreated U2OS cells were trypsinized and centrifuged with 240g for 8 minutes. After removing the supernatant cells were resuspended in serum-free RPMI 1640 media (Sigma-Aldrich, Missouri, USA) containing 3-(N-morpholino)propanesulfonic acid (MOPS; Sigma-Aldrich, Missouri, USA) and 4-(2-hydroxyethyl)-1-piperazineethanesulfonic acid (HEPES; Sigma-Aldrich, Missouri, USA). The cell suspension was then transferred into FACS tubes (400 µl each) and the investigated drugs were added in a concentration of 50 µM and 10 µM. Fluorescence intensity was measured with flow cytometry (FACS Calibur – Becton Dickinson, Palo Alto, CA) after 5, 15, 30, 60 and 120 min drug exposure and analysed using Flowing Software 2.5.1 (Perttu Terho, Turku, Finland). Data illustration and statistical analysis were performed using GraphPad Prism 5.0 software (La Jolla, CA, USA).

2.3.2 Flow Cytometric Cell Cycle Analysis with Propidium Iodide (PI) Staining

Background

Flow cytometry can further be used to assess the cell cycle distribution of a population. A proliferating cell passes during cell cycle progression G1 - S - G2 - M phases for DNA replication, mitosis and subsequent division into two daughter cells [264]. By using a DNA-binding fluorescent dye, the cellular DNA content of the cells can be measured and thereby information about their ploidy, position in the cell cycle and amount of apoptotic cells is gathered [265]. However, the DNA content alone only allows differentiation between G1/G0 versus S versus G2/M phase (Figure 43) and further analysis of e.g. the protein expression is needed to confirm the results. In anticancer drug development this technique represents a valuable tool to understand the effect of certain compounds on cell cycle progression, an important target in oncology research.

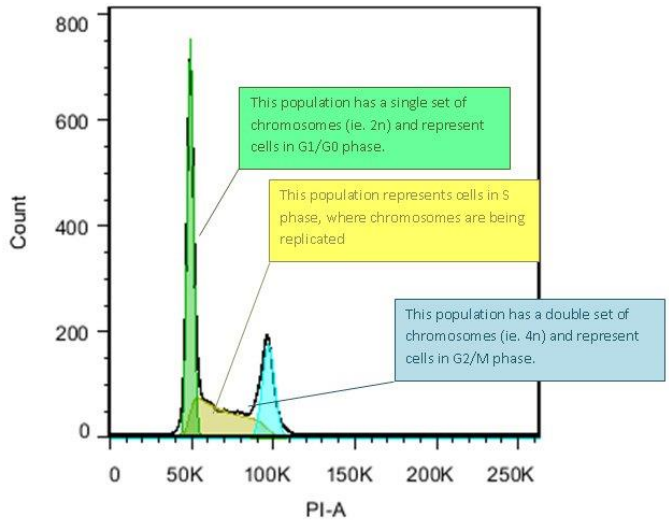

Figure 43: DNA histogram of PI stained cells analysed with flow cytometry. The first peek in green refers to the diploid chromosome content of cells in the G1/G0 phase. The yellow population in the middle represents cells in the synthesis phase (S-phase) followed by the peak in blue indicating a double set of chromosomes (G2/M phase) [262]**.**

Propidium iodide (PI) is a very frequently used red-fluorescent, which has an excitation/emission maximum of 493/636 nm and intercalates into the major groove of double-stranded DNA [266,267]. Since PI is not base-pair selective for DNA, cells require additional digestion with RNAse A to remove double-stranded RNA (dsRNA) background staining. The main principle behind this dye is that PI is stoichiometric, which means that it binds in proportion to the amount of DNA present in the cell. According to this, cells in G2/M have an approximately twice as high fluorescence intensity than cells in the G1 phase, which can be measured by photomultipliers [268]. PI cannot penetrate the intact

membrane of viable cells, making it necessary to fix and permeabilize the cells prior to staining. For fixation precipitating solvents like alcohols should be used. Aldehyde reagents are not recommended since they act by creating crosslinks which can decrease the accuracy of DNA content measurement by impairing stoichiometry of DNA staining with fluorescent dyes [265].

Procedure

$2x10^5$ cells/well were seeded in 1ml into 6-well plates and incubated o/n under standard cell culture conditions. On the following day, cells were treated with the investigated drugs in different concentrations. After 24 h drug exposure, cells were trypsinized and centrifuged with 240 g for 8 minutes. After removing the supernatant cells were washed with 1x PBS, centrifuged again and the cell pellet was resuspended in 100 µl 0.9% NaCl solution. Cells were then fixed by slowly adding the cell suspension dropwise to 70 % ice-cold EtOH and stored o/n at -20 °C. After the fixation process the cells were centrifuged for 2 min at 5000 g, resuspended in 500 µl FACS-PBS/sample and treated with 2 µl RNase A/sample (0.79 Kunitz units/ml) for 30 min at 37 °C. After enzyme digestion the cells were stained with 5 µl propidium iodide/sample (1 mg/ml in PBS; Sigma-Aldrich, Missouri, USA) and incubated for 30 min at 4 °C in the dark, followed by fluorescence intensity measurement with flow cytometry (FACS Calibur – Becton Dickinson, Palo Alto, CA) and quantified with the Cell Quest Pro Software. Data illustration and statistical analysis were performed using GraphPad Prism 5.0 software (La Jolla, CA, USA).

2.4 Live Cell Imaging

Background

Live-cell imaging represents a powerful tool to study the dynamic cellular processes and interactions between living cells in real time and thereby provides an important insight into the pharmacology and the localization of the investigated drugs. Using microincubators, physiological conditions of living cells are maintained, and cells can be observed even over a period of several days. This is a big advantage over fixed-cell microscopy, where the cellular structures and activities are frozen at a certain time point and dynamic changes cannot be observed anymore [269,270]. The drawback of this method are phototoxic side effects, meaning that the excitation light needed to excite fluorophores could harm living cells and potentially alters their physiology. Furthermore photoexcited fluorophores may release reactive oxygen species (ROS), which can also induce cellular damage [271]. This must be kept in mind when setting up the experimental conditions, as improving the contrast, resolution and signal-to-noise ratio is often coupled to increased light exposure.

Consequently, live-cell imaging usually requires a compromise between good image quality and maintaining viable cells [272].

Procedure

3-5x10^4/ml cells were seeded in 8-well µ slides (Ibidi, Martinsried, Germany) in 300 µl respective growth medium and incubated o/n under standard culture conditions. On the next day cells were either additionally pretreated for 24 h with a G4 stabilizer ($TMPyP_4$ or ThT) or drugs were added directly 4-fold concentrated in 100 µl growth medium. Required environmental conditions were maintained using a microscope cage incubator (OkoLab, NA, Italy). Pictures were taken at indicated time points with a Nikon Eclipse Ti inverted microscope (Life-Cell Imaging from Visitron Systems, Puchheim, Germany) using a 40× oil immersion DIC objective, Lumencor spectra color LEDs (light-emitting diode) (395/25 nm excitation and 460/50 nm bandpass emission filter for blue, 475/34 nm excitation and 525/50 nm emission filter for green, 640/30 nm excitation and 700/75 nm emission filter for red) for fluorescence illumination and the imaging software VisiView®. Images were captured with a PCO Edge 4.2 sCMOS camera and quantified using ImageJ 1.51f software (Wayne Rasband, National Institutes of Health, USA).

2.5 Confocal Laser Scanning Microscopy

Confocal laser scanning microscopy (CLSM) is the tool of choice for increased optical resolution and contrast of a micrograph and is used throughout in the biological, biomedical and biochemical research. In contrast to conventional widefield fluorescence microscopy, where the entire specimen is evenly illuminated by the excitation light and thus generating a strong background-noise, CLSM makes use of point illumination via a spatial pinhole to eliminate out-of-focus light (Figure 44) [273]. It thereby increases the optical resolution enormously, however, also decreases in parallel the light intensity. To compensate this loss of light signal, lasers are used as light sources instead of conventional mercury and xenon arc lamps, as lasers produce very strong bundled monochromatic light of a discrete wavelength [274]. For the ZEISS LSM700 confocal microscope (Carl Zeiss microscopy, Germany) 4 different solid state laser diodes are available: violet (405 nm), blue (488 nm), yellow (555 nm) and red (639 nm) [275]. The selected laser excitation light is focused through a pinhole aperture, reflected from a dichroic mirror through the objective lens and is tightly focused onto the target surface. The longer-wavelength fluorescent light emitted from the specimen goes back through the dichroic mirror into the aforementioned confocal pinhole to eliminate all the out-of-focus light and is measured by a highly sensitive photomultiplier tube (PMT), employed for the

detection and noise-free amplification of the light signal [276]. The PMT converts photons of the light into electrical signals which can be recorded by a computer [277].

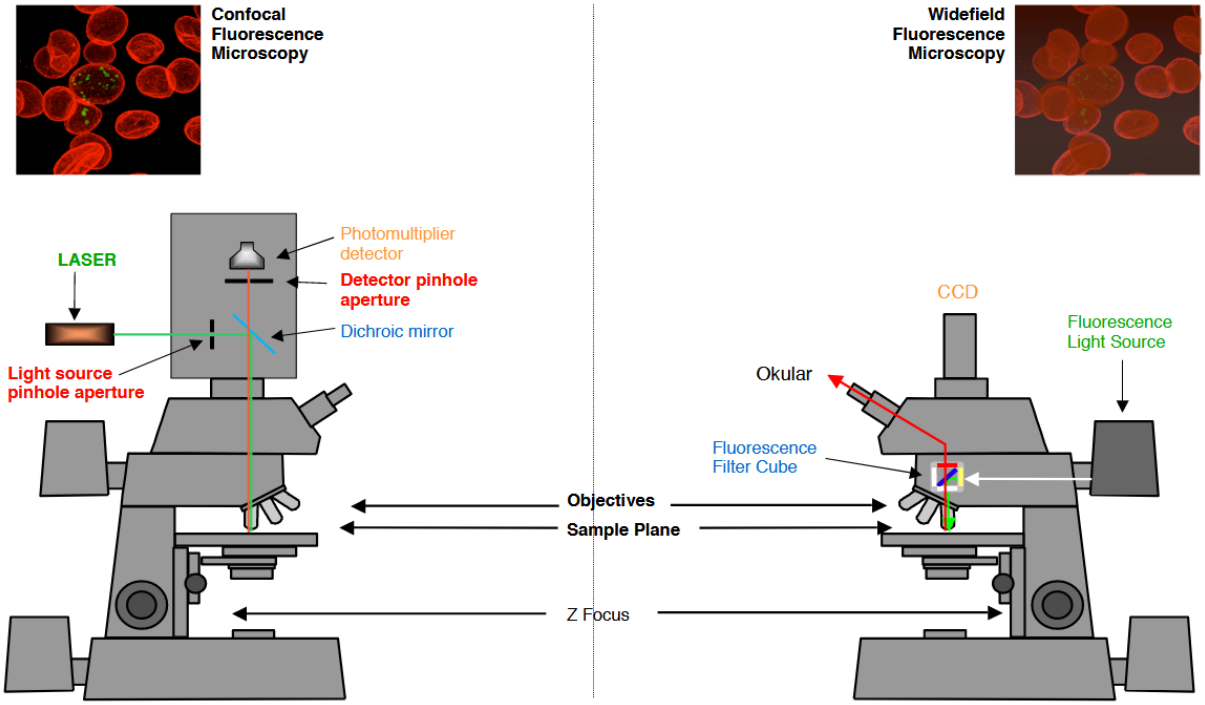

Figure 44: Overview of the differences in the set-up between a confocal and a widefield fluorescence microscope. While in conventional widefield fluorescence microscopy the entire specimen is illuminated at the same time, in confocal microcopy a pinhole is used to eliminate the out-of-focus light and thereby generates pictures with increased optical resolution [277].

Furthermore, transmitted light images can be acquired in bright field, phase contrast or differential interference contrast (DIC) simultaneously with the confocal fluorescent images. Therefore transmitted light detectors (T-PMTs) are used to collect the light passing through the sample [278]. These images are not confocal, as they do not measure light from a discrete focal plane within the specimen. For transmitted light imaging no separate lamp is used, the illumination beam originates from the same laser that is selected for the confocal fluorescent images. The combination of these micrographs allows for instance a precise location of a labeled cell or structure within an unstained sample area [279].

2.5.1 Metaphase Chromosome Preparation

Background

At the metaphase stage of mitosis chromosomes are highly condensed and thereby better visible under the microscope, which makes their analysis a fundamental tool in cytogenetic studies and cancer research. The preparation is based on adding colchicine, a spindle destabilizing reagent and alkaloid extracted from Colchicum autumnale (autumn crocus), to dividing cells (Figure 45). Colchicine binds to tubulin and inhibits microtubule polymerization, leading to an arrest of the cells at the metaphase stage [280,281].

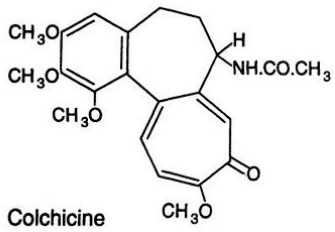

Figure 45: Chemical structure of colchicine [280]**.** The alkaloid is extracted from autumn crocus and can be used for blocking the cells in the metaphase stage of mitosis by disrupting their cell spindles.

Subsequently, cells are treated with a hypotonic solution which initiates swelling of the cells and helps to untangle the chromosomes. Cells are then fixed in a mixture of methanol and acetic acid and dropped on a glass slide, which can be further used for a variety of applications [282,283].

Procedure

U2OS cells were grown in 10ml respective growth medium in T75 cell culture flask under standard culture conditions. Cells were treated at the logarithmic phase with 100 µl colchicine (KaryoMAX COLCEMID Solution, Gibco life technologies, Waltham, MA, USA) and incubated for approximately 60min at 37 °C and 5% CO_2. After that, the medium was removed and collected, cells were washed with 1x Trypsin-EDTA (T/E) and added to the collection tube. T/E was further put on the cell-layer in the T75 flask and incubated for a few minutes until mitotic cells started to float off and adherent cells started to detach, which were also transferred to the collection tube. The cell suspension was centrifuged for 10 min at 200 g. After that the supernatant was removed (except for the last 0.5 cm) and the pellet was carefully resuspended in the remaining media. A hypotonic solution was then added very slowly and dropwise under constant shaking of the tube within 3 min, following incubation at 37 °C for 7 min. Cells were centrifuged again at 200 g for 10 min, the hypotonic solution was removed except for the last 0.5 cm like before and the pellet was resuspended in the remaining supernatant. Subsequently cells were fixed by adding again very slowly under constant shaking the

fixation solution (methanol and acetic acid 3:1), followed by an incubation at -20 °C for 30 min. Afterwards the cells were centrifuged again for 10 min at 200 g. This fixation procedure was repeated two times, but with incubation times of 60 min at -20 °C. After the last fixation step the cell pellet was resuspended in a small volume of fixation solution and dropped onto EtOH/HCl cleaned slides washed with cold ddH_2O, which were then air dried and stored at RT until subsequent fluorescence staining.

2.5.2 Cell Fixation Methods for Fluorescence Imaging

Background

Fixation of cells plays a crucial role in the sample preparation for fluorescence microscopy. The main goal is to preserve the cell morphology as close to the native state as possible. It further makes the sample more resistant for the subsequent preparation and staining procedures and prevents it from being degraded by inactivating proteolytic enzymes [284,285]. The choice of the fixation method is a critical step as it can have a huge impact on the results. This is because to date no perfect fixative is available that is able to preserve the cellular architecture while at the same time it does not modify or damage any antigenic sites, proteins, small molecules or lipids of the specimen. Generally two major groups of fixatives are used for fluorescence microscopy - aldehyde fixatives and organic solvents [284].

Aldehyde reagents are reactive electrophiles that act by creating crosslinks between free primary amine groups of proteins, thereby stabilizing and hardening the sample (Figure 46) [286].

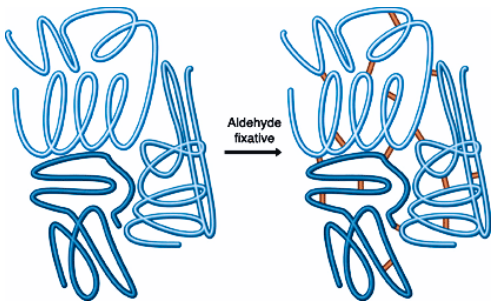

Figure 46: Aldehyde fixation. Fixation with aldehydes is based on crosslinking primary amine groups of proteins and thereby preserving the cellular structure [287].

With this fixation method the plasma membrane stays intact, making a subsequent permeabilization step necessary to allow access to intracellular targets. These fixatives are the best choice in terms of preserving the cell structure and to visualize for instance membrane bound proteins. However,

aldehyde reagents may also damage or mask antigenic sites in the specimen, which can be a serious problem for immunofluorescence labeling with certain antibodies [288,289].

Organic solvents, such as methanol or acetone, act by removing lipids and dehydrating the cells, thereby precipitating and denaturing proteins. This might be an advantage as methanol may expose thereby otherwise buried antigens. Other epitopes however can be completely destroyed during this procedure. While the cellular structure is preserved, many small, soluble molecules are lost, making MeOH fixation unsuitable for certain applications [290]. Acetone is a strong dehydrating agent that is less damaging to epitopes than methanol, which is why they are often combined 1:1 to improve cellular staining results. In contrast to aldehyde reagents no further permeabilization of the sample is required [291].

Procedure

3-7x10^4/ml U2OS and MCF-7 cells were seeded in chamber slides with a removable 8-well silicone chamber (Ibidi, Martinsried, Germany) in 300 µl respective growth medium and incubated o/n under standard culture conditions. On the next day cells were either treated when indicated with certain drugs or untreated cells were fixed immediately.

For fixation with paraformaldehyde (PFA, Sigma-Aldrich, Missouri, USA), the medium was removed and cells were washed 1-2x with prewarmed 1x PBS. A 4% PFA containing PBS solution was added and cells were incubated for 30 min at RT. After that two PFA quenching steps were performed by rinsing the cells briefly and then washing for 10 min with a 0.1 M glycin (Sigma-Aldrich, Missouri, USA) solution in 1x PBS at RT on an orbital shaker. Cells were rinsed and washed for 10 min with 1xPBS afterwards. Subsequent permeabilization was carried out with 0.1 % Triton-X-100 (Sigma-Aldrich, Missouri, USA) in 1x PBS for 15 min at RT. After washing three times with 1xPBS (rinse briefly, wash for 10min) cells were used for further (immuno-)fluorescence staining.

For fixation with methanol (MeOH) and methanol acetone 1:1 (MeAc) the medium was aspirated and cells were washed 1-2x gently with warm 1x PBS. After air-drying for at least 1 h cells were fixed with 300 µl of the respective organic solvent (pre-equilibrated at -20 °C) for 10 min at -20 °C. Following three washing steps with 1x PBS (rinse briefly, wash for 10 min), cells were ready for subsequent staining procedures.

2.5.3 Cellular Staining With Fluorophores and Pt(II) Metallacycles

Background

Fluorophores are fluorescent molecules that are characterized by their ability to absorb light at a certain wavelength and re-emit it at a higher wavelength, which is also referred to as Stokes shift (Figure 47) [292].

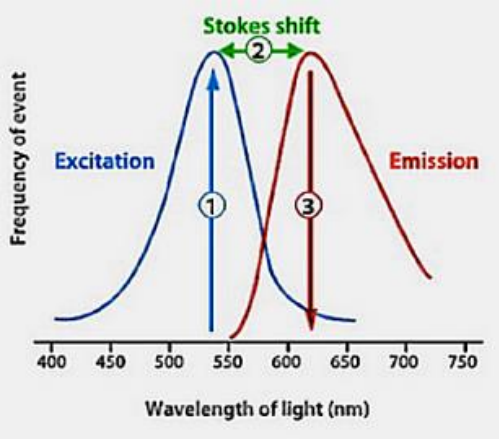

Figure 47: Stokes shift. It describes the difference between the excitation and the emission maximum of a fluorophore [293].

They can be categorized into intrinsic and extrinsic fluorophores. Intrinsic fluorophores are naturally fluorescent, like for instance the aromatic amino acids phenylalanine, tryptophan, tyrosine, flavins or chlorophyll. Extrinsic fluorophores can be added to the specimen to allow the detection of certain structures or organelles and can further be used in combination for co-staining experiments [294].

DAPI (4',6-diamidino-2-phenylindole) is a blue fluorophore that strongly binds to the minor groove of dsDNA, with preference for adenosine-thymidine (A-T) rich regions. Upon binding to DNA the blue fluorescence increases approximately 20 fold [295]. DAPI can be used to stain living and dead cells and represents a popular and easy to use counterstain for nuclei and chromosomes for fluorescence microscopy (Figure 48) [296].

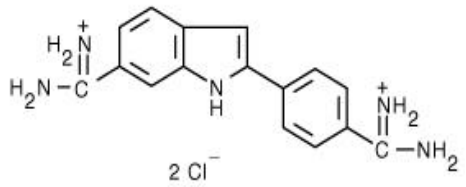

Figure 48: Chemical structure of DAPI (4',6-diamidino-2-phenylindole). DAPI is used for counterstaining nuclei and chromosomes [296].

SYTO™ RNASelect™ Green Fluorescent cell Stain (Thermo Fisher Scientific, Waltham, MA, USA) is a cell-permeant nucleic acid stain that exhibits a strong increase in fluorescence when it is bound to RNA, which makes it useful for the detection of nucleoli. After staining of live cells, MeOH-fixation must be used as PFA may alter the staining pattern [297].

Procedure

For nucleoli staining, living cells were treated with 500nM SYTO™ RNASelect™ Green Fluorescent cell Stain (Thermo Fisher Scientific, Waltham, MA, USA) following manufacture's guidelines [297] and incubated for 20 min at 37 °C and 5 % CO_2. For co-staining experiments cells were further incubated as indicated with 50 µM compound **1** for 20-60 min under the same conditions. Cells were washed twice with warm 1x PBS and fixed with MeOH or MeAc.

For counterstaining with DAPI (Thermo Fisher Scientific, Waltham, MA, USA) fixed nuclei and metaphase chromosomes were either incubated for 10 min with 1.5 µg/ml DAPI at RT or slides were mounted with Vectashield containing 1.5 µg/ml DAPI (Vector Laboratories, Inc., Burlingame, CA, USA).

Staining with Pt(II) metallacycle was performed either in living or in fixed cells. For live cell staining, cells were treated with 50 µM of the metallacycle diluted in the respective growth medium and incubated for 30-60 min at 37 °C and 5 % CO_2, following washing and fixation procedures (chapter 2.6.2). Staining of fixed cells and metaphase chromosome spreads was performed by incubating the cells with a 50 µM Pt_2L_2 dilution in 1x PBS for 30 min at RT.

After successful staining the silicon chamber of the 8 chamber slides (Ibidi, Martinsried, Germany) was removed and cells were mounted depending on the experiment with Vectashield (Vector Laboratories, Inc., Burlingame, CA, USA) with or without DAPI (1.5 µg/ml) and covered with a cover glass. Samples were stored in the dark at 4°C until subsequent analysis with a Zeiss LSM700 confocal microscope (Carl Zeiss microscopy, Germany) for fluorescence imaging in DAPI, AF594, AF488, FITC channels with a 63x objective using immersion oil. Transmitted light images were acquired with the 405 nm violet laser in DICIII with T-PMT. Micrographs were evaluated with Zeiss Zen 2010 B SP1 software (Carl Zeiss microscopy, Germany).

2.5.4 Emission Fingerprinting with Lambda Stacks

Background

Emission fingerprinting is a useful technique to assess the spectral emission signature of a fluorophore. It can be used to analyze and digitally separate multiple fluorescent labels with overlapping emission profiles, to eliminate autofluorescence signals or to determine the emission characteristics of an unknown fluorophore [298]. Therefore a series of x-y images are acquired at different emission wavelengths in an interval of 2-20 nm, creating a three-dimensional dataset called lambda stack (also referred to in the literature as image cube, spectral image stack or spectral cube) (Figure 49) [299,300]. By plotting the pixel intensity versus the emission wavelength the individual fluorescence emission spectral profile of a fluorophore can be determined [301].

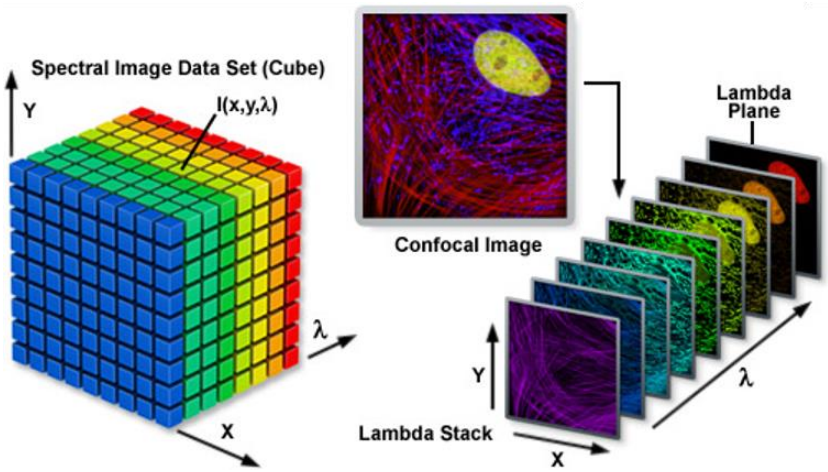

Figure 49: Spectral Imaging Lambda Stack. Emission fingerprinting is based on combining several spectral images acquired in sequential bandwidths of 2-20 nm to a lambda stack. It can be used to determine the spectral profile of uncharacterized fluorophores or to separate multiple fluorophores within a sample even with highly overlapping emission spectra [300].

Procedure

MCF-7 cells fixed with MeOH were incubated with either 50 µM compound **1** or **L1** for 30 min at RT. After three washing steps with 1x PBS (rinse briefly, wash 10 min), the silicon chamber was removed and cells were mounted with Vectashield (Vector Laboratories, Inc., Burlingame, CA, USA) without DAPI and covered with a cover glass. Lambda stacks for **1** and **L1** were acquired with a Zeiss LSM 780 confocal microscope and Zen 2.3 SP1 software (Carl Zeiss microscopy, Germany) using a 63x objective with immersion oil. The emission of the drugs was determined in the range of 411-687 nm with a bandwidth of 9 nm. Spectral images were gathered separately for each laser line: 405 nm, 458

nm, 488 nm, 514 nm, 561 nm, 594 nm and 633 nm. Data were evaluated with Zeiss Zen 2.1 software (Carl Zeiss microscopy, Germany). With the linear unmixing tool emission spectral profiles were obtained by normalizing of the signal intensity values and plotting them on a linear graph versus the corresponding emission wavelengths.

2.5.5 Immunofluorescence with G4-Specific Antibodies

Background

Immunofluorescence (IF) allows optical detection of the distribution and location of a specific protein or structure inside a cell. Therefore, fluorescent labeled antibodies are used, which either bind in a direct or indirect way to the corresponding antigens within a cell. Direct IF includes the application of a single antibody (AB) chemically linked to a fluorophore that binds to the epitope and can be visualized via fluorescence microscopy. Indirect IF is characterized by using first an unlabeled primary AB that binds to the target, followed by a fluorophore-conjugated secondary AB directed against the primary AB for the visualization (Figure 50) [302].

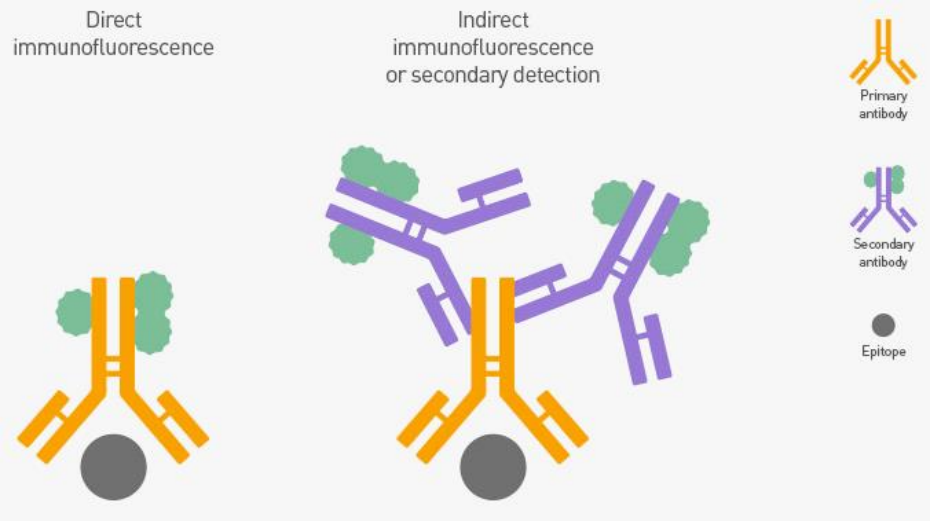

Figure 50: Comparison between direct and indirect immunofluorescence. While direct IF makes use of a single antibody linked to a fluorophore, indirect IF includes an unconjugated primary AB that is recognized by a fluorophore-conjugated secondary AB [303]**.**

Even though direct IF offers the advantage of being less time-consuming it involves higher costs and reduced flexibility. Indirect IF in contrast enables amplification of the signal and a higher sensitivity, which is why it is the more frequently used method [304]. As antibodies are very large molecules,

they cannot cross the cell membrane and are therefore unsuitable for staining living cells. Cells fixed with aldehyde reagents further have to be permeabilized to ensure access of the antibody to the antigen [305]. After fixation of the cells and prior to AB-incubation, all nonspecific binding sites have to be blocked to prevent the AB from binding nonspecifically. While improper blocking leads to a high background signal, excessive blocking can mask the epitope [306]. The blocking buffer consists of serum that contains antibodies binding to the nonspecific reactive sites and should originate from the same species where the secondary antibody was produced [307].

Procedure

Washed cells fixed with MeOH / MeAc / PFA or metaphase chromosome preparations were incubated with the blocking buffer for 45 min at RT containing 1x PBS-BSA (0.2 %) and 10 % normal goat serum (NGS). For PFA fixed and permeabilized cells 0.1 % Triton-X-100 (Sigma-Aldrich, Missouri, USA) was additionally added. After blocking the unspecific binding sites cells were incubated without a washing step in between with the primary AB diluted 1:200 in 1x PBS-BSA (0.2 %) and 3 % NGS. For fixed and permeabilized cells 0.1 % Triton-X-100 was further added to the AB solution. After o/n incubation at 4 °C, cells were washed 3 times with 1x PBS (rinse briefly, wash 10 min) and incubated with the secondary AB (AF594, Thermo Fisher Scientific, Waltham, MA, USA) diluted 1:500 in 1x PBS-BSA (0.2 %) and 3 % NGS. For PFA fixed and permeabilized cells 0.1 % Triton-X-100 was added to the AB solution and cells were incubated for 1 h at 37 °C or RT, following three washing steps in 1x PBS (rinse briefly, wash 10 min). When indicated, cells were further counterstained with 50 µM **1** for 30 min at RT and washed again with 1x PBS. The silicon chamber was removed and cells were mounted depending on the experiment with Vectashield (Vector Laboratories, Inc., Burlingame, CA, USA) with or without DAPI (1.5 µg/ml) and covered with a cover glass. Samples were stored in the dark at 4 °C until subsequent analysis with a Zeiss LSM700 confocal microscope (Carl Zeiss microscopy, Germany) for fluorescence imaging in DAPI, AF594, AF488 channels with a 63x objective using immersion oil. Transmitted light images were acquired with the 405 nm violet laser in DICIII with T-PMT. Micrographs were evaluated with Zeiss Zen 2010 B SP1 software (Carl Zeiss microscopy, Germany).

2.6 Whole Genome Gene Expression Microarray

Background

Whole genome gene expression microarrays allow the measurement of the mRNA expression level of all genes of the human genome at the same time and can be used to compare the gene expression among different conditions, like non-malignant vs. diseased or treated vs. untreated [308]. Therefore, in case of using the Agilent two-color system, total messenger RNA (mRNA) from the experimental and the reference sample are extracted and reverse transcribed into complementary DNA (cDNA) using an oligo dT-promoter primer and moloney murine leukemia virus reverse transcriptase (MMLV-RT), a RNA-dependent DNA polymerase [309]. The principle behind is based on the annealing of the oligo-dT to the poly-A tail, which is present on the 3' end of most mRNA molecules [310]. These cDNA strands are used as a template for the subsequent transcription into cRNA, while at the same time fluorescently labeled nucleotides are incorporated. After purification of the labeled cRNAs to remove excess dye, the samples are combined and heat fragmented so that the length of the cRNAs fit optimally for subsequent hybridization onto the microarray slide. The microarray consists of thousand tiny spots containing pre-designed complementary nucleotide sequences, representing all genes of the human genome. After the hybridization process and subsequent washing steps the microarray is scanned with a laser that excites the fluorescent tags of the bound cRNA to measure the relative gene expression. QC (quality control) and gene annotation is performed using Feature Extraction software, and subsequently samples are analysed separately for each color (Figure 51). With this data gene expression profiles can be created and genes whose expression is altered in response to a certain treatment or condition can be identified [311,312].

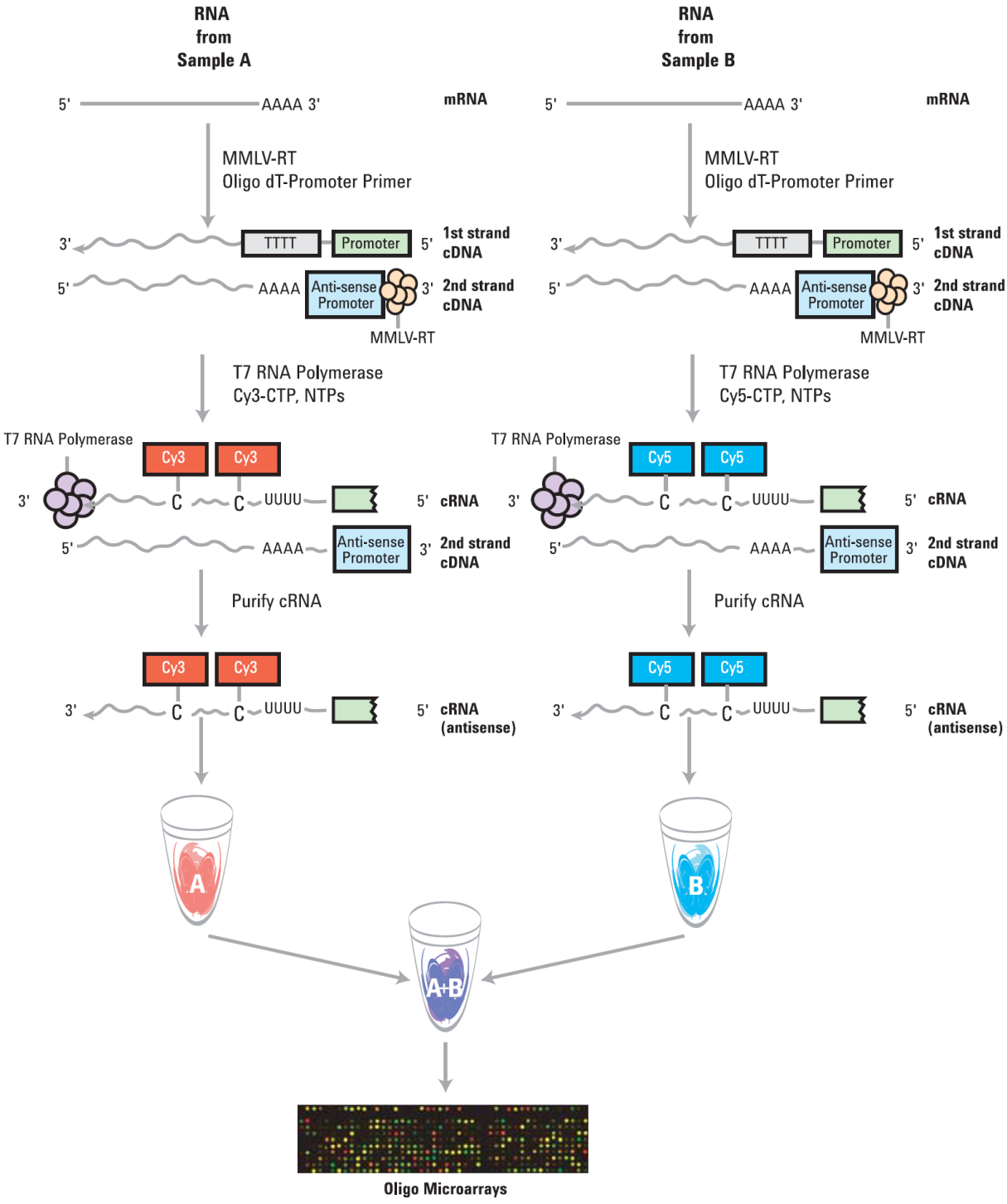

Figure 51: Schematic of the Agilent two-color microarray. mRNAs from a experimental and a reference sample are isolated and reverse transcribed into cDNA with a oligo dT-promoter primer and moloney murine leukemia virus reverse transcriptase (MMLV-RT). The cDNA strands are further transcribed into cRNA by the T7 RNA polymerase, labeled with Cy3 or Cy5 and amplified. The cRNAs of both samples are purified, combined and heat fragmented for the following hybridization on the microarray slide [313].

Procedure

U2OS cells were seeded at a density of $2x10^5$ cells per well in IMDM growth medium (Sigma-Aldrich, Missouri, USA) in 6-well plates and incubated o/n under standard culture conditions. On the following day, cells were treated in duplicates with two different concentrations of **1** (15 µM and 25 µM) and with 10 µM of the reference G-quadruplex stabilizer pyridostatin (PDS; Sigma-Aldrich, Missouri, USA). After 24 h drug exposure, cells were washed with ice cold PBS and RNA of the samples was isolated with the RNeasy Mini Kit (QIAGEN GmbH, Hilden, Germany) following manufacture's guidelines. The quality and amount of isolated RNA was measured with Nanodrop (Nanodrop 1000, Thermo Fisher Scientific, Wilmington, Germany). RNA quality and integrity were further assessed with the Agilent 2100 Bioanalyzer using the Agilent RNA 6000 Nano Kit (Agilent Technologies, Santa Clara, CA, USA). Only samples with a comparable RNA integrity number (RIN) above 9 were used for subsequent microarray analysis. The two-color gene expression microarray was performed using 4x44k whole genome oligonucleotide-based gene expression arrays (Agilent Technologies, Santa Clara, CA, USA). The Low Input Quick Amp Labelling Kit (Agilent Technologies, Santa Clara, CA, USA) was used according to the manufacturer`s instructions for reverse transcription of 75 ng of total RNA into cDNA, labeling with Cy5-CTP or Cy3-CTP, and transcription into cRNA. Amplified cRNA samples were then purified with the RNeasy Mini Kit (Qiagen GmbH, Hilden, Germany). 825 ng of each sample were combined and heat fragmented for 30 min at 60 °C. Hybridization was performed at 65 °C in a hybridization oven (Agilent Technologies, Santa Clara, CA, USA) for 17 h. Slides were washed according to the manufacture's guidelines and scanned with a G2505B Micro Array Scanner (Agilent Technologies, Santa Clara, CA, USA). QC control and gene annotation was carried out using Feature Extraction software, and subsequently samples were analysed separately for each color using GeneSpring software (Agilent Technologies, Santa Clara, CA, USA). An overview of the workflow for the sample preparation and array processing is shown in Figure 52.

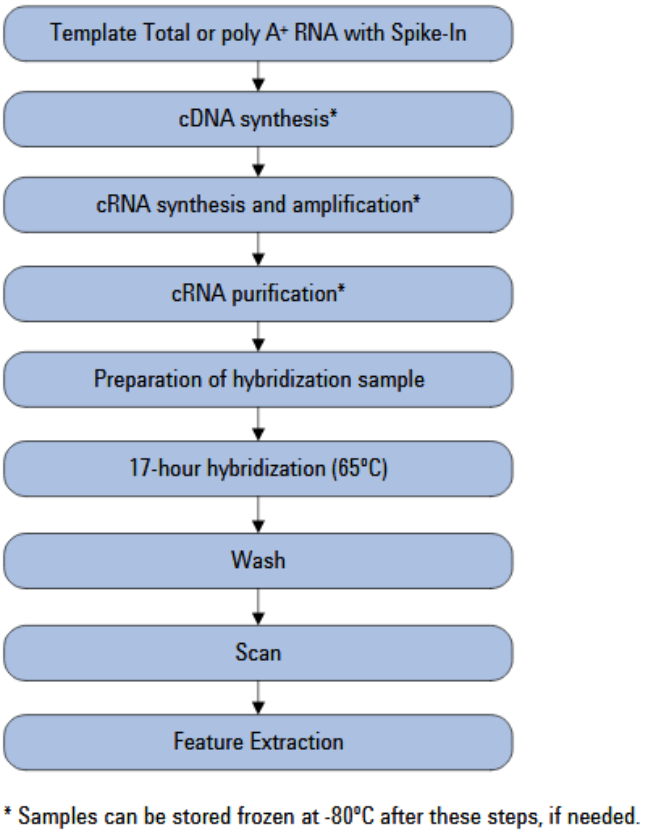

Figure 52: Workflow of the Agilent two-color microarray [313].

3 Results and Discussion

3.1 Prologue of the Equally Contributed First Authorship Publication

"Subcellular Duplex DNA and G-Quadruplex Interaction Profiling of a Hexagonal PtII Metallacycle."

Angewandte Chemie International Edition. 2019 Jun 11;58(24):8007-8012. PMID: 31002438

Impact factor: 12.257

G-quadruplexes attracted much attention during the last years as novel anticancer targets due to their involvement in several pivotal biological processes, such as telomere maintenance, DNA replication, transcription and gene expression. Thus, the rational design of small molecule ligands targeting these noncanonical nucleic acids is considered a promising approach for anticancer therapy. Amongst them, metal-based complexes have emerged as particularly strong and selective G4 binders. Based on a recent report of a self-assembly strategy of Pt_2L_2 boxes aimed at targeting G-quadruplex structures [255], the goal of this study was to synthesize a new, improved version of former self-assembled Pt_2L_2 boxes in terms of efficacy and G4 selectivity as well as to study its applicability in cancer cells. As the Pt_2L_2 metallacycle was designed to be intrinsically fluorescent, we were able to proof that our compound enters cancer cells, is sequestered to cancer cell nuclei, particularly targeting nucleolar substructures, and displays a strong blue fluorescence resistant to UV photobleaching. We further showed that our Pt_2 complex co-localizes with BG4, a G4-specific antibody, and displaces other well-established G4 stabilizers. Moreover, we report on photophysical changes (fluorescence quenching and increased absorption) occurring specifically upon G4 binding.

In this study, I performed the great majority of the biological experiments and in-cell tracking by myself, while Dr. Olaya Domarco from the Universidade da Coruña in Spain and Dr. Alessio Terenzi from the University of Inorganic Chemistry in Vienna (Present address: Donostia International Physics Center, Paseo Manuel de Lardizabal 4, 20018, Donostia, Spain) were responsible for the synthesis of the Pt_2L_2 metallacycle and investigation of its chemical properties. Airyscan super-resolution images were taken at the University of Veterinary Medicine in Vienna and emission fingerprinting was performed at the Core Facility at the Medical University in Vienna both in collaboration with Dipl.-Ing. (FH) Johannes Reisecker.

GDCh Communications Angewandte International Edition Chemie

Subcellular Localization

International Edition: DOI: 10.1002/anie.201900934
German Edition: DOI: 10.1002/ange.201900934

Subcellular Duplex DNA and G-Quadruplex Interaction Profiling of a Hexagonal Pt^{II} Metallacycle

Olaya Domarco[+], Claudia Kieler[+], Christine Pirker, Carina Dinhof, Bernhard Englinger, Johannes M. Reisecker, Gerald Timelthaler, Marcos D. García, Carlos Peinador, Bernhard K. Keppler, Walter Berger,* and Alessio Terenzi**

Abstract: *Metal-driven self-assembly afforded a multitude of fascinating supramolecular coordination complexes (SCCs) with applications as catalysts, host–guest, and stimuli-responsive systems. However, the interest in the biological applications of SCCs is only starting to emerge and thorough characterization of their behavior in biological milieus is still lacking. Herein, we report on the synthesis and detailed in-cell tracking of a Pt_2L_2 metallacycle. We show that our hexagonal supramolecule accumulates in cancer cell nuclei, exerting a distinctive blue fluorescence staining of chromatin resistant to UV photobleaching selectively in nucleolar G4-rich regions. SCC co-localizes with epitopes of the quadruplex-specific antibody BG4 and replaces other well-known G4 stabilizers. Moreover, the photophysical changes accompanying the metallacycle binding to G4s in solution (fluorescence quenching, absorption enhancement) also take place intracellularly, allowing its subcellular interaction tracking.*

The thoughtful choice of transition metals and multidentate ligands allows for the generation of a number of self-assembled supramolecular coordination complexes (SCCs) with intriguing geometries and attractive properties, including optical, sensing, and catalytic.[1–3] Despite the extraordinary growth of the chemistry of SCCs, studies reporting on their potential biomedical applications are so far extremely limited. Recently, some research groups have started to exploit the cavity-cored nature of 3D metallacages to develop innovative drug delivery systems.[2,4–6] We and others focused our efforts on the intrinsic anticancer potential of SCCs,[5] devoting particular attention to those supramolecules where platinum drives the self-assembly.[7–10] Pt-ensembles can in principle be designed to mimic complex cellular regulatory motifs. Therefore, they can act through unusual modes of action potentially capable to overcome the drawbacks (for example resistance) of clinically applied Pt^{II} drugs.[11] Nevertheless, apart from preliminary reports on their cytotoxic activity, detailed information about the in-cell fate of Pt-SCCs is still missing.

In this regard, Stang and Olenyuk reported on the intracellular localization of two emissive Pt^{II} metallacycles.[12] Their compounds were proposed to accumulate in lysosomes of cancer cells producing low toxicity, yet effectively inducing tumor shrinkage in mouse xenograft models.[12] Stang and his team also developed theranostic nanoconstructs incorporating platinum metallacages that displayed in vivo anticancer activity.[13,14] A further demonstration of the potential of Pt^{II}-SCCs in biomedicine was provided by Sleiman and Mao, who discovered that Pt^{II}-based metallacycles display fairly good ability to bind DNA G-quadruplexes (G4s) in solution.[15–18] G4s are non-canonical DNA/RNA motifs enriched in important regulatory regions,[19] and regarded as emerging targets for anticancer drugs.[20] They recently achieved a "star" status due to their subcellular visualization using G4-specific antibodies.[21,22] Furthermore, two G4 binders (CX-3543 and CX-5461) have entered advanced clinical trials for human cancers.[23,24]

In this context, we have recently reported on the promising DNA binding profiles of 4,4′-bipyridine-based dinuclear Pt^{II} metallacyles.[25] Our SCCs, whilst not particularly cytotoxic ($IC_{50} \geq 40\ \mu M$), distinctly influence the expression of genes known to contain quadruplex motifs in their promoters, with potency and selectivity which well correlate with the size of the supramolecules.[25] Herein, we report on a new hexagonal dinuclear Pt^{II} metallacycle (**1**, Figure 1) designed to have DNA-binding capacity and favorable optical properties for tracking its in-cell fate when bound to different nucleic acid structures.

Over the past few years we have developed a straightforward strategy for the self-assembly of dinuclear Pt^{II}-based metallacycles.[26] Inspired by recent works of Wasielewski and Stoddart on cyclophanes bearing isolated phenyl-extended

[*] O. Domarco,[+] Prof. M. D. García, Prof. C. Peinador
Universidade da Coruña, Departamento de Química y Centro de Investigacións Científicas Avanzadas
E-15071 A Coruña (Spain)
E-mail: carlos.peinador@udc.es

C. Kieler,[+] C. Pirker, C. Dinhof, Dr. B. Englinger, J. M. Reisecker, G. Timelthaler, Prof. W. Berger
Medical University of Vienna, Department of Medicine I, Institute of Cancer Research and Comprehensive Cancer Center
Borschkegasse 8a, A-1090 Vienna (Austria)
E-mail: walter.berger@meduniwien.ac.at

Prof. B. K. Keppler, Dr. A. Terenzi
University of Vienna, Institute of Inorganic Chemistry
Waehringerstrasse 42, A-1090 Vienna (Austria)
E-mail: aterenzi@dipc.org

Dr. A. Terenzi
Present address: Donostia International Physics Center
Paseo Manuel de Lardizabal 4, 20018 Donostia (Spain)

[+] These authors contributed equally to this work.

Supporting information and the ORCID identification number(s) for the author(s) of this article can be found under: https://doi.org/10.1002/anie.201900934.

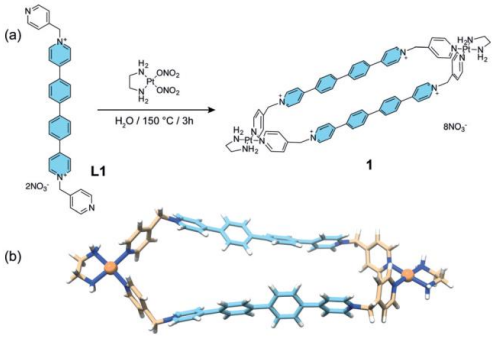

Figure 1. a) Synthesis of Pt-SCC **1**. b) DFT optimized structure of **1**.

viologen moieties,[27,28] we argued that the ditopic pyridyl ligand **L1** (Figure 1a) would confer an adequate emission profile to the final supramolecule and overcome quenching effects typical of SCCs.[29–31] The highly emissive biphenyl-extended viologen moiety (Figure 1, in turquoise) would maintain a ligand-centered emission profile when incorporated in the corresponding dinuclear Pt^{II}-metallacycle **1** due to the non-direct connectivity to the metal centers. Furthermore, the dimensions (ca. 200 $Å^2$) and the octacationic nature of **1** are quite similar to those of our previously reported DNA/quadruplex binders,[25] a fact that we envisaged would translate as well into a comparable DNA-binding profile. Synthesis of **1** was carried out according to methodologies previously reported by us for similar SCCs (see Supporting Information for details).[32]

Steady-state 3D excitation-emission spectra (Supporting Information, Figure S1a,b) showed that **1** buffered solutions emit in the blue with a maximum at 445 nm when excited at 360 nm (an absorption band ascribed to π–π* transitions of the biphenyl moiety). The fluorescence profile of **1** is rather similar to the one of its ligand **L1,** whose emission maximum is slightly blue-shifted ($\lambda_{max} = 437$ nm, Figure S1b in the Supporting Information). This, together with the observation that both **1** and **L1** have emission lifetimes of about 2–3 ns (Supporting Information, Figure S1c), suggest that fluorescence is mainly dependent on the excited states of the ligand, as reported likewise for other Pt^{II}-SCCs.[12] Even though ligand **L1** is more emissive in water than **1** ($\varphi_F = 0.84$ at 437 nm, Figure S2 in the Supporting Information), the metallacycle has a surprisingly good quantum yield in water ($\varphi_F =$ 0.38 at 445 nm). This finding is in sharp contrast to what has been recently observed for other platinum-based cages which display high emission only in non-polar solvents.[33] Such an aspect is particularly important for SCCs biological applications, making **1** a good candidate for tracking the cellular distribution of this class of compounds.

After proving by NMR and UV/Vis spectroscopy that **1** is stable overtime in water, buffered solutions, and cell culture media (with or without fetal bovine serum) (Supporting Information, Figure S3), we explored the interaction of the metallacycle with different DNA sequences including duplex DNA and G4 models. FRET, UV/Vis, fluorescence, and circular dichroism assays showed that **1** is able to strongly bind both duplex and quadruplex DNAs, with moderate preference for parallel G4s (see Supporting Information and Figure S4–S7 for a detailed discussion), similarly with what was observed for other Pt-SCCs prepared by us previously.[25]

We then investigated the applicability of our newly synthesized Pt-compound in biological settings, evaluating its impact on the viability of non-transformed human keratinocytes and human lung fibroblasts (HaCaT and HLF) as well as of cancer cell models derived from different primary origins including breast cancer, osteosarcoma, melanoma, and glioblastoma (Figure 2a and Table S1 in the Supporting Information). While HaCat cells were completely resistant against the cytotoxic impact of the metallacycle, the activity against highly proliferative HLF was comparable to malignant cell types, where **1** showed IC_{50} values in the range 30–45 μM after 72 h of incubation, with MCF-7 and U2OS being the most sensitive models. Ligand **L1** was slightly less active and followed the same trend (Supporting Information, Figure S8a and Table S1). These results are in good agreement with the general low cytotoxicity of similar Pt-SCCs observed earlier by ourselves and Olenyuk.[12,25] Combination of **1** with cisplatin in MCF-7 cells (Supporting Information, Figure S8b) gave rise to a slightly antagonistic effect suggesting that they may share mutual targets (nucleic acids) but exert a differing mode of action.

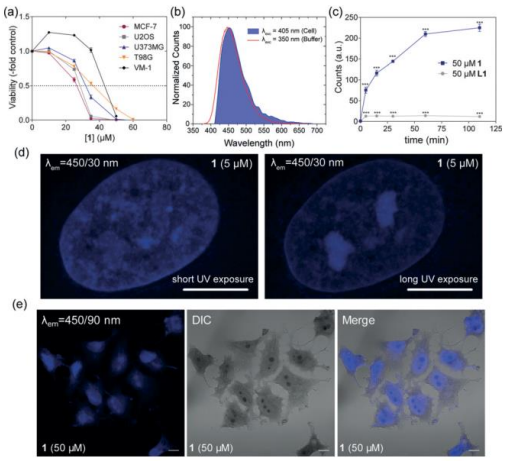

Figure 2. a) Cell viability assessed by MTT assay following exposure to **1** (0–50 μM). b) Normalized emission signatures of **1** in MCF-7 cells acquired with confocal microscope (blue filled area) and in cell-free buffer acquired with a spectrofluorometer. c) Flow cytometric analysis of U2OS cells treated with 50 μM of **L1** (grey) and **1** (blue) over time ($\lambda_{exc} = 405$ nm, $\lambda_{em} = 450/50$ nm), $p < 0.001$, 1-way ANOVA, Bonferroni post-test. d) Airyscan super-resolution microscopy images of U2OS cells treated with 5 μM **1** at short- (10 ms) and long-term (100 ms) exposure ($\lambda_{exc} = 405$ nm, $\lambda_{em} = 450/30$ nm) indicating selective photobleaching effects of **1**. e) CLSM and DIC microscopy images acquired for PFA-fixed MCF-7 cells incubated for 30 min with **1** at 50 μM ($\lambda_{exc} = 405$ nm). Scale bars = 10 μm.

MCF-7 and U2OS cell sensitivity to **1** was also tested through clonogenic assay, selecting a longer incubation time (7 days). Both cell lines showed impaired colony formation upon incubation with **1** at already 15–20 μM (Supporting Information, Figure S9). Interestingly, the long-term treatment had a stronger impact on U2OS compared to MCF-7 cells (15 μM vs. 20 μM, respectively). Conversely, cell cycle distribution analysis revealed that after 24 h incubation there was a significant dose-dependent cell accumulation in G0/G1 phase and clear-cut cell death induction only in MCF-7 cells, while U2OS cell populations presented no appreciable changes at this comparably short incubation time (Supporting Information, Figure S10).

To elucidate whether **1** indeed targets G4 regulated genes, whole genome gene expression analyses were performed on U2OS cells comparing the impact of the metallacycle with that of pyridostatin (PDS), a well-known G4 stabilizer.[21] Gene set enrichment analysis (GSEA) clearly revealed that **1** preferentially targets genes located in chromosomal regions enriched in G4 structures[34] with multiple KEGG terms similarly suppressed or activated by **1** and PDS (Supporting Information, Figure S11 a–c).

Confocal laser scanning microscopy (CLSM) was used to evaluate **1** subcellular emission fingerprint. MCF-7 cells treated with **1** revealed an intense blue fluorescence signal in the range 420–518 nm ($\lambda_{exc} = 405$ nm, Figure 2b and S12 in the Supporting Information), showing a nearly perfect overlap with the emission band obtained in cell-free conditions (Figure 2b). Flow cytometry analysis of **1**-treated U2OS cells nicely confirmed CLSM results. Pt-SCC **1** gave rise to a considerable emission in the blue portion of the spectrum ($\lambda_{exc} = 405$ nm) (Supporting Information, Figure S13a). Interestingly, **1**-associated emission decreased when cells were treated concomitantly with PDS suggesting G4s involvement.[21] In contrast it was unaffected by combination with cisplatin indicating a different binding mechanism (Supporting Information, Figure S13b). In CLSM analyses as well as in FACS experiments, **L1** emission was considerably lower. FACS, for example, displayed a drastic reduction of the blue fluorescence of 94% for **L1** at $\lambda_{exc} = 405$ nm (Supporting Information, Figure S13). The efficiency of **1** emission in cell can be attributed to the increased rigidity imposed by the metallacycle to the biphenyl-extended fluorophore.[28] FACS analysis of U2OS cells treated with **1** showed a significant drug accumulation within the first hour of incubation, while **L1** did not share the same accumulation features (Figure 2c). Live cell imaging indicated that exposure of U2OS cells to compound **1** at 35 μM produced an increase in fluorescence overtime (Supporting Information, Figure S14) which nicely corroborates FACS results. The emission of the ligand was in this case below the detection limit of the instrument (Supporting Information, Figure S15). Crucially, the different emissive behavior of **L1** compared to **1**, observed using diverse experiments and techniques, suggests a different trafficking dynamic inside the cells for the two compounds and allows ruling out possible cellular decomposition of the platinum ensemble to its free building blocks.

Drug distribution within cells was further studied by CLSM. Super-resolution airy-scan images of U2OS cells fixed with MeOH and incubated with **1** showed a structured blue staining of the whole nucleus confirming binding of **1** to DNA. Extended UV exposure, however, produced a photobleaching effect which was dependent on the sub-nuclear region. Hence, at G4-rich loci, **1** photobleaching was distinctly less efficient resulting in the labelling of nucleoli-like substructures (Figure 2d). This effect was corroborated by time-lapse fluorescence microscopy (Supporting Information, Figure S16). Confocal micrographs of U2OS and MCF-7 cells fixed with paraformaldehyde (PFA) confirmed the pan-nuclear blue fluorescent staining induced by **1** (Figure 2e and S17a in the Supporting Information). Interestingly, images of fixed cells exposed to **1,** acquired using DIC (differential interference contrast) mode, revealed a strong contrast enhancement of nuclei and a clear-cut "dark" staining of the nucleoli-like substructures (see below). This unique effect is independent of the fixation method since MCF-7 cells fixed with methanol gave the same outcome (Supporting Information, Figure S17b). Such a contrast enrichment effect was not detected when cells were incubated with **L1** or DAPI, a conventional nuclear DNA stain (Supporting Information Figure S17a).

To have a first hint about possible interaction of **1** with G4s in cells, fluorescence competition assays were performed and analyzed by live cell imaging microscopy. The G4-binders TMPyP4 and Thioflavin-T (ThT) were used since they are also intracellularly fluorescent. In detail, TMPyP4 is a non-selective porphyrin-based binder displaying a red emission,[35] while ThT is known for its green fluorescent, G4-selective, light-up effect both in solution[36] and in cells.[37] MCF-7 cells incubated with the porphyrin and **1** showed an initial TMPyP4-associated red fluorescence localized in the nuclei that turned blue overtime (Supporting Information, Figure S18a and Video S1). The same effect was obtained with ThT/**1** incubation, with the ThT-associated nucleolar green emission being replaced by the blue signals induced by **1** (Supporting Information, Figure S18b and Video S2). This outcome clearly indicated that **1** acts as competitor of both TMPyP4 and ThT for the same binding sites (duplex and G4s), showing an enhanced long-term target affinity. It is worth noting that live cell imaging was affected by considerable cell death after treatment with **1**, probably based on phototoxicity or synergistic effects when combined with TMPyP4 and ThT. We verified the latter hypothesis through viability assays, demonstrating that co-incubations of **1** with ThT (or PDS) produced strong synergistic cytotoxicity in MCF-7 and U2OS cells (Supporting Information, Figure S18c).

A competition assay was also performed in cells fixed after ThT exposure. Metallacycle **1** blocked the G4-selective green fluorescence staining of nucleoli by ThT (Figure 3a and S19a in the Supporting Information), comparable to recent reports for PDS.[37] Similarly, **1** completely displaced the green nucleoli marker SYTO®RNASelect (SYTO, Figure 3b), while it did not interact with mitochondrial labelling by MitoTracker Red (MR, Figure S19b in the Supporting Information).

To further evaluate that cellular distribution of **1** could be governed also by the presence of G4s besides duplex DNA, a series of immunofluorescence studies using the quadruplex

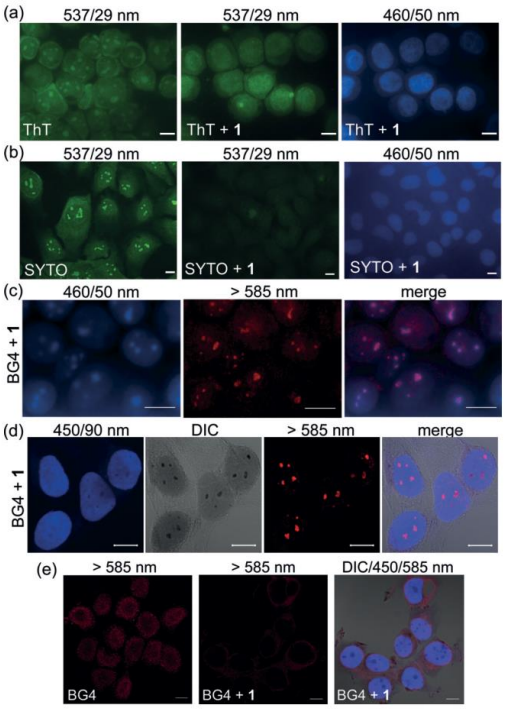

Figure 3. a) Fluorescence microscopy images of MeOH fixed MCF-7 cells, stained with ThT (5 μM) with and without **1** (5 μM) as indicated. Metallacycle **1** prevented ThT G4-specfic nucleolar signals. b) Fluorescence microscopy images of U2OS cells stained with SYTO (500 nM), then fixed with MeOH and exposed to **1** (5 μM). c) Fluorescence microscopy images of MeOH-fixed MCF-7 cells co-stained with BG4 and **1** (order: BG4, **1**) after photobleaching. d,e) CLSM images of MeOH-fixed MCF-7 cells co-stained with BG4 and **1** (order: BG4, **1**) e) PFA-fixed MCF-7 cells co-stained with **1** and BG4 (order: **1**, BG4). Scale bars = 10 μm.

specific antibody BG4[21,22] was performed (Figure 3c–e). Fluorescence microscopy images of MeOH-fixed MCF-7 cells were acquired after BG4 immunofluorescence and subsequent **1** staining at extended UV exposure(photobleaching). Figure 3c depicts the clear and distinct cellular co-localization of BG4-associated red G4-rich foci with photobleaching-resistant **1** fluorescence, both enriched in nucleolar regions.

We then repeated BG4 co-localization experiments, taking advantage of the clear-cut "dark" staining of subnuclear structure observed previously for compound **1.** CLSM images of MeOH fixed MCF-7 cells (Figure 3d) proves that, also in this case, **1** co-localized with the anti-G4 immunostaining by BG4. In detail, our Pt-SCC labelled the whole nucleus with a blue fluorescence and rendered nuclear substructures visible in the DIC channel as dark stains. BG4 revealed red signals exactly in the same regions (λ_{exc} = 555 nm) as depicted from representative pixel intensity plots of fluorescence and DIC images (Supporting Information, Figure S20). It should be noted that BG4 epitope distribution is known to be dependent on the fixation method used. Recent studies reported that the antibody labels preferentially nucleoli when MeOH is used for fixation.[38] Hence, our experiments indicate that Pt-metallacycle **1** actually targets G4-rich nucleolar structures. The co-labelling assays were repeated both changing either the incubation order or the fixation method. When MCF-7 cells were fixed with MeOH, incubated with **1** and then with the antibody, a loss of BG4 staining in the nucleoli was produced (Supporting Information, Figure S21a). The micrographs showed instead a weak overall red labelling within the cytoplasm. The outcome was similar when living cells were pre-treated with **1**, then fixed and finally labelled with BG4 (Supporting Information, Figure S21b). Additionally, comparable displacement effects were obtained when MCF-7 cells were fixed with PFA. Incubation with BG4 produced the classic nuclear red punctate staining pattern (Figure 3e and Figure S22 in the Supporting Information) as reported by Biffi et al.[21,22] When PFA-fixed cells were pre-treated with **1**, the BG4 punctate pattern got diffused, appearing enriched in the cytoplasm, demonstrating that metallacycle **1** disrupted BG4 ability to stain G4s in the nuclear region. Eventually, co-incubation of **1** and BG4 rendered comparable results at the level of individual chromosomes, obtaining the same effect (Supporting Information, Figure S23d).

Overall, these experiments clearly indicate that **1**, once inside the nucleus (and the nucleoli), interacts with nucleic acids and interferes with the G4 epitope recognition by BG4.

Besides its cellular co-localization with BG4 and its emissive properties, our Pt-metallacycle showed the unique ability to provide well-contrasted images of cells in transmission (monochrome) DIC mode. The brightfield channel is often ignored in drug accumulation studies for several reasons (poor contrast, difficult localization of cell borders, faint nuclei and others).[39] Nevertheless, we were particularly intrigued by the clear-cut and intense dark staining of nucleoli provided by **1**, which resulted to be easily reproducible and independent of the fixation method and cell line used.

Considering the complex optical mechanism at the basis of DIC microscopy,[40] we hypothesized that the dark nucleolar "staining" could arise from absorption or refraction (or both) of the light by the Pt-metallacycle within the subnuclear structures, associated to a simultaneous quenching (and photobleaching resistance) of its blue fluorescence. The UV/Vis spectrum of **1** in solution showed a band centred at 355 nm with a tail ending at around 430 nm (Figure 4a). Interestingly, the absorbance at 355 nm was significantly red-shifted when aliquots of pre-folded parallel quadruplex were added, resulting in a considerable increase in absorption at 405 nm (Figure 4a). This effect was noticeably less pronounced when the same experiment was performed using a double-stranded DNA model (Supporting Information, Figure S5b). At the same time, a strong fluorescence quenching was observed after interaction of **1** with the same parallel G4 in solution (Figure 4b). Crucially, the quenching was less pronounced after the interaction with ds-DNA, as confirmed by the binding and the Stern–Volmer constants lower in two

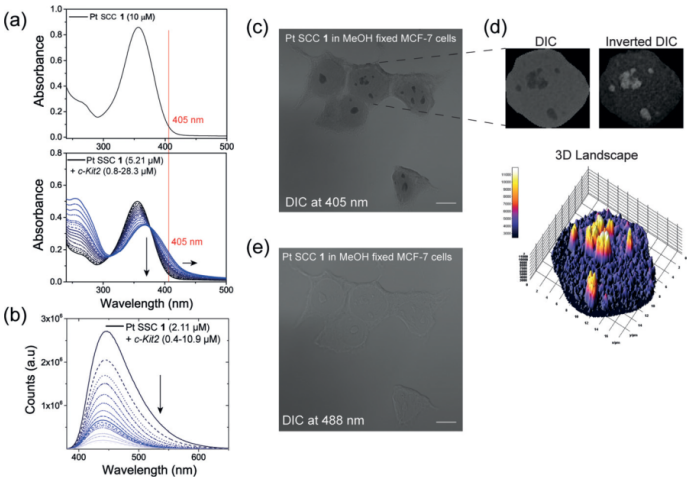

Figure 4. a) UV/Vis absorption spectrum of **1** alone (up) and in combination with increasing amount of *c-Kit2* G4 solution (down). b) Fluorescence titration of **1** with *c-Kit2* G4. c) Image of MCF-7 cells fixed with MeOH and incubated with **1** acquired using DIC mode at 405 nm. d) Differences in absorption within subnuclear regions of a representative **1**-treated nucleus derived from c) visualized by three-dimensional surface plotting of single pixel intensities of the inverted DIC image. e) Image of MCF-7 cells fixed with MeOH and incubated with **1** acquired using DIC mode at 488 nm. Scale bars = 10 μm.

and one orders of magnitudes, respectively (Supporting Information, Figure S6).

Furthermore, MCF-7 cells fixed with MeOH and incubated with **1** afforded cell images with dramatically enhanced contrast in the DIC setting with 405 nm excitation (where the metallacycle-G4 adduct preferentially absorbs light, Figure 4a), depicting prominently visible nucleoli (Figure 4c,d). When changing the excitation wavelength to 488 nm, just faint cell contours typical for DIC remained visible (Figure 4e). Of note, nucleoli staining was not observed when fixed MCF-7 cells were incubated with another Pt-SCC, selected among our toolbox of metallacycles because of its transparency at 405 nm (Supporting Information, Figure S24). Likewise, staining of fixed MCF-7 cells with DAPI resulted in the expected blue chromatin staining without any contrast enhancement in the DIC setting. While nucleoli remained invisible in absorption imaging, they appeared darker in the blue fluorescence channel based on the well-known binding of DAPI to AT-rich regions (Supporting Information, Figure S25).

These considerations strongly suggest that the dark staining is produced by absorption of **1** interacting with G4 structures within the nucleoli in association with initial distinct fluorescence quenching.

In summary, we thoroughly described the intracellular fate of a Pt-SCC. Based on its fluorescence properties, we show, for the first time for a Pt-based SCC, that **1** is taken up by cancer cells and accumulates in the nucleus. Furthermore, the particular alterations of the metallacycle optical features when interacting with G4 as compared to duplex DNA offered a unique tool for its subcellular interaction profiling. Compound **1** preferentially targets nucleolar structures, co-localizes with a G4-specific antibody and displaces well-known G4 stabilizers. Our in-solution and cellular results, together with the information that nucleoli are particularly rich in G4 forming sequences,[38,41–43] strongly support that these noncanonical nucleic acid structures are also the final target of the Pt-SCC. Quarfloxin (CX-3543), the first-in-class G4-binder in clinical trials, is believed to exert its anticancer activity through a similar mechanism, that is, precisely by accumulation in nucleoli.[23] To conclude, platinum-based SCCs are an extremely versatile class of compounds with the potential to mimic recognition properties of complex biological systems. This manuscript provides evidence that nucleic acids, and in particular G-quadruplex structures, can be key cellular targets of platinum-driven supramolecular coordination compounds. Our findings open new avenues in the development of anticancer platinum-based SCCs with promising and defined mechanisms of action.

Acknowledgements

A.T. has received funding from the Mahlke–Obermann Stiftung and the European Union's Seventh Framework Programme (grant agreement no. 609431). C.D. is a recipient of a DOC Fellowship of the Austrian Academy of Sciences (24660). C.P. is grateful to the Ministerio de Economía, Industria *y* Competitividad and FEDER (CTQ2016-75629-P). A.T. is grateful to Prof. L. Salassa for his support and advice.

Conflict of interest

The authors declare no conflict of interest.

Keywords: G-quadruplex · metallacycle · platinum · SCC · subcellular localization

How to cite: *Angew. Chem. Int. Ed.* **2019**, *58*, 8007–8012
Angew. Chem. **2019**, *131*, 8091–8096

[1] R. Chakrabarty, P. S. Mukherjee, P. J. Stang, *Chem. Rev.* **2011**, *111*, 6810–6918.
[2] T. R. Cook, P. J. Stang, *Chem. Rev.* **2015**, *115*, 7001–7045.
[3] A. J. McConnell, C. S. Wood, P. P. Neelakandan, J. R. Nitschke, *Chem. Rev.* **2015**, *115*, 7729–7793.

[4] A. Casini, B. Woods, M. Wenzel, *Inorg. Chem.* **2017**, *56*, 14715 – 14729.
[5] T. R. Cook, V. Vajpayee, M. H. Lee, P. J. Stang, K. W. Chi, *Acc. Chem. Res.* **2013**, *46*, 2464 – 2474.
[6] B. Therrien, G. Süss-Fink, P. Govindaswamy, A. K. Renfrew, P. J. Dyson, *Angew. Chem. Int. Ed.* **2008**, *47*, 3773 – 3776; *Angew. Chem.* **2008**, *120*, 3833 – 3836.
[7] A. Ahmedova, D. Momekova, M. Yamashina, P. Shestakova, G. Momekov, M. Akita, M. Yoshizawa, *Chem. Asian J.* **2016**, *11*, 474 – 477.
[8] F. Kaiser, A. Schmidt, W. Heydenreuter, P. J. Altmann, A. Casini, S. A. Sieber, F. E. Kühn, *Eur. J. Inorg. Chem.* **2016**, 5181 – 5181.
[9] A. Terenzi, C. Ducani, V. Blanco, L. Zerzankova, A. F. Westendorf, C. Peinador, J. M. Quintela, P. J. Bednarski, G. Barone, M. J. Hannon, *Chem. Eur. J.* **2012**, *18*, 10983 – 10990.
[10] M. Mounir, J. Lorenzo, M. Ferrer, M. J. Prieto, O. Rossell, F. X. Avilès, V. Moreno, *J. Inorg. Biochem.* **2007**, *101*, 660 – 666.
[11] B. Englinger, C. Pirker, P. Heffeter, A. Terenzi, C. R. Kowol, B. K. Keppler, W. Berger, *Chem. Rev.* **2019**, *119*, 1519 – 1624.
[12] I. V. Grishagin, J. B. Pollock, S. Kushal, T. R. Cook, P. J. Stang, B. Z. Olenyuk, *Proc. Natl. Acad. Sci. USA* **2014**, *111*, 18448 – 18453.
[13] G. Yu, T. R. Cook, Y. Li, X. Yan, D. Wu, L. Shao, J. Shen, G. Tang, F. Huang, X. Chen, et al., *Proc. Natl. Acad. Sci.* **2016**, *113*, 13720 – 13725.
[14] G. Yu, M. Zhang, M. L. Saha, Z. Mao, J. Chen, Y. Yao, Z. Zhou, Y. Liu, C. Gao, F. Huang, et al., *J. Am. Chem. Soc.* **2017**, *139*, 15940 – 15949.
[15] R. Kieltyka, P. Englebienne, J. Fakhoury, C. Autexier, N. Moitessier, H. F. Sleiman, *J. Am. Chem. Soc.* **2008**, *130*, 10040 – 10041.
[16] X.-H. Zheng, H.-Y. Chen, M.-L. Tong, L.-N. Ji, Z.-W. Mao, *Chem. Commun.* **2012**, *48*, 7607 – 7609.
[17] X.-H. Zheng, Y.-F. Zhong, C.-P. Tan, L.-N. Ji, Z.-W. Mao, *Dalton Trans.* **2012**, *41*, 11807 – 11812.
[18] A. Garci, K. J. Castor, J. Fakhoury, J. L. Do, J. Di Trani, P. Chidchob, R. S. Stein, A. K. Mittermaier, T. Friščić, H. Sleiman, *J. Am. Chem. Soc.* **2017**, *139*, 16913 – 16922.
[19] R. Hänsel-Hertsch, M. Di Antonio, S. Balasubramanian, *Nat. Rev. Mol. Cell Biol.* **2017**, *18*, 279 – 284.
[20] S. Neidle, *Nat. Rev. Chem.* **2017**, *1*, 0041.
[21] G. Biffi, D. Tannahill, J. McCafferty, S. Balasubramanian, *Nat. Chem.* **2013**, *5*, 182 – 186.
[22] G. Biffi, M. Di Antonio, D. Tannahill, S. Balasubramanian, *Nat. Chem.* **2014**, *6*, 75 – 80.
[23] D. Drygin, A. Siddiqui-Jain, S. O'Brien, M. Schwaebe, A. Lin, J. Bliesath, C. B. Ho, C. Proffitt, K. Trent, J. P. Whitten, et al., *Cancer Res.* **2009**, *69*, 7653 – 7661.
[24] H. Xu, M. Di Antonio, S. McKinney, V. Mathew, B. Ho, N. J. O'Neil, N. Dos Santos, J. Silvester, V. Wei, J. Garcia, et al., *Nat. Commun.* **2017**, *8*, 14432.
[25] O. Domarco, D. Lötsch, J. Schreiber, C. Dinhof, S. Van Schoonhoven, M. D. García, C. Peinador, B. K. Keppler, W. Berger, A. Terenzi, *Dalton Trans.* **2017**, *46*, 329 – 332.
[26] M. D. García, C. Alvariño, E. M. López-Vidal, T. Rama, C. Peinador, J. M. Quintela, *Inorg. Chim. Acta* **2014**, *417*, 27 – 37.
[27] Y. Wu, J. Zhou, B. T. Phelan, C. M. Mauck, J. F. Stoddart, R. M. Young, M. R. Wasielewski, *J. Am. Chem. Soc.* **2017**, *139*, 14265 – 14276.
[28] I. Roy, S. Bobbala, J. Zhou, M. T. Nguyen, S. K. M. Nalluri, Y. Wu, D. P. Ferris, E. A. Scott, M. R. Wasielewski, J. F. Stoddart, *J. Am. Chem. Soc.* **2018**, *140*, 7206 – 7212.
[29] V. Blanco, M. D. García, A. Terenzi, E. Pía, A. Fernández-Mato, C. Peinador, J. M. Quintela, *Chem. Eur. J.* **2010**, *16*, 12373 – 12380.
[30] V. Blanco, M. D. García, C. Peinador, J. M. Quintela, *Chem. Sci.* **2011**, *2*, 2407 – 2416.
[31] C. Alvariño, A. Terenzi, V. Blanco, M. D. García, C. Peinador, J. M. Quintela, *Dalton Trans.* **2012**, *41*, 11992.
[32] E. M. López-Vidal, V. Blanco, M. D. García, C. Peinador, J. M. Quintela, *Org. Lett.* **2012**, *14*, 580 – 583.
[33] X. Yan, T. R. Cook, P. Wang, F. Huang, P. J. Stang, *Nat. Chem.* **2015**, *7*, 342 – 348.
[34] E. Y. N. Lam, D. Beraldi, D. Tannahill, S. Balasubramanian, *Nat. Commun.* **2013**, *4*, 1796.
[35] A. Henderson, Y. Wu, Y. C. Huang, E. A. Chavez, J. Platt, F. B. Johnson, R. M. Brosh, D. Sen, P. M. Lansdorp, *Nucleic Acids Res.* **2014**, *42*, 860 – 869.
[36] J. Mohanty, N. Barooah, V. Dhamodharan, S. Harikrishna, P. I. Pradeepkumar, A. C. Bhasikuttan, *J. Am. Chem. Soc.* **2013**, *135*, 367 – 376.
[37] S. Zhang, H. Sun, H. Chen, Q. Li, A. Guan, L. Wang, Y. Shi, S. Xu, M. Liu, Y. Tang, *Biochim. Biophys. Acta Gen. Subj.* **2018**, *1862*, 1101 – 1106.
[38] A. Laguerre, J. M. Y. Wong, D. Monchaud, *Sci. Rep.* **2016**, *6*, 1 – 10.
[39] J. Selinummi, P. Ruusuvuori, I. Podolsky, A. Ozinsky, E. Gold, O. Yli-Harja, A. Aderem, I. Shmulevich, *PLoS One* **2009**, *4*, e7497.
[40] G. Wang, N. Fang in *Imaging and Spectroscopic Analysis of Living Cells* (Ed.: P. M. Conn), Academic Press, New York, **2012**, pp. 83 – 108.
[41] R. Rodriguez, K. M. Miller, J. V. Forment, C. R. Bradshaw, M. Nikan, S. Britton, T. Oelschlaegel, B. Xhemalce, S. Balasubramanian, S. P. Jackson, *Nat. Chem. Biol.* **2012**, *8*, 301 – 310.
[42] J. Lefebvre, C. Guetta, F. Poyer, F. Mahuteau-Betzer, M. P. Teulade-Fichou, *Angew. Chem. Int. Ed.* **2017**, *56*, 11365 – 11369; *Angew. Chem.* **2017**, *129*, 11523 – 11527.
[43] F. Doria, M. Nadai, M. Zuffo, R. Perrone, M. Freccero, S. N. Richter, *Chem. Commun.* **2017**, *53*, 2268 – 2271.

Manuscript received: January 23, 2019
Revised manuscript received: April 17, 2019
Accepted manuscript online: April 19, 2019
Version of record online: May 8, 2019

Angewandte Chemie
Eine Zeitschrift der Gesellschaft Deutscher Chemiker

Supporting Information

Subcellular Duplex DNA and G-Quadruplex Interaction Profiling of a Hexagonal Pt^{II} Metallacycle

Olaya Domarco[+], Claudia Kieler[+], Christine Pirker, Carina Dinhof, Bernhard Englinger, Johannes M. Reisecker, Gerald Timelthaler, Marcos D. García, Carlos Peinador, Bernhard K. Keppler, Walter Berger,* and Alessio Terenzi**

anie_201900934_sm_miscellaneous_information.pdf
anie_201900934_sm_Video_S1.avi
anie_201900934_sm_Video_S2.avi

Table of Contents

Experimental Procedures

General

If not specified otherwise, chemicals were used in commercial grade (Sigma Aldrich and Thermo Fisher Scientific) from freshly opened containers. 5,10,15,20-Tetrakis(1-methyl-4-pyridinio)porphyrin tetra(p-toluenesulfonate) (TMPyP4) and solvents were purchased from Sigma Aldrich and used as received, without further purification. Pt-metallacycle **2** was synthesised as previously reported by us.[1] Mili-Q water was purified with a Milipore Gradient A10 apparatus. Merck 60 (230-400 mesh) silica gel was used for flash chromatography and Merck 60 F254 foils were used for thin layer chromatography. Proton and Carbon NMR spectra were recorded on a Bruker Avance 300 or a Bruker Avance 500 spectrometers. Mass spectrometry experiments were carried out in LCD-q-TOF Applied Biosystems QSTAR Elite spectrometer for low- and high-resolution ESI. Microwave-assisted reactions were carried out in an Anton Paar Monowave 300 reactor in a sealed reaction vial. The reaction mixture temperature was monitored via built-in IR sensor.
Buffers were prepared using MilliQ water and final pH values were measured using a Mettler Toledo pH-meter. Analysis and plotting of the data were carried out using Origin 9.5 (OriginLab Corp.), GraphPad Prism (version 5; GraphPad Software, San Diego, CA) and ImageJ 1.52g.[2]

The self-assembly of the final compound, having a hexagonal open box shape, occurred by mixing ligand **L1** with the platinum precursor $Pt(en)(NO_3)_2$ in water and using a microwave-assisted reaction at 150 °C for 3h.

Synthesis of 4,4'-([1,1'-biphenyl]-4,4'-diyl)bis(1-(2,4-dinitrophenyl)pyridin-1-ium)

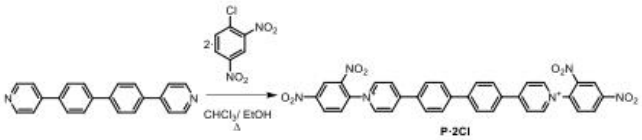

A solution of 4,4'-di(pyridin-4-yl)-1,1'-biphenyl (0.050 mg, 0.162 mmol) and 1-cloro-2,4-dinitrobenceno (0.098 mg, 0.486 mmol) in a mixture of EtOH/$CHCl_3$ 4:1 (25 mL) was heated at 90 °C for 72 hours. The solvent was removed under reduced pressure and the solid was washed with CH_2Cl_2 (10 mL) and CH_3CN (10 ml) to yield P·2Cl (48 mg, 48%). ^{1}H NMR (300 MHz, CD_3OD) δ (ppm): 9.32 (d, *J*= 2.5 Hz, 2H), 9.29 (d, *J*= 7.2 Hz, 4H), 8.96 (dd, *J*= 8.7, 2.5 Hz, 2H), 8.81 (d, *J*= 7.2 Hz, 4H), 8.39 (d, *J*= 7.1 Hz, 4H), 8.36 (d, *J*= 7.2 Hz, 4H), 8.18 (d, *J*= 8.5 Hz, 2H). HR-ESI-MS (m/z) calculated for $[M\text{-}2Cl]^+$ 2321.0744, found 321.0757.

Synthesis of L1·2NO₃

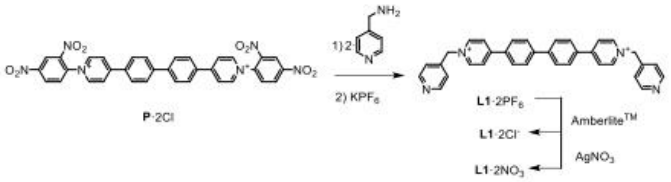

A solution of **P**·2Cl (80 mg, 0.07 mmol) and 4-(aminomethyl)pyridine (25 µL, 0.266 mmol) in MeOH (20 mL) was stirred overnight at room temperature. The solvent was removed under reduced pressure to obtain a solid residue, which was subjected to flash chromatography (SiO_2, CH3CN/NaCl (aq.)(0.6 M)/MeOH 4:1:1). The ligand containing fractions were combined, evaporated, dissolved in water and the obtained yellow solid was filtered. This solid was re-dissolved in the minimum amount of MeOH and an excess of KPF_6 was added to yield **L1**·2PF_6 (40 mg, 47%) ^{1}H NMR (500 MHz, CD_3CN) δ (ppm): 8.78 (d, *J*= 7.1 Hz, 4H), 8.71 (d, *J*= 6.1 Hz, 4H), 8.40 (d, *J*= 7.1 Hz, 4H), 8.13 (d, *J*= 8.7 Hz, 4H), 8.06 (d, *J*= 8.7 Hz, 4H), 7.35 (d, *J*= 6.0 Hz, 4H), 5.78 (s, 4H). ^{13}C NMR (125 MHz, CD_3CN) δ (ppm): 156.41 (C), 150.72 (CH), 144.87 (CH), 142.99 (C), 141.96 (C), 133.50 (C), 129.02 (CH), 128.48 (CH), 125.47 (CH), 122.80 (CH), 62.13 (CH_2). HR-ESI-MS (m/z) calculated for $[M\text{-}2PF_6]^{+2}$ 246.1151, found 246.1176.
L1·2PF_6 and Amberlite CG-400 (200 mg) were suspended into H_2O/MeOH (1:1, 50 mL), and stirred for 12 h. The resin was removed by filtration and the solvent was removed under reduced pressure to yield **L1**·2Cl (22 mg, 34%). A solution of **L1**·2Cl (22 mg, 0.039 mmol) and $AgNO_3$ (13.3 mg, 0.078 mmol) in H_2O/MeOH (1:1, 30 mL) was stirred at 25 ° for 12 h in the dark. The mixture was filtered and the filtrate was slowly evaporated to yield **L1**·2NO_3 (21.5 mg, 90%). ^{1}H NMR (500 MHz, D_2O) δ (ppm): 8.93 (d, *J*= 7.0 Hz, 4H), 8.62 (d, *J*= 6.3 Hz, 4H), 8.45 (d, *J*= 7.0 Hz, 4H), 8.13 (d, *J*= 8.6 Hz, 4H), 8.04 (d, *J*= 8.6 Hz, 4H), 7.42 (d, *J*= 6.3 Hz, 4H), 5.92 (s, 4H).

^{13}C NMR (125 MHz, D_2O) δ (ppm): 156.67 (C), 149.64 (CH), 144.65 (CH), 143.15 (C), 142.84 (C), 133.36 (C), 128.82 (CH), 128.25 (CH), 125.22 (CH), 123.10 (CH), 62.01 (CH_2).

Synthesis of 1·8NO$_3$

A suspension of **L1**·2NO_3 (40 mg, 0.068 mmol) and (en)Pt(NO_3)$_2$ (24.2 mg, 0.068 mmol) in H_2O (20 mL), was heated at 150 °C for 3 h using microwave-assisted heating. The resulted suspension was transferred into a round-bottom flask and the solvent was removed under reduced pressure to obtain a yellow solid (yield 95 %). ^{1}H NMR (500 MHz, D_2O) δ (ppm): 8.86 (d, *J* = 6.9 Hz, 8H), 8.83 (d, *J* = 6.8 Hz, 8H), 8.24 (d, *J* = 7.0 Hz, 8H), 7.87 (d, *J* = 8.6 Hz, 8H), 7.74 (d, *J* = 8.5 Hz, 8H), 7.67 (d, *J* = 6.9 Hz, 8H), 5.92 (s, 8H) 2.88 (s, 8H). ^{13}C NMR (125 MHz, D_2O) δ (ppm): 157.58 (C), 152.68 (CH), 146.83 (C), 145.49 (CH), 144.95 (C), 134.00 (C), 129.15 (CH), 128.63 (CH), 127.20 (CH), 126.04 (CH), 47.34 (CH_2).

1·8NO$_3$ (10 mg) was re-dissolved in the minimum amount of H_2O (2 mL) and an excess of KPF_6 was added to yield **1·8PF$_6$** as a yellow precipitate which was then filtered, washed with cold water (30 mL) and dried under vacuum. HR-ESI-MS (m/z) calculated for [M-3PF_6-H] $^+$21109.1709, found 1109.1837; calculated for [M-4PF_6-2H]$^+$21036.1849, found 1036.1942; calculated for [M-3PF_6]$^+$ 3739.783, found 739.7902; calculated for [M-4PF_6-H]$^+$3691.1257, found 691.1281; calculated for [M-5PF_6-2H]$^{+3}$ 642.4683; found 642.4689.

Interaction with G4 and B-DNA in solution

Steady State Absorption and Emission Spectroscopy. UV-Vis spectra overtime on a PerkinElmer LAMBDA 35 and Jasco V-650 spectrophotometers using 1 cm path-length quartz cuvettes. Fluorescence spectra were recorded on Horiba FluoroMax-4 and Fluoromax Plus-P spectrofluorometers (Kyoto, Japan). Scans were run at room temperature with excitation and emission slit widths as reported in the captions of the corresponding pictures.

For quantum yield measurements, all samples were freshly prepared. Absorption and emission spectra were recorded for samples with concentrations in the range 0.2−5 μM, where the absorption was between 0.01 and 0.08. Quantum yields were determined using quinine sulfate in 0.1 M H_2SO_4 as reference (with φ_F = 0.55 at λ_{exc} = 365 nm and λ_{em} = 451 nm).

Lifetime Measurements. Time-correlated single photon counting (TCSPC) measurements were carried out on a Fluoromax-4 apparatus equipped with a SPC Controller (FluoroHub, Horiba Jobin Yvon). The selected excitation source was a Horiba Nanoled N-370 (pulse < 1.2 ns). A 0.01% dilution of Ludox AS40 colloidal silica in purified water was used as prompt. Data were finally fitted using least squares methods with DAS6 Fluorescence Decay Analysis Software.

DNA sequences for binding studies. The oligodeoxynucleotides (ODNs) reported in Table S2 were purchased from IDT (Integrated DNA Technologies) in HPLC purity grade.

They were resuspended in IDTE buffer (10 mM Tris, 0.1 mM EDTA, pH 8.0, where Tris (tris-hydroxymethyl-aminomethane) is the actual buffer while EDTA (ethylenediaminetetraacetic acid) prevents DNA digestion by nuclease) to obtain 100 μM stock solutions. The extinction coefficient values at 260 nm provided by the manufacturer were used to determine the final ODNs strand concentration.

Lyophilized calf thymus DNA (ct-DNA) was purchased from Sigma-Aldrich and resuspended in IDTE buffer. Final DNA concentration in bases was determined by UV spectrophotometry using 6600 M^{-1} cm^{-1} as molar absorption coefficient at 260 nm.

All along the text, concentration of DNA sequences is reported as strand molarity. When explicitly stated, ODN concentrations were reported in bases.

FRET melting assay. FRET experiments were performed on a 96-well format Applied Biosystems® 7500 Real-Time PCR cycler equipped with a FAM (6-carboxyfluorescein) filter (λ_{ex} = 492 nm; λ_{em} = 516 nm). ODNs were purchased with the probes FAM and TAMRA (6-carboxy-tetramethylrhodamine) attached at the 5'- and 3'- ends, respectively.

To afford G4 folding, FRET ODNs stock solutions were diluted to the desired concentration using 60 mM potassium cacodylate buffer (pH 7.4) and then heated to 95 °C for 5 min, followed by slowly cooling to room temperature overnight. In the final mixes, ODNs final concentration was set to 0.2 μM (total volume of 30 μl). Control TMPyP4 was previously dissolved in DMSO to give 1 mM stock solutions and further diluted with the buffer reaching a total percentage of DMSO never above 0.1 %.

The melting of *c-Kit2* and *h-Telo* G4s (0.2 μM) stabilised by Pt metallacycle **1** was also monitored in a competition assay in the presence of increasing concentration of a non-fluorescent DNA structure. In particular ct-DNA was used to represent a duplex structure while the sequence G4-nl was selected for a quadruplex with no loops.

FAM emission data were collected in duplicate or triplicate in the range 25-95 °C (with a ramp of 1 °C every 30 s). To compare different sets of data, emission data were normalised.[3] $T_{1/2}$ is defined as the temperature at which the normalised emission is 0.5.

Circular dichroism. CD spectra were recorded on Chirascan™ CD (by AppliedPhotophisics), using 1 cm path-length quartz cuvettes, at room temperature using the following parameters: bandwidth: 1.0 nm, time per point: 0.5 s, repeats: 4. The titrations were carried out by adding increasing amounts of **1** to the selected ODN at constant concentration.

Molecular Modelling. Molecular docking was carried out using AutoDock Vina 1.1.2.[4] PDB IDs 2KQH and 1BNA were used as models for *c-Kit2* and B-DNA quadruplexes, respectively.

The structure of compound **1** was optimised by DFT using B3LYP functional,[5–7] Lanl2dz pseudopotential basis set for platinum,[8] and 6-31G(d,p) basis set for the other atoms.[9,10] Calculations were performed with Gaussian09.[11]
Autodock Tools package was used to prepare receptors and the platinum SCC for docking calculations.[12] A grid box large enough to contain the whole DNA structure was created. Since Vina formally treats metals as H-bond donors and no significant changes were expected, Pt(II) was changed with Ni(II) just to retain the square planar coordination around the metal centre. Figures were rendered using Chimera software.[13]

Cell studies

Cell Culture. The human cancer cell lines U2OS, MCF-7, T98G, and U373MG (compare Table S2) were purchased from American Type Culture Collection (Manassas, VA, USA) and cultured in respective growth media (U2OS in IMDM, MCF-7 in DMEM, T98G and U373MG in MNP medium), supplemented with 10% fetal bovine serum (FBS South America, Biowest, Nuaillé, France). VM-1 cells were obtained from the Institute of Cancer Research (Vienna, Austria) and grown in RPMI-1640, supplemented with 10% FBS. Non-malignant human lung fibroblasts (HLF) were taken in culture from a surgical pneumothorax specimen at the ICR Vienna and non-transformed HaCaT keratinocytes were donated by Prof. Fusenig, DKFZ Heidelberg, Germany. All cells cultures were incubated at 37 °C and 5% CO_2 and regularly screened for *Mycoplasma* contamination (Mycoplasma Stain kit, Sigma, St. Louis, Missouri, USA).

Cell viability assays (MTT). 2-3x10^4 cells/ml were seeded in 96-well plates and left to adhere overnight. Cells were treated with 0-50 µM of metallacycle **1** and its ligand **L1** for 72h, followed by determination of cell viability by the 3-(4,5-dimethylthiazol-2-yl)-2,5-diphenyltetrazolium bromide (MTT)-based vitality assay (EZ4U, Biomedica, Vienna, Austria) according to the manufacturer's instructions. Concentrations of **1** and **L1** leading to a reduction of cell number by 50% (IC_{50}) were calculated from whole dose-response curves generated by GraphPad Prism 5 software. Each data point in the response curves represents the mean ± SD of three replicates of one representative experiment, which was performed at least three times. Interaction of **1** with both ThT and PDS was done in 72 h co-exposure assays and cell viability again determined by MTT assay. To investigate a possible interaction between **1**- and cisplatin (Cis) on (Cis)-mediated anticancer activities, co-exposure experiments were performed at the indicated concentrations of both compounds. MTT assay - detecting mitochondrial activity - might be prone for misleading results (overestimation of cell viability) in case of cisplatin. This DNA-damaging compound frequently induces in malignant cells a cell cycle arrest in G2 phase with massive enlarging of cell bodies but lack of apoptosis induction. Hence, we used in these experiments instead of MTT assays the CellTiter-Glo® Luminescent Cell Viability Assay (Promega) detecting cellular ATP contents following the instructions of the manufacturer. The other settings were kept as in MTT assays.

Clonogenic assay. 1-2x10^3 cells/ml were seeded in 24-well plates and incubated overnight, followed by treatment with 0-20 µM of **1** and **L1**. After 7-day drug exposure, cells were fixed with MeOH and stained with crystal violet (0.1 mg/ml in PBS). Images of each well were taken (Nikon Digital Camera D3200, Minato, Tokyo, Japan) and plates were scanned on a Typhoon scanner (Typhoon TRIO Variable Mode Imager, GE Healthcare Life Sciences). Colony growth was determined by calculating integrated area densities with the ImageJ 1.51f software (Wayne Rasband, National Institutes of Health, USA).

Drug uptake and cell cycle analysis by flow cytometry. U2OS cells resuspended in PBS were treated with 50 µM **1** and **L1** for 1h. Fluorescence intensity measurements were carried out on a LSRFortessa flow cytometer (BD Biosciences, East Rutherford, NJ, USA), using 405 nm laser excitation and 450/50 nm ("Horizon V450"), 605/12 nm ("Qdot 605"), and 655/8 nm ("Qdot 655") bandpass emission filters, as well as 355 nm laser excitation and a 450/50 nm ("DAPI") bandpass emission filter. For longer-term drug uptake measurements, U2OS cells were resuspended in serum-free RPMI 1640 media (Sigma-Aldrich, Missouri, USA), containing 3-(N-morpholino)propanesulfonic acid (MOPS; Sigma-Aldrich) and 4-(2-hydroxyethyl)-1-piperazineethanesulfonic acid (HEPES; Sigma-Aldrich, Missouri, USA). Cells were treated with indicated concentrations of **1** and **L1** or with **1** in combination with the indicated concentrations of cisplatin (Cis, 2mM stock prepared in PFS, Sigma) or pyridostatin (PDS, 10 mM stock in DMSO, Sigma) and fluorescence intensity was measured by flow cytometry using 405 nm laser excitation and the Horizon V450 bandpass emission filter at the indicated time points. Data were analysed using Flowing Software 2.5.1 (Perttu Terho, Turku, Finland). For cell cycle analysis, 2x10^5 cells/well were seeded into 6-well plates. After overnight incubation, cells were treated with indicated concentrations of **1** and **L1**. After 24h drug exposure, cells were fixed with 70% ice-cold EtOH at -20°C overnight. Fixed cells were treated with RNase A (0.79 Kunitz units/ml, Sigma-Aldrich, Missouri, USA) for 30 min at 37°C and stained with propidium iodide (1 mg/ml in PBS; Sigma-Aldrich, Missouri, USA) for 30 min at 4°C. Fluorescence intensity was measured by flow cytometry and quantified with the Cell Quest Pro Software (BD Biosciences).

Metaphase chromosome preparation. Metaphase chromosome preparation of MCF-7 cells was performed according to standard protocols and as described by Pirker et al.[14]

Emission fingerprinting with lambda stacks. MCF-7 cells fixed with MeOH were incubated with either 50 µM 1 or L1 for 30 min at RT. After washing with 1x PBS, cells were mounted with Vectashield (Vector Laboratories, Inc., Burlingame, CA, USA) without DAPI. Lambda stacks for **1** and **L1** were acquired with a Zeiss LSM 780 confocal microscope and Zen 2.3 SP1 software (Carl Zeiss microscopy, Germany) using a Plan-Apochromat 63×/1.4 NA Oil DIC M2763x objective with immersion oil and 405 nm laser line. The emission of the drugs was determined in the range of 411-687 nm with a bandwidth of 9 nm. Data were evaluated with Zeiss Zen 2.1

software (Carl Zeiss). Emission spectral profiles were obtained using the linear unmixing tool by normalizing the signal intensity values and plotting them on a linear graph versus the corresponding emission wavelengths.

Live Cell Microscopy. 3-5x10^4/ml cells were seeded in 8-well chamber slides (Ibidi, Martinsried, Germany). After overnight incubation, cells were either additionally pre-treated for 24h with 1 µM TMPyP4 or cells were treated directly with the indicated concentrations of **1** and **L1**. Alternatively, cells were pretreated for 30 min with the G-quadruplex probe 5 µM Thioflavin T (ThT, Sigma) followed by addition of 5 µM **1**. Images were taken every 30 minutes over a period of 24h (29h for Video S1) on a live cell microscope (Visitron Systems, Puchheim, Germany) using a Plan-Apochromat 40×/1.4 NA Oil DIC M27 objective and the imaging software VisiView®. Lumencor (Beaverton, USA) spectra colour LEDs were used for fluorescence illumination (395/25 nm excitation and 460/50 nm bandpass emission filter for blue, 475/34 nm excitation and 525/50 nm emission filter for green and 640/30 nm excitation and 700/75 nm emission filter for red. Images were captured with a PCO Edge 4.2 sCMOS camera and quantified using ImageJ 1.51f software (Wayne Rasband, National Institutes of Health, USA).

Fluorescence microscopy. Cells were seeded in 8-well chamber slides with removable silicone walls (Ibidi). After overnight incubation, cells were stained and/or fixed in different sequences as appropriate and indicated in the respective figure legends. Alternatively, for nuclear staining cells were in some cases cytospin prepared instead of being grown on chamber slides. For staining and competition experiments with specific G-quadruplex probe Thioflavin T (ThT, Sigma), nucleolar probe SYTO® RNASelect green (SYTO, Molecular Probes, Eugene, OR) and MitoTracker® Red CMXRos mitochondrial stain (250nM; Molecular Probes) cells were fixed in MeOH (-20°C, 15 min). Fluorescence images were taken on a DMRXA (Leica, Wetzlar, Germany) equipped with a monochrome fluorescence camera based on a CCD sensor and a HCX PL APO 63x (1.32 – 0.6) or a PL APO 100x (1.4 – 0.7) oil objective using DAPI (λ_{exc} 350/50, λ_{em} 460/50), FITC (λ_{exc} 495/25, λ_{em} 537/29), or Cy3 (λ_{exc} 546/22, λ_{em} 590/23) filter cubes. Photomicrographs were processed by VisiView software (Visitron Systems, Puchheim, Germany) at the indicated settings. For photobleaching experiments, **1**-stained cells were exposed for longer periods to UV excitation. Fluorescence images were taken with a PL APO 100x (1.4 – 0.7) oil objective in time-lapse mode with one frame every 5 seconds at an illumination time of 10 ms and the DAPI filter cube (350/50 excitation, 460/50 emission). Photomicrographs were processed by VisiView software (Visitron Systems, Puchheim, Germany) at Max/Min (range) autoscale settings.

Confocal laser-scanning microscopy (CLSM). 3-7x10^4/ml U2OS and MCF-7 cells were seeded in 8-well chamber slides with removable silicone walls (Ibidi). After overnight attachment, staining with **1** was performed either in living or in fixed cells. For fixation with PFA, cells were washed with 1xPBS before adding a 4% PFA containing PBS solution for 30min at RT. Following PFA quenching with a PBS-solution containing 0.1 M glycin, cells were washed with 1xPBS and subsequent permeabilisation was carried out using 0.1% Triton-X-100 in 1xPBS for 15min at RT. After washing again with 1xPBS, cells were used for immunofluorescence staining. For fixation with MeOH, washed cells were air-dried at least 1 hour before adding ice-cold MeOH for 10 min at -20°C. Following PBS-washing, cells were ready for subsequent staining procedures. For live cell staining, cells were treated with 50 µM **1** for 30-60 min at 37°C before fixation. Staining of fixed cells as well as metaphase chromosome spreads was performed by adding a 50 µM drug dilution in 1xPBS for 30 min at RT. For immunofluorescence staining, MeOH-/ PFA-fixed cells as well as metaphase chromosome preparations were blocked for 45min at RT with 1x PBS-BSA (0.2%) containing 10% FBS (for PFA fixed cells, 0.1% Triton-X-100 was additionally added to the blocking buffer). Blocked cells were incubated with BG4 antibody[15,16] (Mouse IgG1, from AbsoluteAntibody) diluted 1:200 in 1x PBS-BSA (0.2%) and 3% FBS (for PFA fixed cells 0.1% Triton-X-100 was additionally added to the antibody dilution) and incubated overnight at 4°C. After washing with 1x PBS, cells were incubated with secondary AB (AF594, Thermo Fisher Scientific, Waltham, MA, USA) diluted 1:500 in 1x PBS-BSA (0.2%) and 3% FBS (for PFA fixed cells 0.1% Triton-X-100 was added) for 1h at 37°C or RT. When indicated, cells or metaphase chromosome spreads were further counterstained with 50 µM **1** or **L1** for 30 min at RT. For counterstaining with 4',6-diamidino-2-phenylindole (DAPI, Thermo Fisher Scientific, Waltham, MA, USA), fixed nuclei and metaphase chromosomes were either incubated for 10 min with 1.5 µg/ml DAPI at RT or slides were mounted with Vectashield containing 1.5 µg/ml DAPI (Vector Laboratories, Inc., Burlingame, CA, USA). Samples were stored in the dark at 4°C until subsequent analysis with a Zeiss LSM700 confocal microscope (Carl Zeiss microscopy, Germany) for fluorescence imaging in DAPI (405 nm excitation and 450/90 nm emission) and AF594 (555 nm excitation and >585 nm emission) channels with a Plan-Apochromat 63×/1.4 NA Oil DIC M27. Transmitted light images were acquired with the 405 nm violet laser line in DICIII with T-PMT. For super-resolution imaging, a Zeiss LSM 880 microscope equipped with an Airyscan detector, a laser diode for 405 nm excitation, a BP 420-480 emission filter and a 63x/1.40 Plan-Apochromat, Oil, DIC III objective was used. Micrographs were evaluated with Zeiss Zen 2010 B SP1 software (Carl Zeiss).
Three-dimensional surface plots of single pixel intensities, derived from inverted DIC images of cropped nuclei were generated using the "3D Surface Plot" plugin in the FIJI distribution package of ImageJ software. Two-dimensional pixel intensity plots from lines indicating the region of interest in fluorescence and DIC channels were generated using the "Plot Profile" analysis tool in ImageJ software.

mRNA expression microarray. The impact of **1** (25 µM, 24 h exposure) and PDS (15 µM, 24 h exposure) on whole-genome gene expression was performed on 4×44K whole genome oligonucleotide-based gene expression arrays (Agilent, Santa Clara, USA) as previously described.[17,18] Gene expression data were preprocessed in R using the LIMMA package and evaluated by gene set enrichment analysis (GSEA) (http://www.broadinstitute.org/gsea/msigdb/index.jsp) against the KEGG database gene sets. Additionally, the set of genes located in chromosomal regions enriched for G4 structures was derived from supplementary Table S4 in Lam et al. 2012.[19]

Statistical analysis. Data were analysed using GraphPad Prism. If not specified otherwise, data are given as mean values ± standard deviation (SD) of triplicate values of one representative experiment, performed at least three times. For comparison of two groups, two-tailed Student's t-test was carried out. P-values, t-values (t) and degrees of freedom (DF) of each analysis are indicated in corresponding figure legends. Comparison of multiple groups was performed using one-way analysis of variance (ANOVA) with Bonferroni post-test. P-values below 0.05 were considered as statistically significant and marked with asterisks: *** $p < 0.001$.

Table S1. IC_{50} values for **1** and **L1**

Cell line	U2OS		MCF-7		VM-1		U373MG		T98G		HaCaT		HLF	
	Mean IC_{50}	± SD	Mean IC_{50}	± SD	Mean IC_{50}	± SD	Mean IC_{50}	± SD	Mean IC_{50}	± SD	Mean IC_{50}	± SD	Mean IC_{50}	± SD
L1*	35.58	4.64	35.47	1.55	>50	-	44.14	3.13	43.30	1.08	>50	-	36.43	8.31
1	31.67	3.21	29.81	4.64	45.34	2.07	35.85	3.56	37.28	1.41	>50	-	26.04	5.21

* While **L1** and **1** showed similar IC_{50} values in the MTT tests, when observed in live-cell imaging, metallacycle **1** revealed a higher tendency to induce cell death.

Table S2. 5'-3' ODNs sequences. In *ds-DNA* Heg linker is $[(-CH_2-CH_2-O-)_6]$

ODN	Sequence
h-Telo	AGG GTT AGG GTT AGG GTT AGG G
c-Kit1	AGG GAG GGC GCT GGG AGG AGG G
c-Kit2	CGG GCG GGC GCG AGG GAG GGG
hTERT	GGG GGC TGG GCC GGG GAC CCG GGA GGG GTC GGG ACG GGG CGG GG
hTERT-s	AGG GGA GGG GCT GGG AGG GC
Bcl2	AGG GGC GGG CGC GGG AGG AAG GGG GCG GGA GCG GGG CTG
VEGF	CGG GGC GGG CCT TGG GCG GGG T
ds-DNA (duplex)	TATAGCTATA-Heg-TATAGCTATA

Table S3. Overview of the different cell lines used in this project

Cell line	Disease	Tissue	Growth medium	Source
U2OS	Osteosarcoma	Bone	IMDM (Sigma-Aldrich)	ATCC
MCF-7	Adenocarcinoma	Mammary gland, breast	DMEM (Sigma-Aldrich)	ATCC
T98G	Glioblastoma	Brain	MNP (Sigma-Aldrich)	ATCC
U373MG	Glioblastoma	Brain	MNP (Sigma-Aldrich)	ATCC
VM-1	Melanoma	Skin	RPMI 1640 (Sigma-Aldrich)	ICR[20]
HaCaT	Keratinocytes, non-malignant	Skin	RPMI 1640 (Sigma-Aldrich)	Prof. Fusenig, DKFZ Heidelberg
HLF	Fibroblasts, non-malignant	Lung; pneumothorax	RPMI 1640 (Sigma-Aldrich)	ICR

VM: Vienna Melanoma
IMDM: Iscove's Modified Dulbecco's Medium
DMEM: Dulbecco's Modifies Eagle's Medium
MNP: Modified Eagle's Medium supplemented with 0.2% Na-pyruvate and 1% non-essential amino acids
RPMI: Roswell Park Memorial Institute
ATCC: American Type Culture Collection
ICR: Institute for Cancer Research, Vienna

Results and Discussion

Spectroscopic features of metallacycle 1

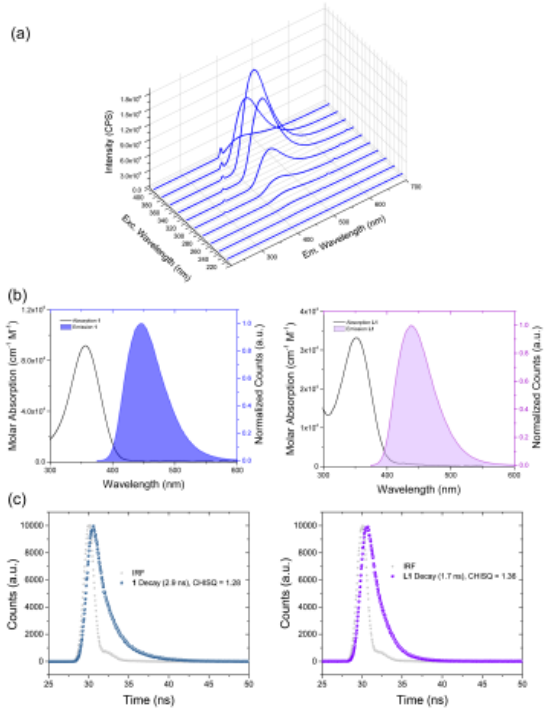

Figure S1. Fluorescence emission of metallacycle 1 and its ligand L1. (a) Full excitation-emission 3D landscape of 5 μM **1** in Tris-HCl 5 mM, KCl 50 mM, pH=7.8, obtained by fluorescence spectroscopy (Slit width: 0.5 nm). Spectra are shown for excitation wavelengths from 220 nm to 400 nm. 1st and 2nd order Rayleigh scattering can be seen as diagonal ridges. (b) Absorption (black) and emission (filled area) spectra of **1** and **L1** in Tris-HCl 5 mM, KCl 50 mM, pH=7.8. (c) Excited state lifetime decay for **1** and **L1** in Tris-HCl 5 mM, KCl 50 mM (pH=7.8) measured in a time-correlated single photon counting (TCSPC) setup. Both compounds exhibit a mono-exponential decay (violet and blue dots). IRF (grey dots) = instrument response function (prompt).

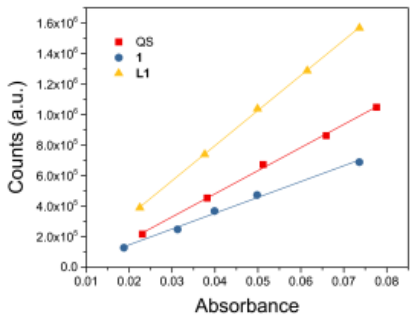

Figure S2. Quantum yield evaluation of 1 and L1. Plot of emission vs absorption in water of **1**, **L1** and quinine sulfate (QS) for quantum yield evaluation.

Stability of metallacycle 1

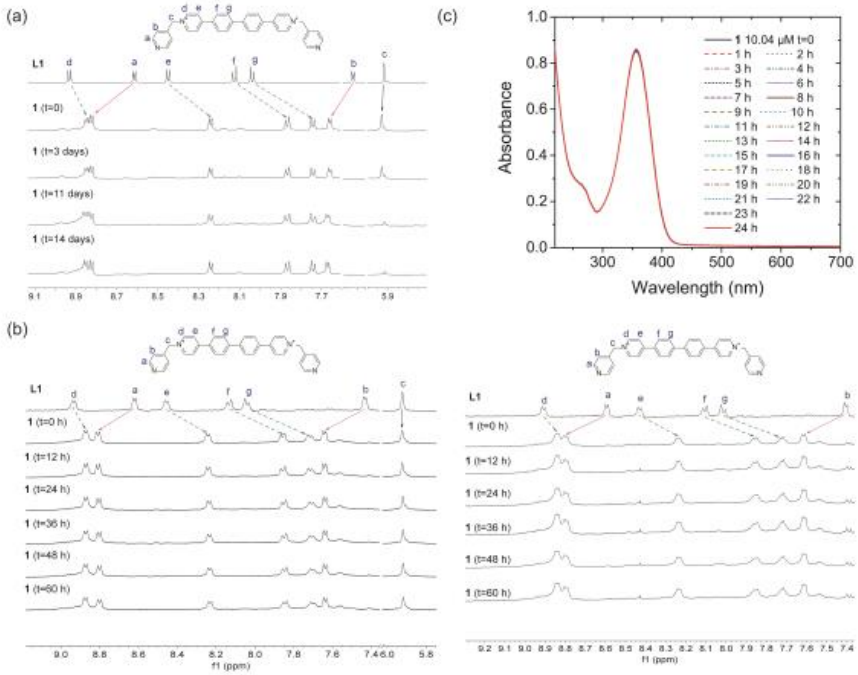

Figure S3. Stability overtime of compound 1. (a) NMR spectra of **1** overtime in (a) D_2O and (b) cell culture medium RPMI without (left) and with (right) fetal bovine serum (with 10% D_2O) (b) UV-Vis spectra of **1** overtime in the buffer Tris-HCl 5 mM, KCl 50 mM (pH=7.8).

Duplex DNA vs G4 binding studies

At first, we assessed the capacity of our platinum compound **1** and its constituent ligand **L1** to bind/stabilise duplex and/or quadruplex DNA. A standard FRET assay was performed using a self-complementary duplex model and the typical telomeric sequence *h-Telo*, arranged in a hybrid G4 topology.[21] Ligand **L1** did not affect the melting temperature of the duplex and had a minor influence on the stability of the quadruplex when compared to **1** (Figure S4). The metallacycle strongly stabilised the telomeric G4 ($\Delta T_{1/2}$ = 24.9) and, four time less the duplex ($\Delta T_{1/2}$ = 7.2) at the same concentration. The stabilisation produced by **1** on both duplex and quadruplex was found to be concentration dependent (Figure S4a,b). Interestingly, only in the case of *h-Telo* a significant stabilisation was observed at increasing concentration of **1**, reaching $\Delta T_{1/2}$ values even higher than the one obtained with the control molecule TMPyP4, a porphyrin known to be a good G4 binder, though with poor selectivity.[22]

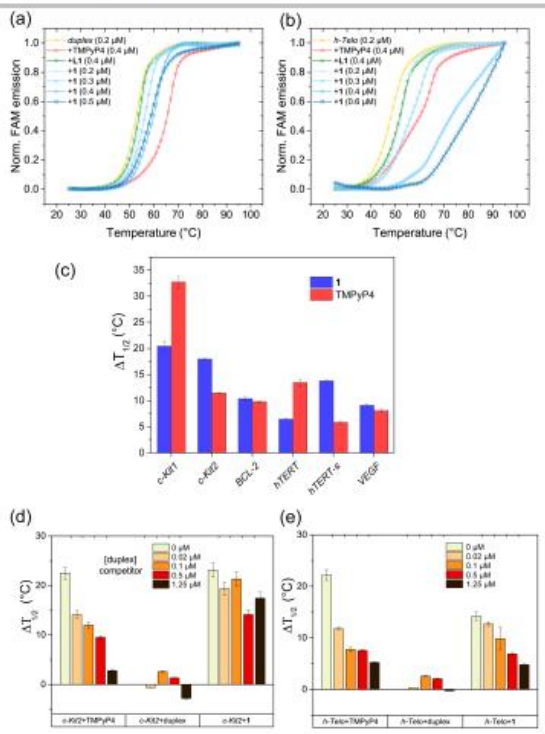

Figure S4. Interaction with duplex DNA and G4 sequences. (a-b) FRET melting profiles of (a) *ds-DNA* duplex and (b) *h-Telo* G4 upon interaction with ligand **L1**, metallacycle **1** and control TMPyP4 at the indicated concentrations. Buffer: 60 mM potassium cacodylate, pH 7.4. (c) Bar graph representing stabilization temperatures, $\Delta T_{1/2}$ (°C), obtained by FRET melting assays for **1** and TMPyP4 (0.4 μM) binding to the investigated G4 sequences (0.2 μM). Buffer: 60 mM potassium cacodylate, pH 7.4. (d-e) Stabilization of (d) *c-Kit2* and (e) *h-Telo* G4s (0.2 μM) by **1** (0.5 μM) and control compound TMPyP4 (0.5 μM) in the presence of increasing concentration of duplex DNA competitor (ct-DNA). Concentration of G4s are reported per strand; ct-DNA concentration has been divided by 20 (average base length of a G4 sequence) to make a fair comparison for selectivity. For the competition assay, 10 mM potassium cacodylate buffer (pH 7.4) supplemented with 95 mM of LiCl was used.[22]

Encouraged by these results, other FRET melting assays were performed using **1** (and control TMPyP4) with G-rich oncogene sequences known to fold in G4s with different arrangements (Figure S4c). Interestingly, compound **1** turned out to be more active than the porphyrin when bound to *c-Kit2* and *hTERT-s* oligonucleotides, which form standard parallel G4s.[23,24] An opposite situation was observed when the metallacycle was mixed with *c-Kit1* and *hTERT* sequences, known to form a parallel quadruplex with a unique cleft,[25] and a parallel G4 with a 26-base long looping hairpin,[24] respectively. These findings would suggest that **1** interacts preferentially via stacking on the guanine quartets while the presence of loops and/or cavities on the G4 secondary structure likely diminishes its affinity.

Competitive FRET experiments were performed using the *c-Kit2*-**1** and *h-Telo*-**1** systems in the presence of increasing amounts of duplex-DNA. *c-Kit2* thermal stabilization induced by **1** was less affected by the duplex competitor when compared with TMPyP4 (Figure S4d). On the other hand, the addition of a duplex to the *h-Telo*-**1** system (Figure S4e) produced a clear destabilisation effect.

UV-Vis and fluorescence titrations were performed in order to quantify the interaction between **1** and duplex or G4 DNA models. The UV-Vis spectrum of compound **1** (solid black line, Figure S5a,b), when exposed to increasing concentrations of *c-Kit2*, showed a hypochromic effect accompanied by a large red-shift. These effects, especially the red shift, were less pronounced in the case of **1** interacting with the duplex model ct-DNA. At the same time, a strong fluorescence quenching was observed after the interaction of **1** with the same parallel G4 in solution (Figure S6a) and the duplex model *ds-DNA* (Figure S6b). Stern-Volmer constants (Figure S6c) revealed that the quenching effect was one order of magnitude lower the interaction with *ds-DNA*. Binding constants (K_b) have been calculated from UV-Vis and fluorescence titrations and in both cases the interaction with the quadruplex motif *c-Kit2* resulted higher of one to two order of magnitude.

Overall, these thermal and spectroscopic data suggest that, while it is true that metallacycle **1** binds both duplexes and quadruplexes, it can be said that the platinum compound has a moderate preference for (parallel) G4s, behaving better than the poorly selective TMPyP4.

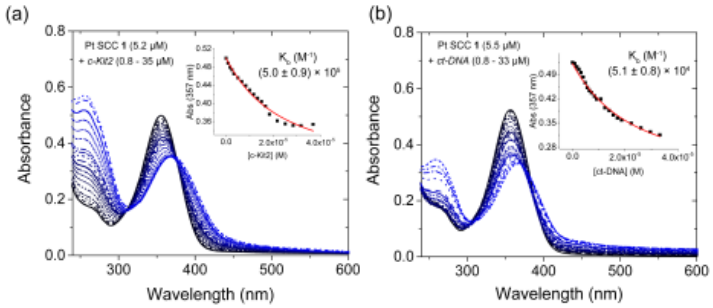

Figure S5. UV-Vis titrations. (a-b) UV-Vis absorption spectrum of **1** in combination with increasing amount of (a) *c-Kit2* G4 and (b) ct-DNA. In the insets the plot of the absorbance at 357 nm for the calculation of the binding constants (K_b). K_b values have been calculated using previously reported equations, and the related fitting was obtained implementing such equations in Origin software.[26] Buffer: Tris-HCl 5 mM, KCl 50 mM, pH=7.8.

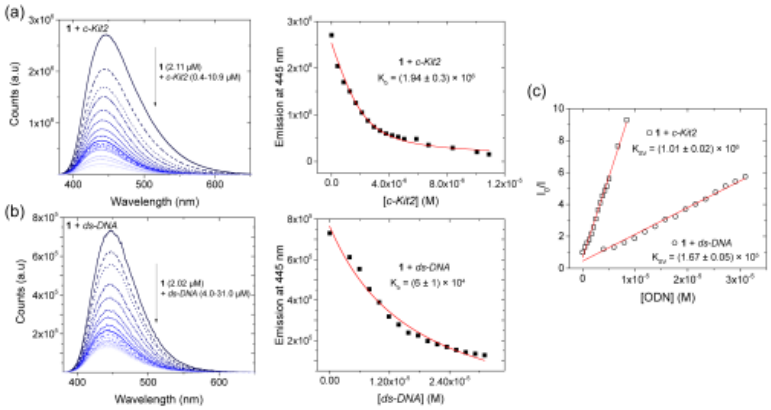

Figure S6. Emission of 1 interacting with G4 and B-DNA. Fluorescence titration of compound **1** with increasing amounts of (a) *c-Kit2* and (b) *ds-DNA* sequences in Tris-HCl 5 mM, KCl 50 mM, pH=7.8. λ_{exc} = 360 nm, Slits width = 5.0/0.6 nm for *c-Kit2* and 0.6/0.6 nm for *ds-DNA*. In the right column the plot of the emission at 445 nm for the calculation of the binding constants. (c) Stern-Volmer plots for fluorescence quenching of **1** by *c-Kit2* and *ds-DNA* oligonucleotides. Binding (K_b) and Stern-Volmer constants (K_{SV}) have been calculated using previously reported equations, and the related fitting was obtained implementing such equations in Origin software.[26,27] For Stern-Volmer data fitting, only the linear portion of the plot was used. Concentration of the ODNs are reported in bases.

Circular dichroism measurements and docking calculations were performed to give insights on the metallacycle mode of binding to DNA. The addition of increasing aliquots of **1** to a *c-Kit2* solution induced the appearance of a slight CD band at around 380 nm, without dramatic shifts in the quadruplex fingerprint region of the spectrum (200-300 nm), indicating that the general parallel arrangement of the G4 is preserved after the interaction (probably via stacking on top of the tetrads) (Figure S7a). This scenario is confirmed by docking simulations (Figure S7c) where metallacycle **1** uses one of its viologen chromophores to sit on top of the terminal G-tetrad. It is worth noting that both CD and simulations indicated that **1** acts as a major groove binder when interacting with duplex DNA (Figures S7b and S7d).

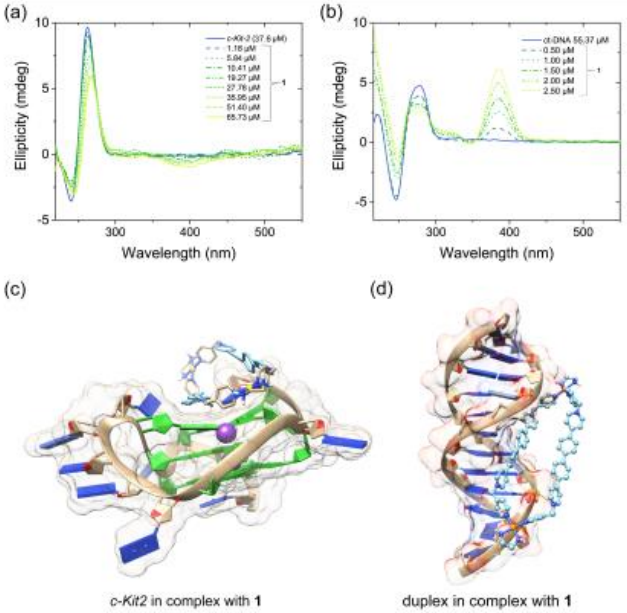

Figure S7. Circular dichroism and docking calculations. (a-b) CD spectra of (a) *c-Kit2* G4 and (b) ct-DNA in the presence of increasing aliquots of metallacycle **1**. Concentrations of both *c-Kit2* and ct-DNA are reported in bases. Buffer: Tris-HCl 5 mM, KCl 50 mM, pH=7.8. (c-d) Cartoon showing the best docking binding pose of **1** with (c) parallel G4 *c-Kit2* (PDB entry 2KQH) and (d) a duplex DNA model (PDB entry 1BNA).

Cell studies

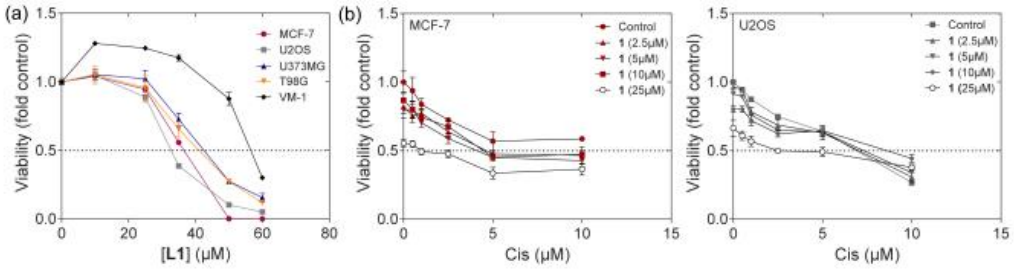

Figure S8. Impact of L1 and 1 in combination with cisplatin on cancer cell viability. (a) Viability of U2OS, MCF-7, U373MG, T98G and VM-1 cells was assessed by MTT assay following 72h exposure to increasing **L1** concentrations in the range of 0-50 μM. Data are normalized to untreated controls. The dashed line refers to 50% cell viability and indicates the IC_{50}. Each data point represents the mean ± SD of three replicates of one representative experiment, which was performed at least three times. (b) Impact of **1** at the indicated concentrations on the activity of cisplatin (Cis) was assessed under conditions as in (a). Cell viability was in these experiments assessed by CellTiter-Glo® Luminescent Cell Viability Assay (Promega) detecting cellular ATP contents following the instructions of the manufacturer.

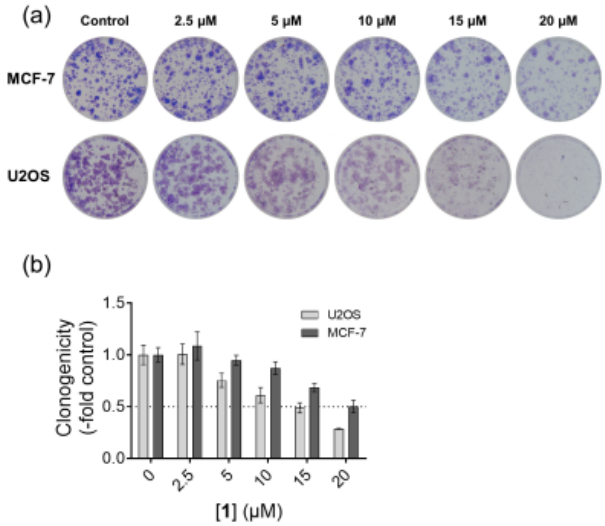

Figure S9. Impact of metallacycle 1 on the colony formation capacity of MCF-7 and U2OS cells. 1x10^3 (U2OS) or 2x10^3 (MCF-7) cells/ml were exposed for 7 days to increasing concentrations of **1** (0-20 µM). (a) Representative pictures after MeOH fixation and crystal violet staining upon treatment with the indicated drug concentrations taken with a Nikon Digital Camera D3200. The upper panel refers to MCF-7 cells, the lower panel to U2OS cells. (b) Colony growth of U2OS and MCF-7 cells given as relative integrated density values normalized to the untreated controls, quantified with ImageJ 1.51f software and illustrated as bar graphs with GraphPad Prism 5.0 software. The dashed line refers to 50% colony forming capacity. Bars indicate duplicate values of one representative experiment, performed at least three times and are presented as mean ± SD.

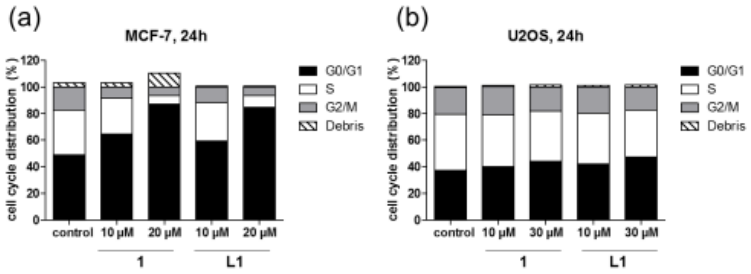

Figure S10. Effects on cell cycle distribution upon treatment with 1 and L1. (a) MCF-7 and (b) U2OS cells were exposed for 24 h with either (a) 10 and 20 µM or (b) 10 and 30 µM of the indicated compounds. DNA content of the cells was measured following EtOH fixation and PI staining with flow cytometry and quantified with the Cell Quest Pro Software. Data are presented as number of cells (%) in G0/G1, S and G2/M phase using GraphPad Prism 5.0 software and refer to one representative experiment, which was performed at least three times.

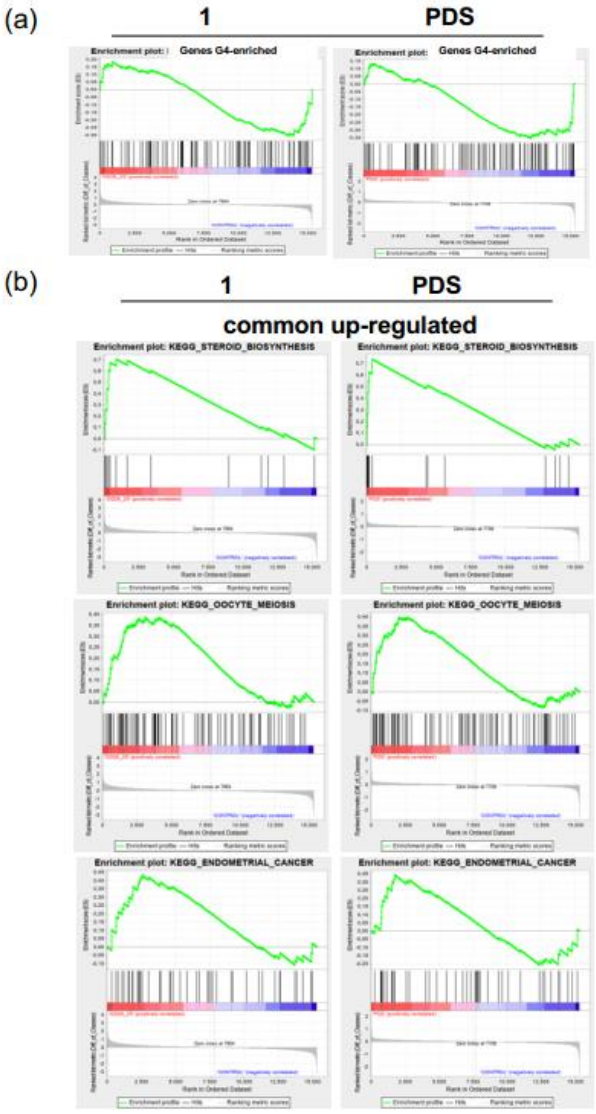
(a)
1
PDS
Enrichment plot: Genes G4-enriched
Enrichment plot: Genes G4-enriched
(b)
1
PDS
common up-regulated
Enrichment plot: KEGG_STEROID_BIOSYNTHESIS
Enrichment plot: KEGG_STEROID_BIOSYNTHESIS
Enrichment plot: KEGG_OOCYTE_MEIOSIS
Enrichment plot: KEGG_OOCYTE_MEIOSIS
Enrichment plot: KEGG_ENDOMETRIAL_CANCER
Enrichment plot: KEGG_ENDOMETRIAL_CANCER

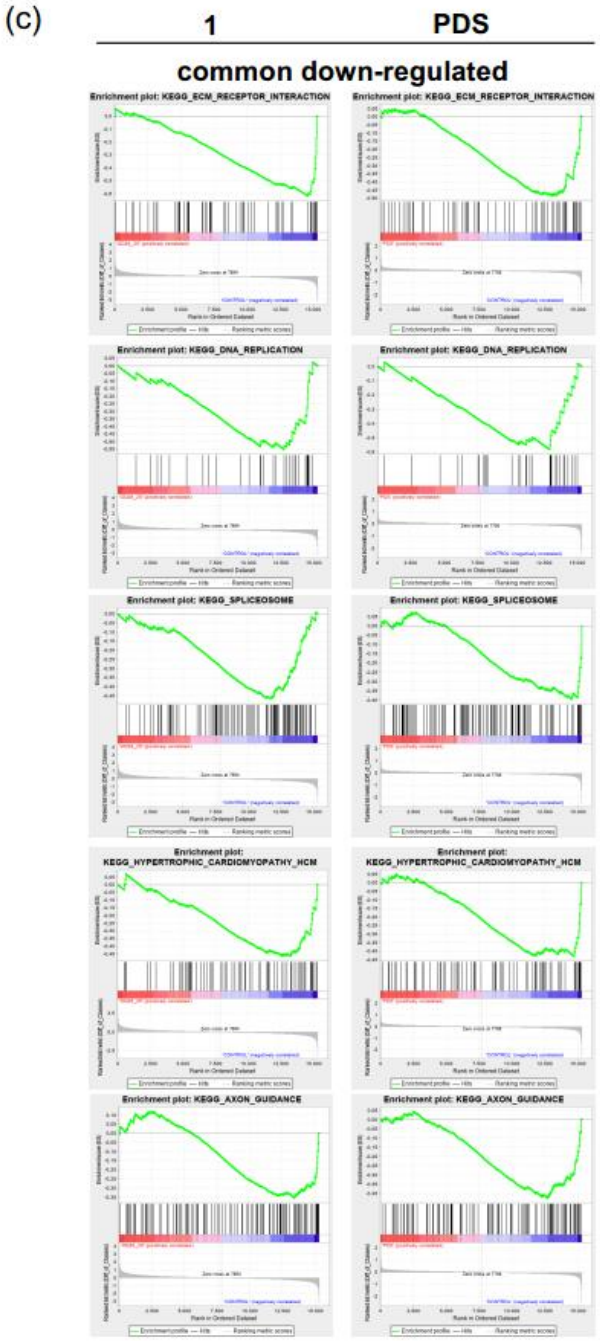

Figure S11. (a) Impact of **1** and PDS (24 h exposure, 25 μM and 15 μM, respectively) on the expression of genes in chromosomal regions enriched for G4 structures as published by Lam et al. (Nat. Commun. 2013, 4, 1796). (b,c) Selection of representative KEGG pathways significantly upregulated (b) or downregulated (c) by **1** and PDS (24 h exposure, 25 μM and 15 μM, respectively). GSEA analyses were performed using http://www.broadinstitute.org/gsea/msigdb/index.jsp

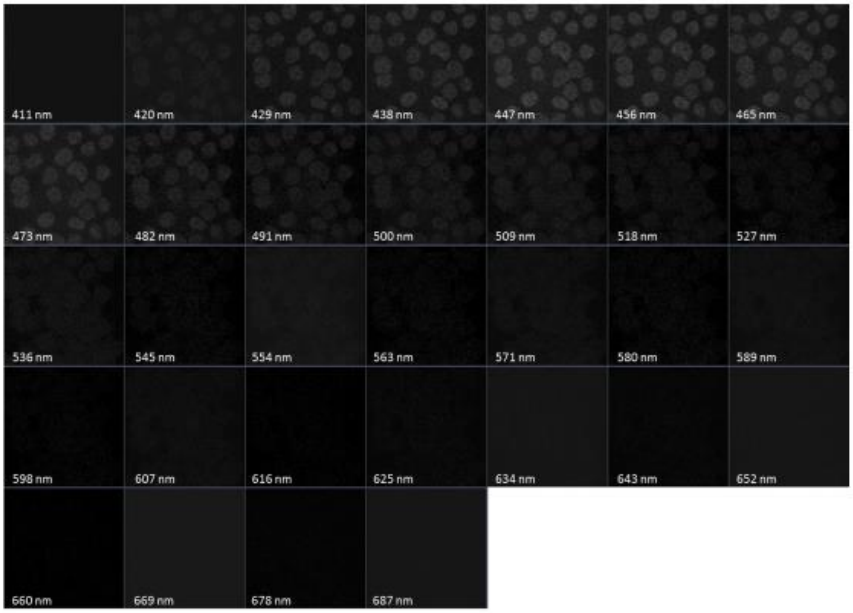

Figure S12. Fluorescence emission fingerprinting of 1. MCF-7 cells treated with 50 µM **1** were employed for the acquisition of a series of *x-y* images with a Zeiss LSM 780 confocal laser scanning microscope and Zen 2.3 SP1 software using a Plan-Apochromat 63×/1.4 NA Oil DIC M27 objective. The emission of **1** was acquired after excitation with 405 nm laser in the range of 411–687 nm and a bandwidth of 9 nm.

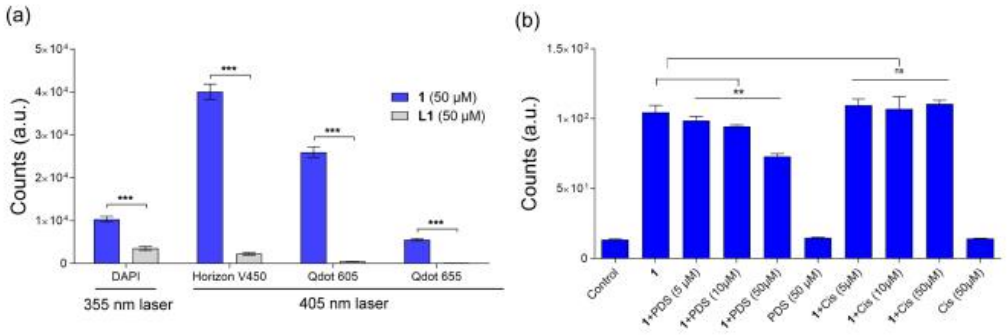

Figure S13. Intracellular fluorescence properties of 1 and L1. (a) Fluorescence intensity after 1h exposure of 50 µM **1** (blue) and **L1** (grey) in viable U2OS cells determined by flow cytometry and normalized to negative control. Emission signals were detected after excitation with the 355 nm laser in the DAPI channel (450/50 nm filter) and after excitation with the 405 nm laser in the Horizon V450 (450/50 nm filter), Qdot 605 (605/12 nm filter) as well as in the Qdot 655 (655/8 nm filter) channel. *** $p \leq 0.001$, DF=4, Student's t-test. (b) Live MCF-7 cells were exposed to 5 µM **1** in combination with the indicated concentrations of either the G-quadruplex stabilizer Pyridostatin (PDS) or the DNA targeting platinum anticancer drug cisplatin (Cis). Cellular fluorescence activity was determined by flow cytometry as under (a). **, $p < 0.01$ by One-way ANOVA with posthoc Bonferroni correction.

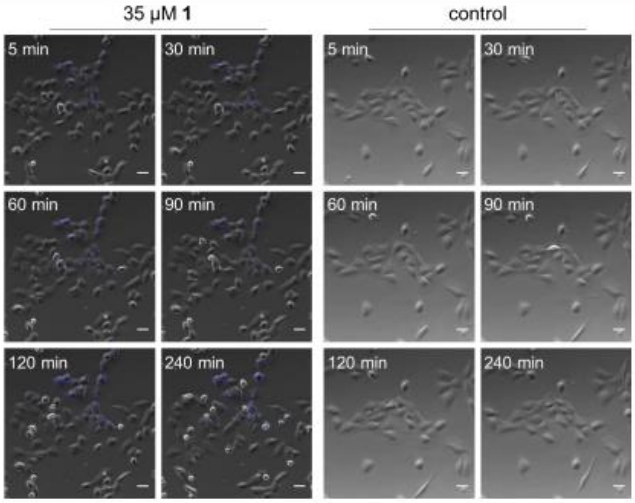

Figure S14. Time-dependent intracellular accumulation of 1. Representative merged images of live cell microscopy showing metallacycle **1** in U2OS cells (λ_{exc} = 395/25nm, λ_{em} = 460/50 nm). Scale bars indicate 25 µm.

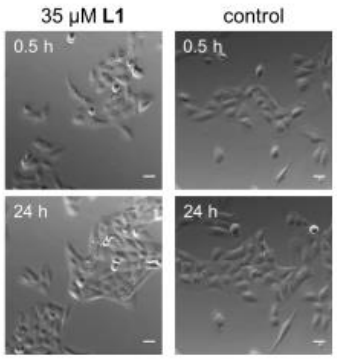

Figure S15. Time-dependent intracellular accumulation of L1. Representative merged images of live cell microscopy of ligand **L1** in U2OS cells (λ_{exc} = 395/25 nm, λ_{em} = 460/50 nm). Scale bars indicate 25 µm.

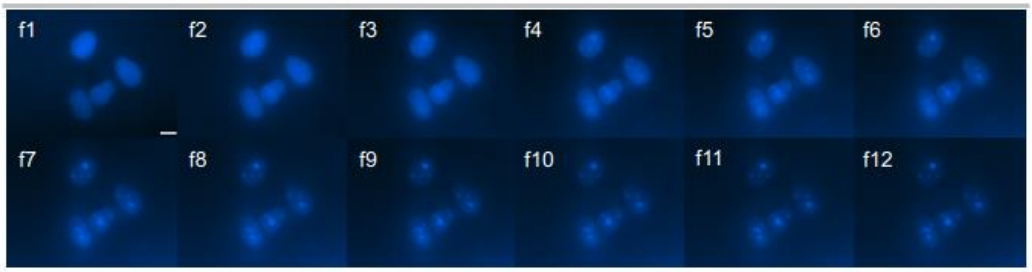

Figure S16. Selective photobleaching of 1-associated nuclear fluorescence. MeOH-fixed U2OS cells were stained with 5 µM **1** for 30 minutes. Fluorescence images were taken on a DMRXA (Leica, Wetzlar, Germany) with a PL APO 100x (1.4 – 0.7) oil objective in time-lapse mode with one frame every 5 seconds at an illumination time of 10 ms and the DAPI filter cube (350/50 excitation, 460/50 emission). Photomicrographs were processed by VisiView software (Visitron Systems, Puchheim, Germany) at Max/Min (range) autoscale settings each. Scale bar indicates 10 µm.

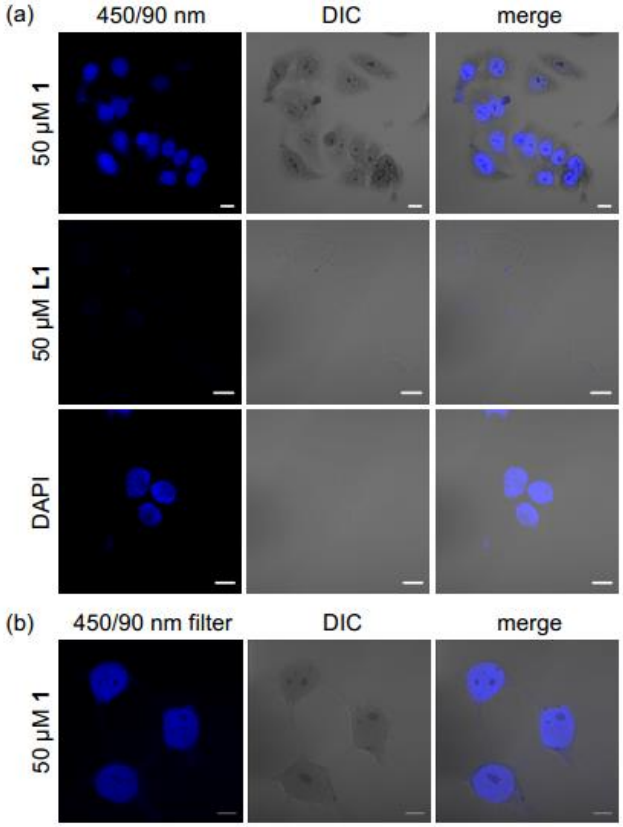

Figure S17. Visualization of 1, L1 and DAPI within PFA fixed cells and of 1 within MeOH fixed cells. (a) Representative images of U2OS cells incubated with 50 µM **1**, 50 µM **L1** or 1 µg/ml DAPI and (b) of MCF-7 cells stained with 50 µM **1** for 30 min. All cells were analyzed with CLSM using the 405 nm laser line and a Plan-Apochromat 63×/1.4 NA Oil DIC M27 objective. Scale bars indicate 10 µm.

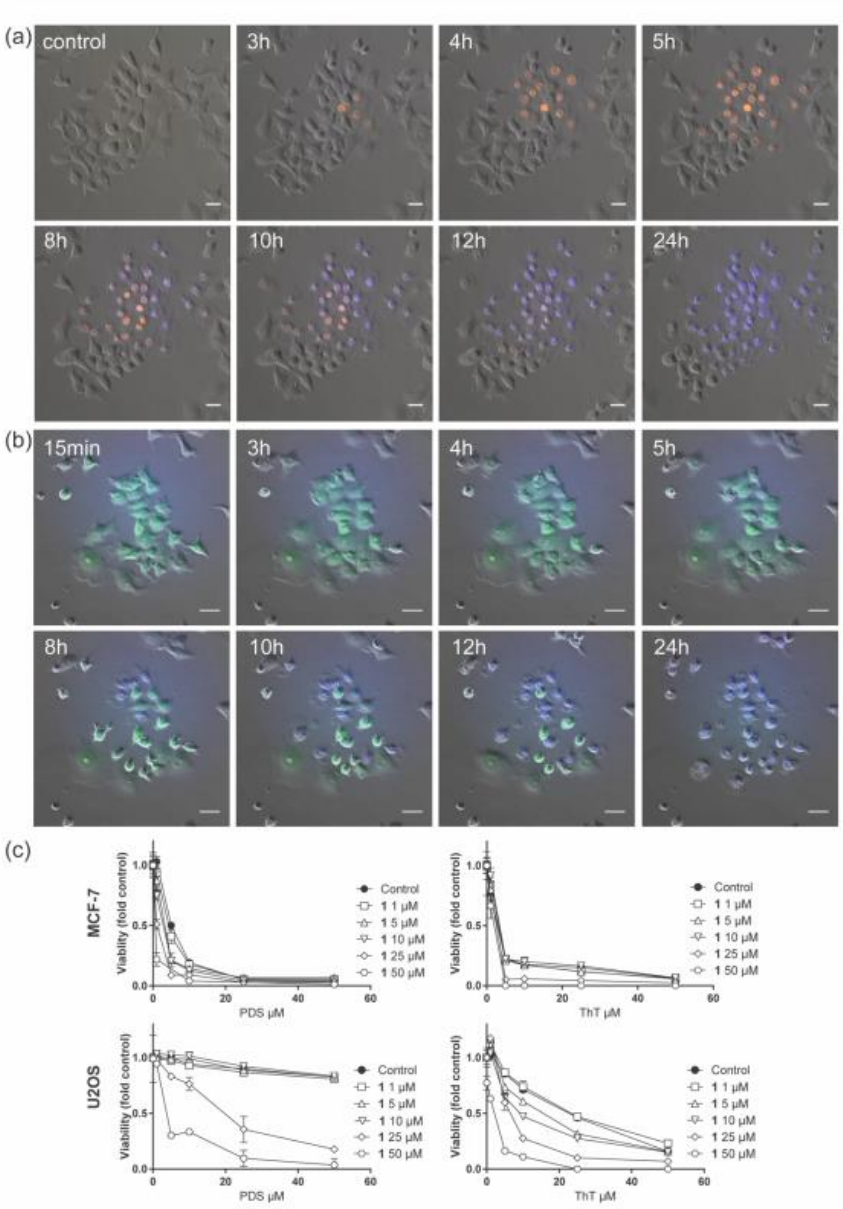

Figure S18. Competition of 1 and TMPyP4 or ThT for the same nuclear target. (a) Representative images of live cell microscopy showing time-dependent intracellular accumulation of TMPyP4 and metallacycle **1** within MCF-7 cells (λ_{exc} = 395/25nm, λ_{em} = 460/50 nm for the blue and λ_{exc} = 560/40nm, λ_{em} = 630/75nm for the red channel). Scale bars indicate 25 μm. See complete live cell competition in Video S1 (58 pictures, one every 30 min). (b) Representative images of live cell microscopy showing intracellular competition of ThT and **1** within U2OS cells. (λ_{exc} = 395/25nm, λ_{em} = 460/50 nm for the blue and λ_{exc} = 475/34, λ_{em} = 525/50 nm for the green channel). Scale bars indicate 10 μm. See complete live cell competition in Video S2 (95 pictures, one every 15 min). (c) **1** exerts synergistic activity with G4-targeting agents ThT and PDS in a 72h co-exposure experiment. Cell viability was determined by MTT assay. To focus on drug interaction effects, data in all curves are depicted normalized to the respective control containing medium (control) or the respective concentrations of **1** as indicated.

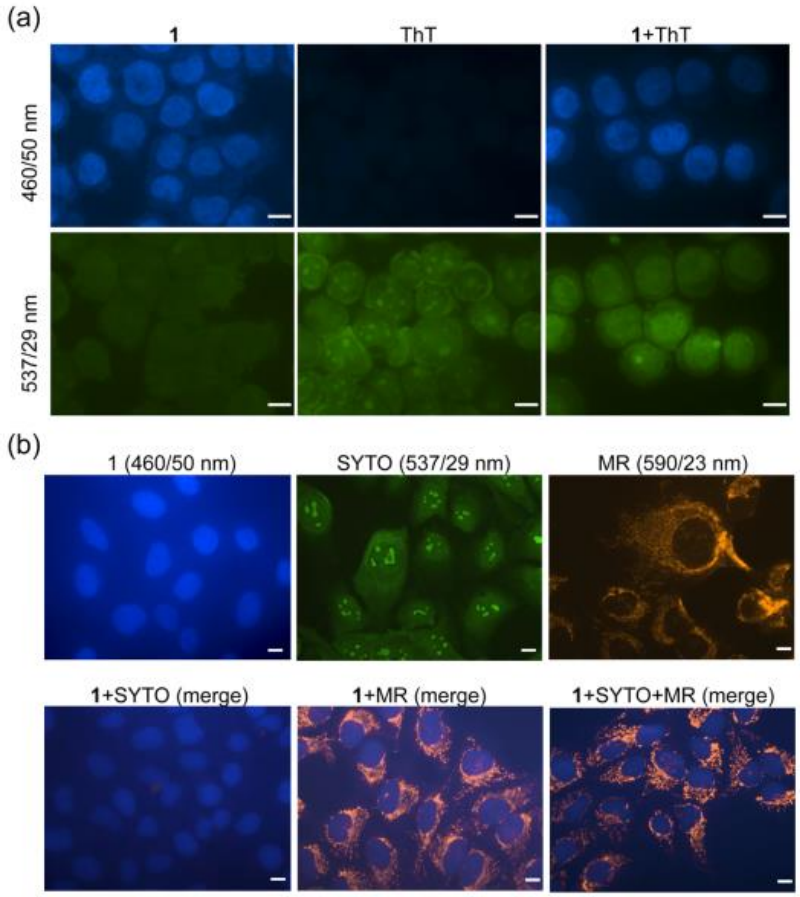

Figure S19. Co-labelling with 1 and ThT, SYTO and MR. (a) MCF7 cells were cytospin prepared, fixed in MeOH (-20°C, 15min) and consequently stained with **1** (5 µM), ThT (5 µM) or a combination of both as indicated. (b) U2OS cells were grown on Ibidi 8-well µ-slides for 24h and then exposed to either SYTO® RNASelect green fluorescence nucleoli dye (SYTO 500 nM; Molecular Probes, Eugene, OR) or MitoTracker® Red CMXRos (MR, 250 nM; Molecular Probes) for 30 min. Then cells were fixed in MeOH (-20°C, 15 min) and stained with **1** (5 µM). Fluorescence images were taken on a DMRXA (Leica, Wetzlar, Germany) with a HCX PL APO 63x (1.32 – 0.6) oil objective using DAPI (λ_{exc} 350/50, λ_{em} 460/50), FITC (λ_{exc} 495/25, λ_{em} 537/29), or Cy3 (λ_{exc} 546/22, λ_{em} 590/23) filter cubes. In (b) acquisition setting were kept identical for the single dye photomicrographs in the upper and the merged pictures in the lower panels. Photomicrographs were processed by VisiView software (Visitron Systems, Puchheim, Germany) in all cases at 14 bit full range settings. Scale bars indicate 10 µm.

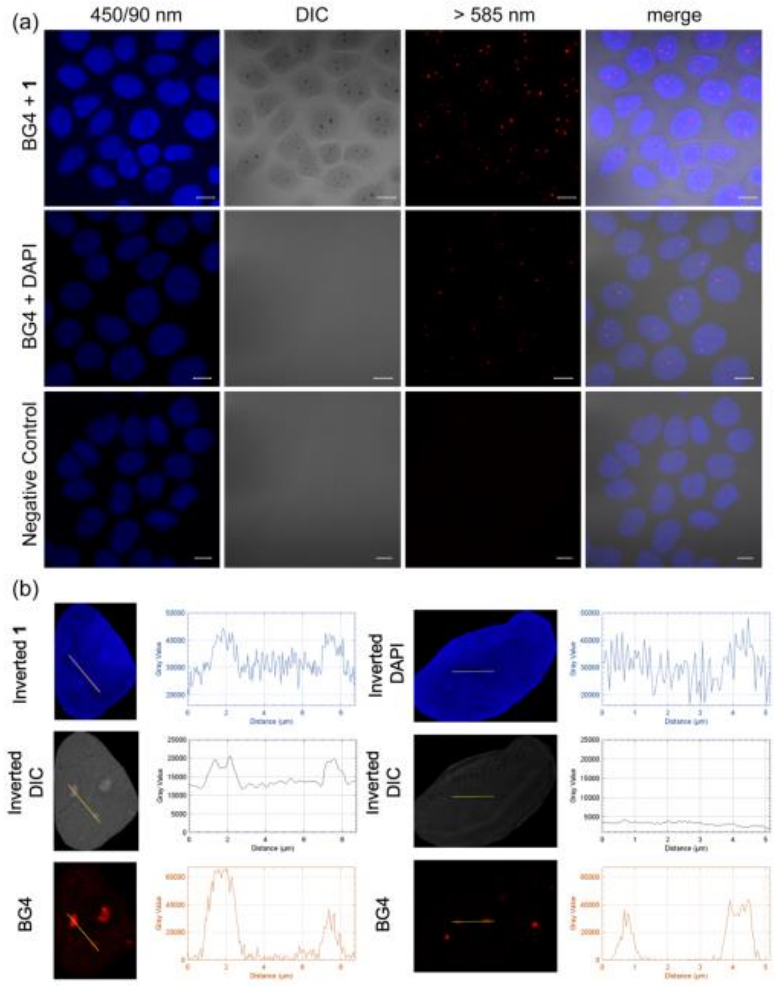

Figure S20. (a) **Colocalization of 1 and BG4**. Representative CLSM images of immunofluorescence staining with BG4 (red) on MeOH fixed MCF-7 cells, counterstained with **1** or DAPI (blue). Scale bars indicate 10 µm. (b) Analysis of spatial correlation of nuclear fluorescence, DIC absorption, and G4-enriched chromatin regions of **1**-treated versus DAPI-stained MCF-7 cells shown in Figure 3a. Two-dimensional pixel intensity plots from the indicated yellow lines in fluorescence and DIC channels of representative cropped nuclei of 1-treated cells (left panel) and DAPI-stained cells (right panel) were generated using the "Plot Profile" analysis tool in ImageJ software. X-axes of intensity plots indicate the distance along respective yellow lines. Y-axes indicate pixel intensities of each channel (16-bit image depth) along respective yellow lines.

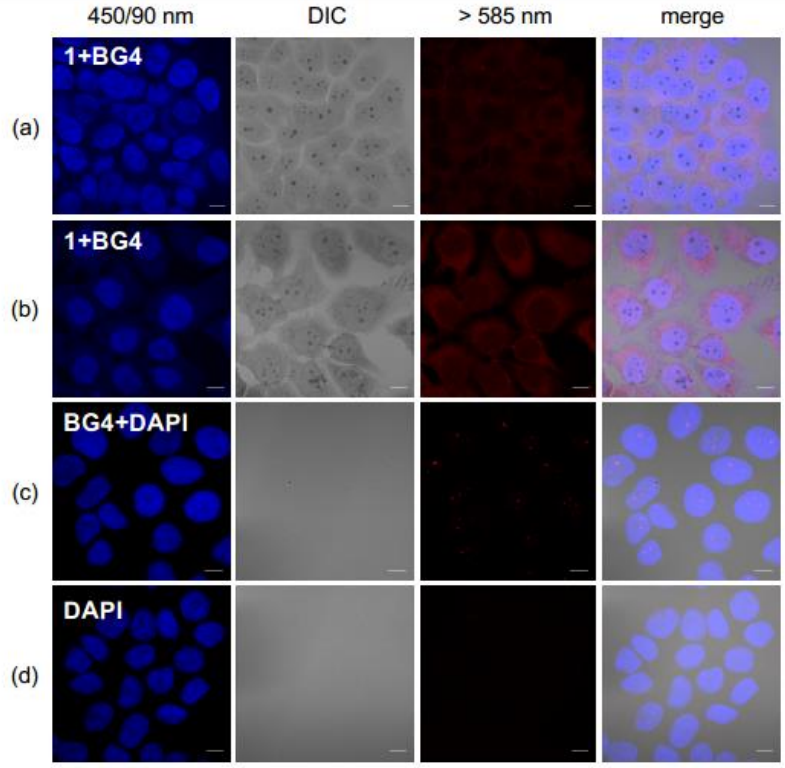

Figure S21. Treatment with 1 disrupts epitope recognition by BG4 in MeOH-fixed cells. (a) MeOH-fixed MCF-7 cells, treated with 50 μM **1** for 30 min followed by BG4 incubation. (b) 50 μM **1** pre-treated MCF-7 cells (1 h), fixed with MeOH and stained with BG4. (c) Confocal microscopy pictures of untreated MCF-7 cells, fixed with MeOH and stained with BG4 (positive control). (d) AF594 negative control. Control pictures are counterstained with DAPI (blue). Scale bars indicate 10 μm.

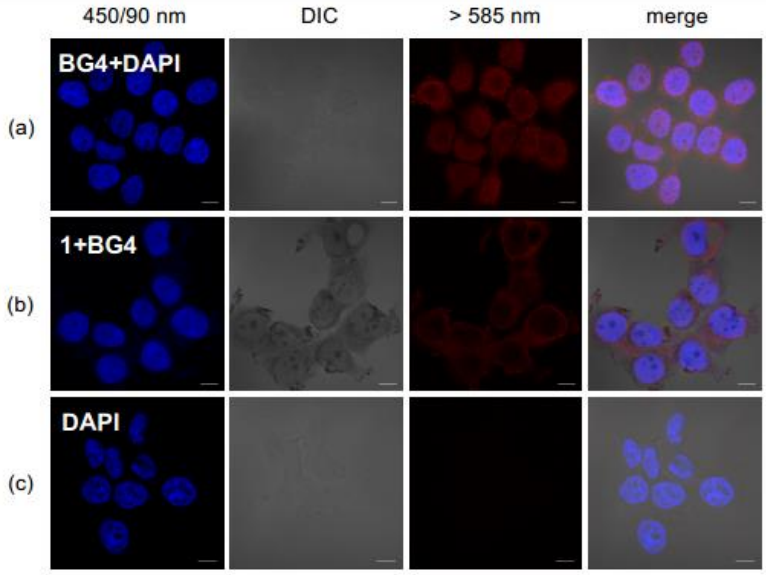

Figure S22. Treatment with 1 disrupts epitope recognition by BG4 in PFA-fixed cells. (a) MCF-7 cells fixed with PFA, incubated with BG4 and counterstained with DAPI showed a nuclear red punctate staining pattern (partially extended to the cytoplasm as previously reported.[15,16] (b) When PFA-fixed MCF-7 cells were treated with metallacycle **1** (50 μM) for 30 min before BG4 incubation, the punctate pattern got diffused, appearing enriched in the cytoplasm. (c) AF594 negative control, counterstained with DAPI. Scale bars indicate 10 μm.

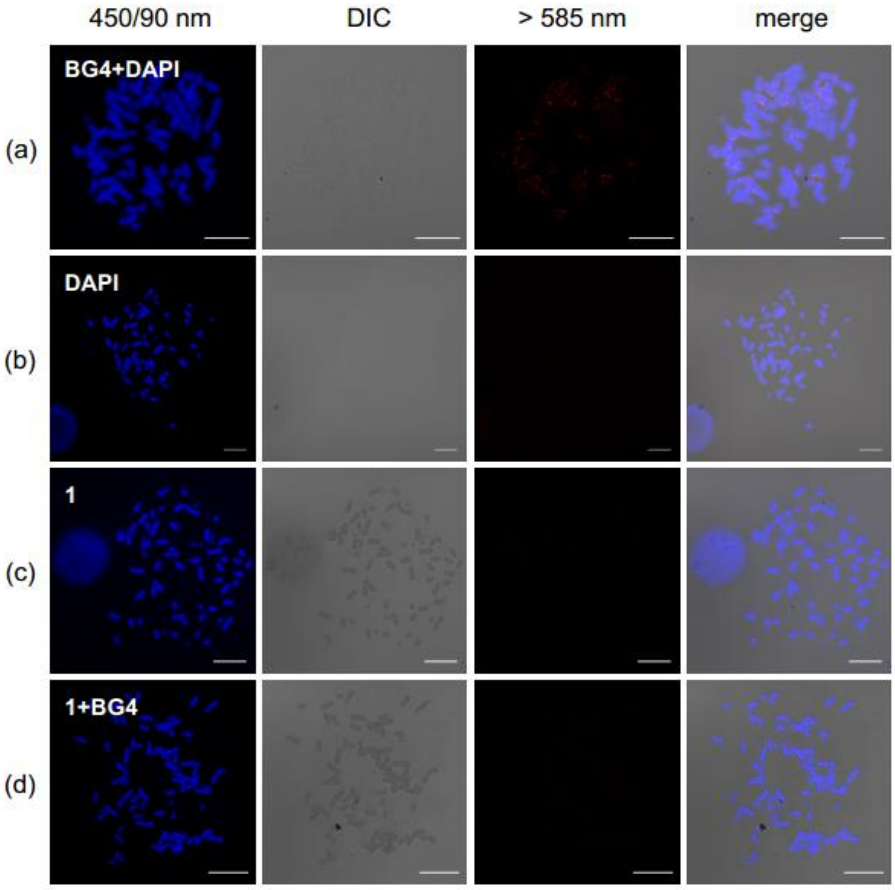

Figure S23. Detection of G-quadruplex structures in metaphase chromosomes of human cancer cells. (a) Representative confocal images of immunofluorescence staining with BG4 (red) and DAPI (blue) on MCF-7 metaphase chromosome spreads. Metaphase chromosomes i immune-stained with BG4 showed distinct red foci at both telomeres and non-telomeric regions, as previously reported).[15] (b) AF594 negative control, counterstained with DAPI. (c) Confocal images of MCF-7 chromosomes stained with 50 μM **1** for 30 minutes. (d) MCF-7 chromosomes treated with 50 μM **1** for 30 min followed by BG4 incubation. Images were acquired using 405 nm excitation laser line and a Plan-Apochromat 63×/1.4 NA Oil DIC M27 objective. Scale bars indicate 10 μm.

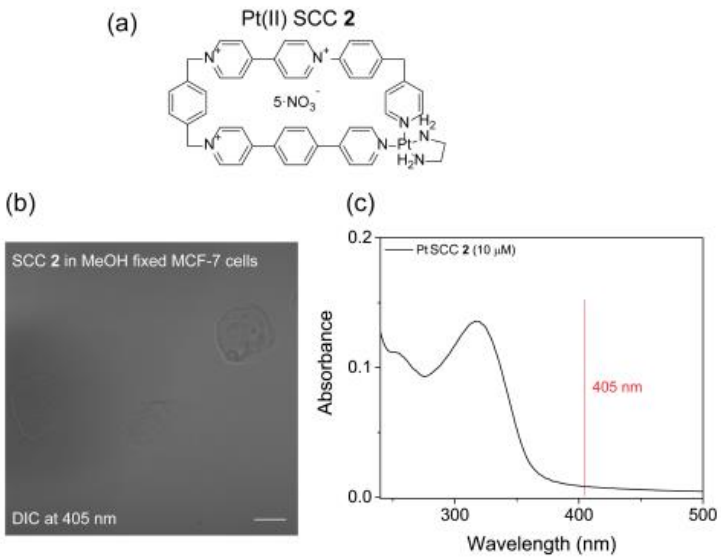

Figure S24. Absorption features of 2 in cell and in solution. (a) Structure of Pt(II) SCC **2**. (b) Bright field image of MeOH fixed MCF-7 cells incubated with Pt-metallacycle **2** acquired using transmitted light DIC mode with the 405 nm laser line and a Plan-Apochromat 63×/1.4 NA Oil DIC M27 objective. (c) UV-Vis absorption spectrum of **2** in Tris-HCl 5 mM, KCl 50 mM, pH=7.8.

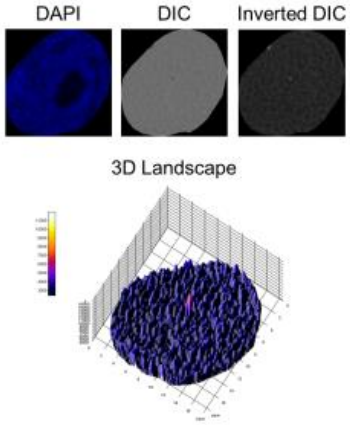

Figure S25. DAPI control experiment in DIC mode. Representative nucleus cropped from confocal image of MCF-7 cells fixed with MeOH and incubated with DAPI and acquired using transmitted light DIC mode at 405 nm. Differences in absorption within subnuclear regions were visualized by three-dimensional surface plotting of single pixel intensities of the inverted DIC image.

References

[1] O. Domarco, I. Neira, T. Rama, A. Blanco-Gómez, M. D. García, C. Peinador, J. M. Quintela, *Org. Biomol. Chem.* **2017**, *15*, 3594–3602.

[2] C. A. Schneider, W. S. Rasband, K. W. Eliceiri, *Nat. Methods* **2012**, *9*, 671–675.

[3] D. Renčiuk, J.-L. Mergny, A. Guédin, J. Zhou, L. Beaurepaire, A. Bourdoncle, *Methods* **2012**, *57*, 122–128.

[4] O. Trott, A. J. Olson, *J. Comput. Chem.* **2010**, *31*, 455–61.

[5] A. D. Becke, *J. Chem. Phys.* **1993**, *98*, 5648–5652.

[6] C. Lee, W. Yang, R. G. Parr, *Phys. Rev. B* **1988**, *37*, 785–789.

[7] P. J. Stephens, F. J. Devlin, C. F. Chabalowski, M. J. Frisch, *J. Phys. Chem.* **1994**, *98*, 11623–11627.

[8] P. J. Hay, W. R. Wadt, *J. Chem. Phys.* **1985**, *82*, 270–283.

[9] P. C. Hariharan, J. A. Pople, *Theor. Chim. Acta* **1973**, *28*, 213–222.

[10] M. M. Francl, *J. Chem. Phys.* **1982**, *77*, 3654–3665.

[11] M. J. Frisch, G. W. Trucks, H. B. Schlegel, G. E. Scuseria, M. A. Robb, J. R. Cheeseman, G. Scalmani, V. Barone, B. Mennucci, G. A. Petersson, et al., *Gaussian Inc Wallingford CT* **2009**, *34*, Wallingford CT.

[12] G. M. Morris, R. Huey, W. Lindstrom, M. F. Sanner, R. K. Belew, D. S. Goodsell, A. J. Olson, *J. Comput. Chem.* **2009**, *30*, 2785–2791.

[13] E. F. Pettersen, T. D. Goddard, C. C. Huang, G. S. Couch, D. M. Greenblatt, E. C. Meng, T. E. Ferrin, *J. Comput. Chem.* **2004**, *25*, 1605–1612.

[14] C. Pirker, K. Holzmann, S. Spiegl-Kreinecker, L. Elbling, C. Thallinger, H. Pehamberger, M. Micksche, W. Berger, *Melanoma Res.* **2003**, *13*, 483–492.

[15] G. Biffi, D. Tannahill, J. McCafferty, S. Balasubramanian, *Nat. Chem.* **2013**, *5*, 182–186.

[16] G. Biffi, M. Di Antonio, D. Tannahill, S. Balasubramanian, *Nat. Chem.* **2014**, *6*, 75–80.

[17] V. Mathieu, C. Pirker, W. M. Schmidt, S. Spiegl-Kreinecker, D. Lötsch, P. Heffeter, B. Hegedus, M. Grusch, R. Kiss, W. Berger, *Oncotarget* **2012**, *3*, 399–413.

[18] E. Puujalka, M. Heinz, B. Hoesel, P. Friedl, B. Schweighofer, J. Wenzina, C. Pirker, J. A. Schmid, R. Loewe, E. F. Wagner, et al., *J. Invest. Dermatol.* **2016**, *136*, 967–977.

[19] E. Y. N. Lam, D. Beraldi, D. Tannahill, S. Balasubramanian, *Nat. Commun.* **2013**, *4*, 1796.

[20] V. Mathieu, C. Pirker, W. M. Schmidt, S. Spiegl-Kreinecker, D. Lötsch, P. Heffeter, B. Hegedus, M. Grusch, R. Kiss, W. Berger, *Oncotarget* **2012**, *3*, 399–413.

[21] J. Dai, C. Punchihewa, A. Ambrus, D. Chen, R. A. Jones, D. Yang, *Nucleic Acids Res.* **2007**, *35*, 2440–2450.

[22] J. M. Nicoludis, S. P. Barrett, J. L. Mergny, L. A. Yatsunyk, *Nucleic Acids Res.* **2012**, *40*, 5432–5447.

[23] S. T. D. Hsu, P. Varnai, A. Bugaut, A. P. Reszka, S. Neidle, S. Balasubramanian, *J. Am. Chem. Soc.* **2009**, *131*, 13399–13409.

[24] S. M. L. Palumbo, S. W. Ebbinghaus, L. H. Hurley, *J. Am. Chem. Soc.* **2009**, *131*, 10878–10891.

[25] A. T. Phan, V. Kuryavyi, S. Burge, S. Neidle, D. J. Patel, *J. Am. Chem. Soc.* **2007**, *129*, 4386–4392.

[26] P. Thordarson, *Chem. Soc. Rev.* **2011**, *40*, 1305–1323.

[27] E. Rajczak, V. L. Pecoraro, B. Juskowiak, *Metallomics* **2017**, *9*, 1735–1744.

Author Contributions

A.T., W.B. and C.P. conceived and directed the study in all its parts. O.D. and M.D.G. performed the synthesis and the structural characterization of the metallacycle. O.D. and A.T. carried out all the measurements in solution. C.K, C.P. and C.D. performed the in-cell studies including cell viability and clonogenic assays, flow cytometry, live cell microscopy and CLSM. B.E., J.R. and G.T. analysed live cell microscopy and CLSM data. A.T., W.B., C.P. and B.K.K. analysed and interpreted the overall results. All the authors contributed to the final version of the manuscript.

List of Figures

List of Tables

Abbreviations

°C	Degree Celsius
µl	Microliter
A	Adenosine
AB	Antibody
ABC	ATP Binding Cassette
AFM	Atomic Force Microscopy
Akt	Protein Kinase B
ALT	Alternative Lengthening of Telomeres
ATCC	American Type Culture Collection
ATM	Ataxia-Telangiectasia Mutated
ATR	ATM- and Rad3-Related
Bcl-XL	B-cell lymphoma-extra large
BFB	Breakage-Fusion-Bridge
C	Cytosine
c-Abl	Abelson Tyrosine Kinase
CAF	Cancer Associated Fibroblast
CD	Circular Dichroism
cDNA	Complementary DNA
CLSM	Confocal Laser Scanning Microscopy
cm	Centimeter
CO2	Carbon Dioxide
cRNA	Complementary RNA
CTR1	Copper Transporter-1
CX-3543	Quarfloxin
Cy	Cyanine
DACH	Diaminocyclohexane
DAPI	4’,6-diamidino-2-phenylindole
ddH2O	Double-Distilled Water
DDR	DNA Damage Response
DHFR	Dihydrofolate Reductase
DIC	Differential Interference Contrast
D-loop	Displacement Loop
DMEM	Dulbecco’s Modifies Eagle’s Medium
DNA	Deoxyribonucleic Acid
ds	Double-Stranded
DSB	Double Strand Break
dsRNA	Double-Stranded RNA
e.g.	Exempli Gratia
EDTA	Ethylenediaminetetraacetic Acid
EGFR	Epidermal Growth Factor Receptor
ERK	Extracellular-Signal Regulated Kinase
ESI-MS	Electrospray Ionization Mass Spectrometry
EtOH	Ethanol

FACS	Fluorescence-Activated Cell Sorting
FAM	Fluorescein
FBS	Fetal Bovine Serum
FDA	U.S. Food and Drug Administration
FITC	Fluorescein Isothiocyanate
FLIP	FLICE-like inhibitory protein
FRET	Fluorescence Resonance Energy Transfer
G	Guanine
g	Gram or Gravitational Force
G4	G-Quadruplex
GIR	Global Info Research
GO	Gene Ontology
GSEA	Gene Set Enrichment Analysis
h	Hour
H2O	Water
HCl	Hydrogen Chloride
HEPES	4-(2-hydroxyethyl)-1-piperazineethanesulfonic Acid
HR	Homologous Recombination
hTERT	Human Telomerase Reverse Transcriptase
hTR / hTERC	Human Telomerase RNA
i.a.	Inter Alia
IC50	Half Maximal Inhibitory Concentration
ICR	Institute for Cancer Research
IF	Immunofluorescence
IMDM	Iscove's Modified Dulbecco's Medium
JNK	c-Jun N-terminal Kinases
KCl	Potassium Chloride
l	Liter
LED	Light-Emitting Diode
MAPK	Mitogen-Activated Protein Kinase
MAZ	Myc-Associated Zinc Finger Protein
MeAc	Methanol Acetone
MeOH	Methanol
min	Minute
ml	Milliliter
MMLV-RT	Moloney Murine Leukemia Virus Reverse Transcriptase
MMR	Mismatch Repair
MNP	Modified Eagle's Medium supplemented with 0.2% Na-pyruvate and 1% non-essential amino acid
MOPS	3-(N-morpholino)propanesulfonic Acid
mRNA	Messenger RNA
MTT	3-(4,5-dimethylthiazol-2-yl)-2,5-diphenyltetrazolium
NaCl	Sodium Chloride
NER	Nucleotide Excision Repair
NGS	Normal Goat Serum
NHEJ	Nonhomologous End-Joining
nm	Nanometer
NMR	Nuclear Magnetic Resonance

NSCLC	Non-Small-Cell Lung Carcinoma
o/n	Overnight
PARP	Poly ADP-Ribose Polymerase
PBS	Phosphate-Buffered Saline
PDS	Pyridostatin
PFA	Paraformaldehyde
PI	Propidium Iodide
PI3	Phosphoinositide 3
PMT	Photomultiplier Tube
POT1	Protection of Telomeres Protein 1
PQS	Putative Quadruplex Sequence
Pt	Platinum
PTEN	Phosphatase And Tensin Homolog
QC	Quality Control
RAP1	Ras-Related Protein 1
rDNA	Ribosomal DNA
RIN	RNA Integrity Number
RNA	Ribonucleic Acid
RNAP II	RNA-Polymerase II
ROS	Reactive Oxygen Species
RPMI	Roswell Park Memorial Institute
rRNA	Ribosomal Ribonucleic Acid
RT	Room Temperature
SCC	Supramolecular Coordination Complex
SP1	Specificity Protein 1
SPR	Surface Plasmon Resonance
ss	Single-Stranded
SSB	Single Strand Break
SSC	Side Scatter
T	Thymidine
T/E	Trypsin-Ethylenediaminetetraacetic Acid
TAMRA	Tetramethylrhodamine
TCAB1	Telomerase CAjal Body Protein 1
ThT	Thioflavin T
TIN2	TRF1-Interacting Nuclear Factor 2
TKI	Tyrosine Kinase Inhibitor
t-loop	Telomeric Loop
TME	Tumor Microenvironment
TMM	Telomere Maintenance Mechanism
TMPyP4	5,10,15,20-tetra(N-methyl-4-pyridyl)porphyrin
T-PMT	Transmitted Light Detector
TPP1	POT1- and TIN2-Organizing Protein
TSS	Transcription Start Site
UTR	Untranslated Region
UV-Vis	UV-Visible Spectroscopy
VM	Vienna Melanoma

Literature

[1] F. Bray, J. Ferlay, I. Soerjomataram, R.L. Siegel, L.A. Torre, A. Jemal, Global cancer statistics 2018: GLOBOCAN estimates of incidence and mortality worldwide for 36 cancers in 185 countries, CA. Cancer J. Clin. 68 (2018) 394–424. doi:10.3322/caac.21492.

[2] World Health Organisation, Latest global cancer data: Cancer burden rises to 18.1 million new cases and 9.6 million cancer deaths in 2018, Int. Agency Res. Cancer. 263 (2018) 13–15. http://gco.iarc.fr/,.

[3] World Health Organisation, Global cancer data, Int. Agency Res. Cancer. (2018) 13–15. http://gco.iarc.fr/,.

[4] J. Klotz, M. Hackl, M. Schwab, A. Hanika, D. Haluza, Combining population projections with quasilikelihood models: A new way to predict cancer incidence and cancer mortality in Austria up to 2030, Demogr. Res. 40 (2019) 503–532. doi:10.4054/DEMRES.2019.40.19.

[5] World Health Organization, Cancer, (2018). https://www.who.int/en/news-room/fact-sheets/detail/cancer (accessed September 3, 2019).

[6] C.L. Chaffer, R.A. Weinberg, A Perspective on Cancer Cell Metastasis, Science (80-.). 331 (2011) 1559–1564. doi:10.1126/science.1203543.

[7] P Uma Devi, Basics of Carcinogenesis, Heal. Adm. XVII (2000) 16–24. http://medind.nic.in/haa/t05/i1/haat05i1p16.pdf.

[8] R.A. Weinberg, The Biology of Cancer, 2014. doi:10.1017/CBO9781107415324.004.

[9] M. Greaves, C.C. Maley, Clonal Evolution in Cancer, Nature. 481 (2012) 306. doi:10.1038/NATURE10762.

[10] B. Alberts, A. Johnson, J. Lewis, D. Morgan, M. Raff, K. Roberts, P. Walter, Molecular biology of the cell, 6th edition, 2014.

[11] A.E. Denton, E.W. Roberts, D.T. Fearon, Stromal Cells in the Tumor Microenvironment, in: Adv. Exp. Med. Biol., 2018: pp. 99–114. doi:10.1007/978-3-319-78127-3_6.

[12] M. Wang, J. Zhao, L. Zhang, F. Wei, Y. Lian, Y. Wu, Z. Gong, S. Zhang, J. Zhou, K. Cao, X. Li, W. Xiong, G. Li, Z. Zeng, C. Guo, Role of tumor microenvironment in tumorigenesis, J. Cancer. 8 (2017) 761–773. doi:10.7150/jca.17648.

[13] C. Belli, D. Trapani, G. Viale, P. D'Amico, B.A. Duso, P. Della Vigna, F. Orsi, G. Curigliano, Targeting the microenvironment in solid tumors, Cancer Treat. Rev. 65 (2018) 22–32. doi:10.1016/j.ctrv.2018.02.004.

[14] G. Lorusso, C. Rüegg, The tumor microenvironment and its contribution to tumor evolution toward metastasis, Histochem. Cell Biol. 130 (2008) 1091–1103. doi:10.1007/s00418-008-0530-8.

[15] S. Guo, C.-X. Deng, Effect of Stromal Cells in Tumor Microenvironment on Metastasis Initiation, Int. J. Biol. Sci. 14 (2018) 2083–2093. doi:10.7150/ijbs.25720.

[16] K. Kessenbrock, V. Plaks, Z. Werb, Matrix metalloproteinases: regulators of the tumor microenvironment., Cell. 141 (2010) 52–67. doi:10.1016/j.cell.2010.03.015.

[17] D. Hanahan, R.A. Weinberg, The hallmarks of cancer., Cell. 100 (2000) 57–70. doi:10.1016/s0092-8674(00)81683-9.

[18] Y.A. Fouad, C. Aanei, Revisiting the hallmarks of cancer, Am. J. Cancer Res. 7 (2017) 1016–1036.

[19] S. Negrini, V.G. Gorgoulis, T.D. Halazonetis, Genomic instability — an evolving hallmark of cancer, Nat. Rev. Mol. Cell Biol. 11 (2010) 220–228. doi:10.1038/nrm2858.

[20] K. Pietras, A. Östman, Hallmarks of cancer: Interactions with the tumor stroma, Exp. Cell Res. 316 (2010) 1324–1331. doi:10.1016/j.yexcr.2010.02.045.

[21] Y. Lazebnik, What are the hallmarks of cancer?, Nat. Rev. Cancer. 10 (2010) 232–233. doi:10.1038/nrc2827.

[22] D. Hanahan, R.A. Weinberg, Hallmarks of cancer: The next generation, Cell. 144 (2011) 646–674. doi:10.1016/j.cell.2011.02.013.

[23] M.C. White, D.M. Holman, J.E. Boehm, L.A. Peipins, M. Grossman, S.J. Henley, Age and Cancer Risk: A Potentially Modifiable Relationship, Am. J. Prev. Med. 46 (2014) S7. doi:10.1016/J.AMEPRE.2013.10.029.

[24] S. Wu, W. Zhu, P. Thompson, Y.A. Hannun, Evaluating intrinsic and non-intrinsic cancer risk factors, Nat. Commun. 9 (2018) 3490. doi:10.1038/s41467-018-05467-z.

[25] Y.J. Ko, S.P. Balk, Targeting steroid hormone receptor pathways in the treatment of hormone dependent cancers., Curr. Pharm. Biotechnol. 5 (2004) 459–70. http://www.ncbi.nlm.nih.gov/pubmed/15544494 (accessed September 4, 2019).

[26] V.A. Katzke, R. Kaaks, T. Kühn, Lifestyle and cancer risk, Cancer J. (United States). 21 (2015) 104–110. doi:10.1097/PPO.0000000000000101.

[27] A. V. Lichtenstein, Cancer: Bad luck or punishment?, Biochem. 82 (2017) 75–80. doi:10.1134/S0006297917010084.

[28] What Is Cancer? - National Cancer Institute, (n.d.). https://www.cancer.gov/about-cancer/understanding/what-is-cancer (accessed September 3, 2019).

[29] Types of cancer | Cancer Research UK, (n.d.). https://www.cancerresearchuk.org/what-is-cancer/how-cancer-starts/types-of-cancer (accessed September 3, 2019).

[30] What Are Basal and Squamous Cell Skin Cancers?, (n.d.). https://www.cancer.org/cancer/basal-and-squamous-cell-skin-cancer/about/what-is-basal-and-squamous-cell.html (accessed September 3, 2019).

[31] C. Janeway, P. Travers, M. Walport, M. Shlomchik, Immunobiology, 5th edition, Garland Pub, 2001. https://www.ncbi.nlm.nih.gov/books/NBK10757/ (accessed September 3, 2019).

[32] R. Küppers, M.L. Hansmann, The Hodgkin and Reed/Sternberg cell, Int. J. Biochem. Cell Biol. 37 (2005) 511–517. doi:10.1016/j.biocel.2003.10.025.

[33] M. MacGill, Blastoma: Causes, types, diagnosis, and treatment, (n.d.). https://www.medicalnewstoday.com/articles/301456.php (accessed September 3, 2019).

[34] Z. Abbas, S. Rehman, An Overview of Cancer Treatment Modalities, Intech. (2018). doi:http://dx.doi.org/10.5772/57353.

[35] Types of Cancer Treatment | American Cancer Society, (n.d.). https://www.cancer.org/treatment/treatments-and-side-effects/treatment-types.html (accessed May 30, 2019).

[36] H.B. Othersen, Ephraim McDowell: the qualities of a good surgeon., Ann. Surg. 239 (2004) 648–650. doi:10.1097/01.sla.0000124382.04128.5a.

[37] W.S. Halsted, The Results of Operations for the Cure of Cancer of the Breast Performed at the Johns Hopkins Hospital from June, 1889, to January, 1894, Ann. Surg. 20 (1894) 497–555.

[38] V.T. DeVita, S.A. Rosenberg, Two Hundred Years of Cancer Research, N. Engl. J. Med. 366 (2012) 2207–2214. doi:10.1056/NEJMra1204479.

[39] G.H. Sakorafas, M. Safioleas, Breast cancer surgery: An historical narrative. Part II. 18th and 19th centuries, Eur. J. Cancer Care (Engl). 19 (2010) 6–29. doi:10.1111/j.1365-2354.2008.01060.x.

[40] H. (Jack) West, J.O. Jin, Adjuvant Therapy, JAMA Oncol. 1 (2015) 698. doi:10.1001/jamaoncol.2015.2095.

[41] A.K. Bryant, M.P. Banegas, M.E. Martinez, L.K. Mell, J.D. Murphy, Trends in Radiation Therapy among Cancer Survivors in the United States, 2000-2030., Cancer Epidemiol. Biomarkers Prev. 26 (2017) 963–970. doi:10.1158/1055-9965.EPI-16-1023.

[42] K. Haume, S. Rosa, S. Grellet, M.A. Śmiałek, K.T. Butterworth, A. V Solov'yov, K.M. Prise, J. Golding, N.J. Mason, Gold nanoparticles for cancer radiotherapy: a review., Cancer Nanotechnol. 7 (2016) 8. doi:10.1186/s12645-016-0021-x.

[43] R. Baskar, J. Dai, N. Wenlong, R. Yeo, K.-W. Yeoh, Biological response of cancer cells to radiation treatment., Front. Mol. Biosci. 1 (2014) 24. doi:10.3389/fmolb.2014.00024.

[44] E.J. Moding, M.B. Kastan, D.G. Kirsch, Strategies for optimizing the response of cancer and normal tissues to radiation., Nat. Rev. Drug Discov. 12 (2013) 526–42. doi:10.1038/nrd4003.

[45] H. Gelband, P. Jha, R. Sankaranarayanan, S. Horton, Cancer: Disease Control Priorities, Third Edition (Volume 3)., The International Bank for Reconstruction and Development / The World Bank, 2015. doi:10.1596/978-1-4648-0349-9_CH14.

[46] G.C. Barnett, C.M.L. West, A.M. Dunning, R.M. Elliott, C.E. Coles, P.D.P. Pharoah, N.G. Burnet, Normal tissue reactions to radiotherapy: towards tailoring treatment dose by genotype., Nat. Rev. Cancer. 9 (2009) 134–42. doi:10.1038/nrc2587.

[47] A. Fairchild, S.H. Tirumani, M.H. Rosenthal, S.A. Howard, K.M. Krajewski, M. Nishino, A.B. Shinagare, J.P. Jagannathan, N.H. Ramaiya, Hormonal therapy in oncology: A primer for the radiologist, Am. J. Roentgenol. 204 (2015) W620–W630. doi:10.2214/AJR.14.13604.

[48] Side effects of hormone therapy | Cancer Research UK, (n.d.). https://www.cancerresearchuk.org/about-cancer/cancer-in-general/treatment/hormone-therapy/side-effects-women (accessed September 5, 2019).

[49] A. Garrett, M.A. Quinn, Hormonal therapies and gynaecological cancers, Best Pract. Res. Clin. Obstet. Gynaecol. 22 (2008) 407–421. doi:10.1016/j.bpobgyn.2007.08.003.

[50] Common Side Effects of Eulexin (Flutamide) Drug Center - RxList, (n.d.). https://www.rxlist.com/eulexin-side-effects-drug-center.htm#overview (accessed September 5, 2019).

[51] N.E. Papaioannou, O. V. Beniata, P. Vitsos, O. Tsitsilonis, P. Samara, Harnessing the immune system to improve cancer therapy, Ann. Transl. Med. 4 (2016). doi:10.21037/atm.2016.04.01.

[52] J. Couzin-Frankel, Breakthrough of the year 2013. Cancer immunotherapy., Science. 342 (2013) 1432–3. doi:10.1126/science.342.6165.1432.

[53] D. Baxter, Active and passive immunization for cancer., Hum. Vaccin. Immunother. 10 (2014) 2123–9. doi:10.4161/hv.29604.

[54] T.N. Schumacher, R.D. Schreiber, Neoantigens in cancer immunotherapy, Science (80-.). 348 (2015) 69–74. doi:10.1126/science.aaa4971.

[55] M. Sambi, L. Bagheri, M.R. Szewczuk, Current challenges in cancer immunotherapy: Multimodal approaches to improve efficacy and patient response rates, J. Oncol. 2019 (2019). doi:10.1155/2019/4508794.

[56] C. Lee Ventola, Cancer immunotherapy, part 3: Challenges and future trends, P T. 42 (2017) 514–521.

[57] V.V. Padma, An overview of targeted cancer therapy., BioMedicine. 5 (2015) 19. doi:10.7603/s40681-015-0019-4.

[58] E. Pérez-Herrero, A. Fernández-Medarde, Advanced targeted therapies in cancer: Drug nanocarriers, the future of chemotherapy, Eur. J. Pharm. Biopharm. 93 (2015) 52–79. doi:10.1016/j.ejpb.2015.03.018.

[59] R.J. Kreitman, Immunotoxins for targeted cancer therapy, AAPS J. 8 (2006) E532. doi:10.1208/AAPSJ080363.

[60] L. Yan, N. Rosen, C. Arteaga, Targeted cancer therapies., Chin. J. Cancer. 30 (2011) 1–4. doi:10.5732/CJC.010.10553.

[61] D.J.L. Wong, A. Ribas, Targeted Therapy for Melanoma, Cancer Treat. Res. 167 (2016) 251–262. doi:10.1007/978-3-319-22539-5_10.

[62] T. Le, D.E. Gerber, Newer-Generation EGFR Inhibitors in Lung Cancer: How Are They Best Used?, Cancers (Basel). 11 (2019). doi:10.3390/cancers11030366.

[63] Chemotherapy - Mayo Clinic, (n.d.). https://www.mayoclinic.org/tests-procedures/chemotherapy/about/pac-20385033 (accessed September 6, 2019).

[64] How Is Chemotherapy Given?, (n.d.). http://chemocare.com/chemotherapy/what-is-chemotherapy/how-chemotherapy-is-given.aspx (accessed September 6, 2019).

[65] J.D. Watson, F.H.C. Crick, A structure for deoxyribose nucleic acids, Nature. 171 (1953) 737–738.

[66] K. Gurova, New hopes from old drugs: revisiting DNA-binding small molecules as anticancer agents, Futur. Oncol. 5 (2009) 1685–1704.

[67] Atta-ur-Rahman, I.M. Choudhary, Frontiers in Drug Design & Discovery: Volume 9 - Google Books, 2018. https://books.google.at/books?id=NoJoDwAAQBAJ&pg=PA60&lpg=PA60&dq=antimetabolites+incorporation+of+chemically+altered+nucleotide&source=bl&ots=YsYf9ylHx1&sig=ACfU3U2wU2dOtZDGPzqt-4dkwgPNQ7Ayfw&hl=en&sa=X&ved=2ahUKEwiAnobF453jAhVIwqYKHU6_AFYQ6AEwD3oECAkQAQ (accessed July 5, 2019).

[68] H. Tian, B. Cronstein, Understanding the Mechanisms of Action of Methotrexate, Bull. NYU Hosp. Jt. Dis. 65 (2007) 168–173.

[69] N.J. Wheate, C.R. Brodie, J.G. Collins, S. Kemp, J.R. Aldrich-wright, DNA Intercalators in Cancer Therapy: Organic and Inorganic Drugs and Their Spectroscopic Tools of Analysis, Mini-Reviews Med. Chem. 7 (2007) 627–648.

[70] L.H. Swift, R.M. Golsteyn, Genotoxic anti-cancer agents and their relationship to DNA damage, mitosis, and checkpoint adaptation in proliferating cancer cells, Int. J. Mol. Sci. 15 (2014) 3403–3431. doi:10.3390/ijms15033403.

[71] K. Cheung-Ong, G. Giaever, C. Nislow, DNA-damaging agents in cancer chemotherapy: Serendipity and chemical biology, Chem. Biol. 20 (2013) 648–659. doi:10.1016/j.chembiol.2013.04.007.

[72] B. Rosenberg, L. Van Camp, T. Krigas, Inhibition of Cell Division in Escherichia coli by Electrolysis Products from a Platinum Electrode, Nature. 205 (1965) 698–699. doi:10.1038/205698a0.

[73] M. Peyrone, Ueber die Einwirkung des Ammoniaks auf Platinchlorür, Ann. Der Chemie Und Pharm. 51 (1844) 1–29. doi:10.1002/jlac.18440510102.

[74] T.C. Johnstone, G.Y. Park, S.J. Lippard, Understanding and improving platinum anticancer drugs--phenanthriplatin., Anticancer Res. 34 (2014) 471–6. http://www.ncbi.nlm.nih.gov/pubmed/24403503%0Ahttp://www.pubmedcentral.nih.gov/articlerender.fcgi?artid=PMC3937549.

[75] Platinum based Cancer Drug Market 2019| Worldwide Overview by Industry Size, Market Share, Future Trends, Growth Factors and Leading Players Research Report Analysis by 360 Market Updates - MarketWatch, (2019). https://www.marketwatch.com/press-release/platinum-based-cancer-drug-market-2019-worldwide-overview-by-industry-size-market-share-future-trends-growth-factors-and-leading-players-research-report-analysis-by-360-market-updates-2019-04-03 (accessed July 9, 2019).

[76] N. Shah, D.S. Dizon, New-Generation Platinum Agents for Solid Tumors, Futur. Oncol. 5 (2009) 33–42. https://www.medscape.com/viewarticle/589012 (accessed July 9, 2019).

[77] S. Ghosh, Cisplatin: The first metal based anticancer drug, Bioorg. Chem. 88 (2019). doi:10.1016/j.bioorg.2019.102925.

[78] J.C. Dabrowiak, Platinum Drugs for Treating Cancer, Met. Med. (2017) 91–156. doi:10.1002/9781119191377.ch3.

[79] L. Kelland, The resurgence of platinum-based cancer chemotherapy, Nat. Rev. Cancer. 7 (2007) 573–584. doi:10.1038/nrc2167.

[80] FDA Approved Drug Products, 2019. https://www.accessdata.fda.gov/scripts/cder/daf/index.cfm?event=reportsSearch.process&rptName=2&reportSelectMonth=12&reportSelectYear=1978&nav (accessed July 10, 2019).

[81] S. Dasari, P. Bernard Tchounwou, Cisplatin in cancer therapy: Molecular mechanisms of action, Eur. J. Pharmacol. 740 (2014) 364–378. doi:10.1016/j.ejphar.2014.07.025.

[82] C. Monneret, Platinum anticancer drugs. From serendipity to rational design, Ann. Pharm. Fr. 69 (2011) 286–295. doi:10.1016/j.pharma.2011.10.001.

[83] A. Basu, S. Krishnamurthy, Cellular responses to Cisplatin-induced DNA damage., J. Nucleic

Acids. 2010 (2010). doi:10.4061/2010/201367.

[84] C. Rocha, M. Silva, A. Quinet, J. Cabral-Neto, C. Menck, DNA repair pathways and cisplatin resistance: an intimate relationship, Clinics. 73 (2018) 1–10. doi:10.6061/clinics/2018/e478s.

[85] S.A. Aldossary, Review on Pharmacology of Cisplatin: Clinical Use, Toxicity and Mechanism of Resistance of Cisplatin, Biomed. Pharmacol. J. 11 (2019) 07–15. doi:10.13005/bpj/1608.

[86] R. Oun, Y.E. Moussa, N.J. Wheate, The side effects of platinum-based chemotherapy drugs: A review for chemists, Dalt. Trans. 47 (2018) 6645–6653. doi:10.1039/c8dt00838h.

[87] Q. Cao, Y. Li, E. Freisinger, P.Z. Qin, R.K.O. Sigel, Z.-W. Mao, G-quadruplex DNA targeted metal complexes acting as potential anticancer drugs, Inorg. Chem. Front. 4 (2017) 10–32. doi:10.1039/C6QI00300A.

[88] H. Yang, W. Kong, L. He, J.-J. Zhao, J.D. O'Donnell, J. Wang, R.M. Wenham, D. Coppola, P.A. Kruk, S. V. Nicosia, J.Q. Cheng, MicroRNA Expression Profiling in Human Ovarian Cancer: miR-214 Induces Cell Survival and Cisplatin Resistance by Targeting PTEN, Cancer Res. 68 (2008) 425–433. doi:10.1158/0008-5472.CAN-07-2488.

[89] J. Liu, W. Chen, H. Zhang, T. Liu, L. Zhao, miR-214 targets the PTEN-mediated PI3K/Akt signaling pathway and regulates cell proliferation and apoptosis in ovarian cancer, Oncol. Lett. 14 (2017) 5711–5718. doi:10.3892/ol.2017.6953.

[90] L. Bao, J. Wu, M. Dodson, E.M. Rojo de la Vega, Y. Ning, Z. Zhang, M. Yao, D.D. Zhang, C. Xu, X. Yi, ABCF2, an Nrf2 target gene, contributes to cisplatin resistance in ovarian cancer cells., Mol. Carcinog. 56 (2017) 1543–1553. doi:10.1002/mc.22615.

[91] S. Alonezi, J. Tusiimire, J. Wallace, M.J. Dufton, J.A. Parkinson, L.C. Young, C.J. Clements, J.-K. Park, J.-W. Jeon, V.A. Ferro, D.G. Watson, Metabolomic Profiling of the Synergistic Effects of Melittin in Combination with Cisplatin on Ovarian Cancer Cells., Metabolites. 7 (2017). doi:10.3390/metabo7020014.

[92] Y. Wang, X. Deng, C. Yu, G. Zhao, J. Zhou, G. Zhang, M. Li, D. Jiang, Z. Quan, Y. Zhang, Synergistic inhibitory effects of capsaicin combined with cisplatin on human osteosarcoma in culture and in xenografts., J. Exp. Clin. Cancer Res. 37 (2018) 251. doi:10.1186/s13046-018-0922-0.

[93] M. Alizadehnohi, M. Nabiuni, Z. Nazari, Z. Safaeinejad, S. Irian, The synergistic cytotoxic effect of cisplatin and honey bee venom on human ovarian cancer cell line A2780cp., J. Venom Res. 3 (2012) 22–7. http://www.ncbi.nlm.nih.gov/pubmed/23301148 (accessed September 7, 2019).

[94] S. Pecorelli, H.C. Wagenaar, I.B. Vergote, D. Curran, L. V Beex, E. Wiltshaw, J.B. Vermorken, Cisplatin (P), vinblastine (V) and bleomycin (B) combination chemotherapy in recurrent or advanced granulosa(-theca) cell tumours of the ovary. An EORTC Gynaecological Cancer Cooperative Group study., Eur. J. Cancer. 35 (1999) 1331–7. doi:10.1016/s0959-8049(99)00142-2.

[95] H. Wu, H. Jin, C. Wang, Z. Zhang, H. Ruan, L. Sun, C. Yang, Y. Li, W. Qin, C. Wang, Synergistic Cisplatin/Doxorubicin Combination Chemotherapy for Multidrug-Resistant Cancer via Polymeric Nanogels Targeting Delivery, ACS Appl. Mater. Interfaces. 9 (2017) 9426–9436. doi:10.1021/acsami.6b16844.

[96] S. Uddin, Z. Jehan, M. Ahmed, A. Alyan, F. Al-Dayel, A. Hussain, P. Bavi, K.S. Al-Kuraya, Overexpression of Fatty Acid Synthase in Middle Eastern Epithelial Ovarian Carcinoma

Activates AKT and Its Inhibition Potentiates Cisplatin-Induced Apoptosis, Mol. Med. 17 (2011) 635–645. doi:10.2119/molmed.2011.00046.

[97] I.W. Achkar, N. Abdulrahman, H. Al-Sulaiti, J.M. Joseph, S. Uddin, F. Mraiche, Cisplatin based therapy: the role of the mitogen activated protein kinase signaling pathway, J. Transl. Med. 16 (2018). doi:10.1186/S12967-018-1471-1.

[98] H.S. Oberoi, N. V Nukolova, A. V Kabanov, T.K. Bronich, Nanocarriers for delivery of platinum anticancer drugs., Adv. Drug Deliv. Rev. 65 (2013) 1667–85. doi:10.1016/j.addr.2013.09.014.

[99] Drugs@FDA: FDA Approved Drug Products, (n.d.). https://www.accessdata.fda.gov/scripts/cder/daf/index.cfm?event=reportsSearch.process&rptName=1&reportSelectMonth=3&reportSelectYear=1989&nav (accessed July 11, 2019).

[100] D. Chen, V. Milacic, M. Frezza, Q. Dou, Metal Complexes, their Cellular Targets and Potential for Cancer Therapy, Curr. Pharm. Des. 15 (2009) 777–791. doi:10.2174/138161209787582183.

[101] X. Chen, J. Wang, Z. Fu, B. Zhu, J. Wang, S. Guan, Z. Hua, Curcumin activates DNA repair pathway in bone marrow to improve carboplatin-induced myelosuppression, Sci. Rep. 7 (2017) 1–11. doi:10.1038/s41598-017-16436-9.

[102] A. Ibrahim, S. Hirschfeld, M.H. Cohen, D.J. Griebel, G.A. Williams, R. Pazdur, FDA drug approval summaries: oxaliplatin., Oncologist. 9 (2004) 8–12. doi:10.1634/theoncologist.9-1-8.

[103] M.. Thierry André, M.D., Corrado Boni, M.D., Lamia Mounedji-Boudiaf, M.D., Matilde Navarro, M.D., Josep Tabernero, M.D., Tamas Hickish, M.D., Clare Topham, M.D., Marta Zaninelli, M.D., Philip Clingan, M.D., John Bridgewater, M.D., Isabelle Tabah-Fisch, M.D., Oxaliplatin, Fluorouracil, and Leucovorin as Adjuvant Treatment for Colon Cancer Thierry, N. Engl. J. Med. 350 (2004) 2343–51. doi:10.1056/NEJMoa032709.

[104] L.E. Raez, S. Kobina, E.S. Santos, Oxaliplatin in first-line therapy for advanced non-small-cell lung cancer, Clin. Lung Cancer. 11 (2010) 18–24. doi:10.3816/CLC.2010.n.003.

[105] H. Starobova, I. Vetter, Pathophysiology of Chemotherapy-Induced Peripheral Neuropathy, Front. Mol. Neurosci. 10 (2017) 1–21. doi:10.3389/fnmol.2017.00174.

[106] T. Shalaby, G. Fiaschetti, K. Nagasawa, K. Shin-Ya, M. Baumgartner, M. Grotzer, G-quadruplexes as potential therapeutic targets for embryonal tumors, Molecules. 18 (2013) 12500–12537. doi:10.3390/molecules181012500.

[107] I. Bang, Untersuchungen über die Guanylsäre, Biochem. Z. 26 (1910) 293–311. https://www.researchgate.net/publication/284409160_Untersuchungen_uber_die_Guanylsare (accessed July 12, 2019).

[108] M. Gellert, M.N. Lipsett, D.R. Davies, Helix formation by guanylic acid., Proc. Natl. Acad. Sci. U. S. A. 48 (1962) 2013–8. doi:10.1073/pnas.48.12.2013.

[109] D.N. Edwards, A. Machwe, Z. Wang, D.K. Orren, Intramolecular telomeric G-quadruplexes dramatically inhibit DNA synthesis by replicative and translesion polymerases, revealing their potential to lead to genetic change, PLoS One. 9 (2014). doi:10.1371/journal.pone.0080664.

[110] J. Bidzinska, G. Cimino-Reale, N. Zaffaroni, M. Folini, G-quadruplex structures in the human genome as novel therapeutic targets, Molecules. 18 (2013) 12368–12395. doi:10.3390/molecules181012368.

[111] D. Rhodes, H.J. Lipps, Survey and summary G-quadruplexes and their regulatory roles in biology, Nucleic Acids Res. 43 (2015) 8627–8637. doi:10.1093/nar/gkv862.

[112] S. Burge, G.N. Parkinson, P. Hazel, A.K. Todd, S. Neidle, Quadruplex DNA: Sequence, topology and structure, Nucleic Acids Res. 34 (2006) 5402–5415. doi:10.1093/nar/gkl655.

[113] S. Millevoi, H. Moine, S. Vagner, G-quadruplexes in RNA biology, Wiley Interdiscip. Rev. RNA. 3 (2012) 495–507. doi:10.1002/wrna.1113.

[114] E. Largy, J.-L. Mergny, V. Gabelica, Role of Alkali Metal Ions in G-Quadruplex Nucleic Acid Structure and Stability, in: Met. Ions Life Sci., 2016: pp. 203–258. doi:10.1007/978-3-319-21756-7_7.

[115] D. Yang, K. Okamoto, Structural insights into G-quadruplexes: Towards new anticancer drugs, Future Med. Chem. 2 (2010) 619–646. doi:10.4155/fmc.09.172.

[116] M. Malgowska, K. Czajczynska, D. Gudanis, A. Tworak, Z. Gdaniec, Overview of the RNA G-quadruplex structures., Acta Biochim. Pol. 63 (2016) 609–621. doi:10.18388/abp.2016_1335.

[117] A. Nuthanakanti, I. Ahmed, S.Y. Khatik, K. Saikrishnan, S.G. Srivatsan, Probing G-quadruplex topologies and recognition concurrently in real time and 3D using a dual-app nucleoside probe, Nucleic Acids Res. 47 (2019) 6059–6072. doi:10.1093/nar/gkz516.

[118] J.Y. Lee, J. Yoon, H.W. Kihm, D.S. Kim, Structural Diversity and Extreme Stability of Unimolecular Oxytricha nova Telomeric G-Quadruplex, Biochemistry. 47 (2008) 3389–3396. doi:10.1021/bi702013d.

[119] J.L. Huppert, Four-stranded nucleic acids: Structure, function and targeting of G-quadruplexes, Chem. Soc. Rev. 37 (2008) 1375–1384. doi:10.1039/b702491f.

[120] D.L. Ma, Z. Zhang, M. Wang, L. Lu, H.J. Zhong, C.H. Leung, Recent Developments in G-Quadruplex Probes, Chem. Biol. 22 (2015) 812–828. doi:10.1016/j.chembiol.2015.06.016.

[121] X. Cang, J. Šponer, T.E. Cheatham, Explaining the varied glycosidic conformational, G-tract length and sequence preferences for anti-parallel G-quadruplexes, Nucleic Acids Res. 39 (2011) 4499–4512. doi:10.1093/nar/gkr031.

[122] T. Ou, Y. Lu, J. Tan, Z. Huang, K.-Y. Wong, L. Gu, G-Quadruplexes: Targets in Anticancer Drug Design, ChemMedChem. 3 (2008) 690–713. doi:10.1002/cmdc.200700300.

[123] X. Cang, J. Šponer, T.E. Cheatham, Insight into G-DNA structural polymorphism and folding from sequence and loop connectivity through free energy analysis, J. Am. Chem. Soc. 133 (2011) 14270–14279. doi:10.1021/ja107805r.

[124] S. Pandey, P. Agarwala, S. Maiti, Effect of Loops and G-Quartets on the Stability of RNA, J. Phys. Chem. B. 117 (2013) 6896–6905. doi:dx.doi.org/10.1021/jp401739m.

[125] A. Piazza, M. Adrian, F. Samazan, B. Heddi, F. Hamon, A. Serero, J. Lopes, M.-P. Teulade-Fichou, A.T. Phan, A. Nicolas, Short loop length and high thermal stability determine genomic instability induced by G-quadruplex-forming minisatellites, EMBO J. 34 (2015) 1718–1734. doi:10.15252/embj.201490702.

[126] M.M. Fay, S.M. Lyons, P. Ivanov, RNA G-Quadruplexes in Biology: Principles and Molecular Mechanisms, J. Mol. Biol. 429 (2017) 2127–2147. doi:10.1016/j.jmb.2017.05.017.

[127] P. Agarwala, S. Pandey, S. Maiti, The tale of RNA G-quadruplex, Org. Biomol. Chem. 13 (2015) 5570–5585. doi:10.1039/c4ob02681k.

[128] M. Kaushik, S. Kaushik, S. Kukreti, Exploring the characterization tools of Guanine-Quadruplexes, Front. Biosci. 21 (2016) 468–478. doi:10.2741/4402.

[129] M. Małgowska, D. Gudanis, A. Teubert, G. Dominiak, Z. Gdaniec, How to study G-quadruplex structures, Biotechnologia. 93 (2013) 381–390. doi:10.5114/bta.2012.46592.

[130] H.M. Wong, O. Stegle, S. Rodgers, J.L. Huppert, A toolbox for predicting G-quadruplex formation and stability, J. Nucleic Acids. 2010 (2010). doi:10.4061/2010/564946.

[131] S. Haider, Computational Methods to Study G-Quadruplex–Ligand Complexes, J. Indian Inst. Sci. 98 (2018) 325–339. doi:10.1007/s41745-018-0083-3.

[132] Q. Li, J.-F. Xiang, Q.-F. Yang, H.-X. Sun, A.-J. Guan, Y.-L. Tang, G4LDB: a database for discovering and studying G-quadruplex ligands., Nucleic Acids Res. 41 (2013) D1115-23. doi:10.1093/nar/gks1101.

[133] J. Jaumot, R. Gargallo, Experimental methods for studying the interactions between G-quadruplex structures and ligands., Curr. Pharm. Des. 18 (2012) 1900–16. http://www.ncbi.nlm.nih.gov/pubmed/22376108 (accessed July 25, 2019).

[134] E.I. Solomon, A.B.P. Lever, Inorganic electronic structure and spectroscopy, Wiley, 1999. https://books.google.at/books?id=C7KaQgAACAAJ&redir_esc=y.

[135] R. Del Villar-Guerra, R.D. Gray, J.B. Chaires, Characterization of quadruplex DNA structure by circular dichroism, Curr. Protoc. Nucleic Acid Chem. 2017 (2017) 17.8.1-17.8.16. doi:10.1002/cpnc.23.

[136] M. Vorlíčková, I. Kejnovská, J. Sagi, D. Renčiuk, K. Bednářová, J. Motlová, J. Kypr, Circular dichroism and guanine quadruplexes, Methods. 57 (2012) 64–75. doi:10.1016/j.ymeth.2012.03.011.

[137] J. Kypr, I. Kejnovska, D. Renciuk, M. Vorlickova, Circular dichroism and conformational polymorphism of DNA, Nucleic Acids Res. 37 (2009) 1713–1725. doi:10.1093/nar/gkp026.

[138] R. Del Villar-Guerra, J.O. Trent, J.B. Chaires, G-Quadruplex Secondary Structure Obtained from Circular Dichroism Spectroscopy., Angew. Chem. Int. Ed. Engl. 57 (2018) 7171–7175. doi:10.1002/anie.201709184.

[139] J.-L. Mergny, A.-T. Phan, L. Lacroix, Following G-quartet formation by UV-spectroscopy, FEBS Lett. 435 (1998) 74–78. doi:10.1016/S0014-5793(98)01043-6.

[140] B. Juskowiak, S. Takenaka, Fluorescence Resonance Energy Transfer in the Studies of Guanine Quadruplexes, in: Fluoresc. Energy Transf. Nucleic Acid Probes, Humana Press, New Jersey, 2006: pp. 311–342. doi:10.1385/1-59745-069-3:311.

[141] D.G. Norman, R.J. Grainger, D. Uhrìn, D.M.J. Lilley, Location of Cyanine-3 on Double-Stranded DNA Importance for Fluorescence.pdf, Biochemistry. 39 (2000) 6317–6324.

[142] B.T. Bajar, E.S. Wang, S. Zhang, M.Z. Lin, J. Chu, A guide to fluorescent protein FRET pairs, Sensors. 16 (2016) 1–24. doi:10.3390/s16091488.

[143] T. Förster, Energiewanderung und Fluoreszenz, Naturwissenschaften. 33 (1946) 166–175. doi:10.1007/BF00585226.

[144] J.A. Broussard, B. Rappaz, D.J. Webb, C.M. Brown, Fluorescence resonance energy transfer microscopy as demonstrated by measuring the activation of the serine/threonine kinase Akt, Nat. Protoc. 8 (2013) 265–281. doi:10.1038/nprot.2012.147.

[145] M.C. Chirio-Lebrun, M. Prats, Fluorescence resonance energy transfer (FRET): Theory and experiments, Biochem. Educ. 26 (1998) 320–323. doi:10.1016/S0307-4412(98)80010-1.

[146] K. Aoki, Y. Kamioka, M. Matsuda, Fluorescence resonance energy transfer imaging of cell signaling from in vitro to in vivo: Basis of biosensor construction, live imaging, and image processing, Dev. Growth Differ. 55 (2013) 515–522. doi:10.1111/dgd.12039.

[147] P.S. Shirude, S. Balasubramanian, Single molecule conformational analysis of DNA G-quadruplexes, Biochimie. 90 (2008) 1197–1206. doi:10.1016/j.biochi.2008.01.015.

[148] M.S. Smyth, J.H.J. Martin, Review x Ray crystallography, J Clin Pathol Mol Pathol. 53 (2000) 8–14. doi:10.1136/mp.53.1.8.

[149] K. Hasegawa, X-Introduction to single crystal X-ray analysis I. What is X-ray crystallography?, Rigaku J. 28 (2012) 14–18. http://www.rigaku.com/downloads/journal/RJ28-1/RJ28-1_14-18s.pdf.

[150] J. Holcomb, N. Spellmon, Y. Zhang, M. Doughan, C. Li, Z. Yang, Protein crystallization: Eluding the bottleneck of X-ray crystallography, AIMS Biophys. 4 (2017) 557–575. doi:10.3934/biophy.2017.4.557.

[151] D.A. Shapiro, D. DePonte, R.B. Doak, P. Fromme, G. Hembree, M. Hunter, S. Marchesini, K. Schmidt, D. Starodub, U. Weierstall, H. Chapman, J. Spence, X-Ray Powder Diffraction from Sub-Micron Crystals of Photosystem-1 Membrane Protein, (2008). http://arxiv.org/abs/0803.4027 (accessed July 30, 2019).

[152] H. Zheng, K.B. Handing, M.D. Zimmerman, I.G. Shabalin, S.C. Almo, W. Minor, X-ray crystallography over the past decade for novel drug discovery - where are we heading next?, Expert Opin. Drug Discov. 10 (2015) 975–89. doi:10.1517/17460441.2015.1061991.

[153] M. Webba da Silva, NMR methods for studying quadruplex nucleic acids, Methods. 43 (2007) 264–277. doi:10.1016/j.ymeth.2007.05.007.

[154] P. Murat, Y. Singh, E. Defrancq, Methods for investigating G-quadruplex DNA/ligand interactions, Chem. Soc. Rev. 40 (2011) 5293–5307. doi:10.1039/c1cs15117g.

[155] N. Saranathan, P. Vivekanandan, G-Quadruplexes: More Than Just a Kink in Microbial Genomes, Trends Microbiol. 27 (2019) 148–163. doi:10.1016/j.tim.2018.08.011.

[156] M. Bartas, M. Cutová, V. Brázda, P. Kaura, J. Šťastný, J. Kolomazník, J. Coufal, P. Goswami, J. Červeň, P. Pečinka, The presence and localization of G-Quadruplex forming sequences in the domain of bacteria, Molecules. 24 (2019). doi:10.3390/molecules24091711.

[157] B.D. Griffin, H.W. Bass, Review: Plant G-quadruplex (G4) motifs in DNA and RNA; abundant, intriguing sequences of unknown function, Plant Sci. 269 (2018) 143–147. doi:10.1016/j.plantsci.2018.01.011.

[158] M. Metifiot, S. Amrane, S. Litvak, M.L. Andreola, Survey and summary G-quadruplexes in viruses: Function and potential therapeutic applications, Nucleic Acids Res. 42 (2014) 12352–12366. doi:10.1093/nar/gku999.

[159] N. Beaume, R. Pathak, V.K. Yadav, S. Kota, H.S. Misra, H.K. Gautam, S. Chowdhury, Genome-wide study predicts promoter-G4 DNA motifs regulate selective functions in bacteria: Radioresistance of D. radiodurans involves G4 DNA-mediated regulation, Nucleic Acids Res. 41 (2013) 76–89. doi:10.1093/nar/gks1071.

[160] P. Armas, N.B. Calcaterra, G-quadruplex in animal development: Contribution to gene expression and genomic heterogeneity, Mech. Dev. 154 (2018) 64–72. doi:10.1016/j.mod.2018.05.004.

[161] E. Lavezzo, M. Berselli, I. Frasson, R. Perrone, G. Palù, A.R. Brazzale, S.N. Richter, S. Toppo, G-quadruplex forming sequences in the genome of all known human viruses: A comprehensive guide., PLoS Comput. Biol. 14 (2018) e1006675. doi:10.1371/journal.pcbi.1006675.

[162] V.S. Chambers, G. Marsico, J.M. Boutell, M. Di Antonio, G.P. Smith, S. Balasubramanian, High-throughput sequencing of DNA G-quadruplex structures in the human genome, Nat. Biotechnol. 33 (2015) 877–881. doi:10.1038/nbt.3295.

[163] S.L.B. König, A.C. Evans, J.L. Huppert, Seven essential questions on G-quadruplexes, Biomol. Concepts. 1 (2010) 197–213. doi:10.1515/bmc.2010.011.

[164] S. Frees, C. Menendez, M. Crum, P.S. Bagga, QGRS-Conserve: A computational method for discovering evolutionarily conserved G-quadruplex motifs, Hum. Genomics. 8 (2014) 1–13. doi:10.1186/1479-7364-8-8.

[165] J. Qiu, M. Wang, Y. Zhang, P. Zeng, T.-M. Ou, J.-H. Tan, S.-L. Huang, L.-K. An, H. Wang, L.-Q. Gu, Z.-S. Huang, D. Li, Biological Function and Medicinal Research Significance of G-Quadruplex Interactive Proteins., Curr. Top. Med. Chem. 15 (2015) 1971–87. http://www.ncbi.nlm.nih.gov/pubmed/25980412 (accessed August 1, 2019).

[166] E. Henderson, C.C. Hardin, S.K. Walk, I. Tinoco, E.H. Blackburn, Telomeric DNA oligonucleotides form novel intramolecular structures containing guanine·guanine base pairs, Cell. 51 (1987) 899–908. doi:10.1016/0092-8674(87)90577-0.

[167] K. Muraki, K. Nyhan, L. Han, J.P. Murnane, Mechanisms of telomere loss and their consequences for chromosome instability, Front. Oncol. 2 (2012) 1–13. doi:10.3389/fonc.2012.00135.

[168] C. Lin, D. Yang, Human Telomeric G-Quadruplex Structures and G-Quadruplex-Interactive Compounds., Methods Mol. Biol. 1587 (2017) 171–196. doi:10.1007/978-1-4939-6892-3_17.

[169] W. Lu, Y. Zhang, D. Liu, Z. Songyang, M. Wan, Telomere- structure, function, and regulation, Exp Cell Res. 4 (2011) 133–141. doi:10.1126/scisignal.2001449.Engineering.

[170] T. de Lange, Shelterin-Mediated Telomere Protection, Annu. Rev. Genet. 52 (2018) 223–247. doi:10.1146/annurev-genet-032918-021921.

[171] Y. Doksani, The response to dna damage at telomeric repeats and its consequences for telomere function, Genes (Basel). 10 (2019) 1–17. doi:10.3390/genes10040318.

[172] C.M. Roake, S.E. Artandi, Control of Cellular Aging, Tissue Function, and Cancer by p53 Downstream of Telomeres., Cold Spring Harb. Perspect. Med. 7 (2017). doi:10.1101/cshperspect.a026088.

[173] T. Janovič, M. Stojaspal, P. Veverka, D. Horáková, C. Hofr, Human Telomere Repeat Binding Factor TRF1 Replaces TRF2 Bound to Shelterin Core Hub TIN2 when TPP1 Is Absent, J. Mol. Biol. (2019) 1–13. doi:10.1016/j.jmb.2019.05.038.

[174] R.E. Verdun, J. Karlseder, Replication and protection of telomeres, Nature. 447 (2007) 924–931. doi:10.1038/nature05976.

[175] J. Karlseder, K. Hoke, O.K. Mirzoeva, C. Bakkenist, M.B. Kastan, J.H.J. Petrini, T. de Lange, The telomeric protein TRF2 binds the ATM kinase and can inhibit the ATM-dependent DNA damage response., PLoS Biol. 2 (2004) E240. doi:10.1371/journal.pbio.0020240.

[176] R.M. Stansel, T. de Lange, J.D. Griffith, T-loop assembly in vitro involves binding of TRF2 near the 3' telomeric overhang., EMBO J. 20 (2001) 5532–40. doi:10.1093/emboj/20.19.5532.

[177] A.M. Olovnikov, A theory of marginotomy: The incomplete copying of template margin in enzymic synthesis of polynucleotides and biological significance of the phenomenon, J. Theor. Biol. 41 (1973) 181–190. doi:10.1016/0022-5193(73)90198-7.

[178] A. Suram, U. Herbig, The replicometer is broken: Telomeres activate cellular senescence in response to genotoxic stresses, Aging Cell. 13 (2014) 780–786. doi:10.1111/acel.12246.

[179] R.J. Hodes, K.S. Hathcock, N.P. Weng, Telomeres in T and B cells, Nat. Rev. Immunol. 2 (2002) 699–706. doi:10.1038/nri890.

[180] L. Hayflick, The limited in vitro lifetime of human diploid cell strains, Exp. Cell Res. 37 (1965) 614–636. doi:10.1016/0014-4827(65)90211-9.

[181] M.A. Jafri, S.A. Ansari, M.H. Alqahtani, J.W. Shay, Roles of telomeres and telomerase in cancer, and advances in telomerase-targeted therapies, Genome Med. 8 (2016). doi:10.1186/s13073-016-0324-x.

[182] K. Turner, V. Vasu, D. Griffin, Telomere Biology and Human Phenotype, Cells. 8 (2019) 73. doi:10.3390/cells8010073.

[183] T.B. Gaspar, A. Sá, J.M. Lopes, M. Sobrinho-Simões, P. Soares, J. Vinagre, Telomere maintenance mechanisms in cancer, Genes (Basel). 9 (2018). doi:10.3390/genes9050241.

[184] N. Kim, M. Piatyszek, K. Prowse, C. Harley, M. West, P. Ho, G. Coviello, W. Wright, S. Weinrich, J. Shay, Specific association of human telomerase activity with immortal cells and cancer, Science (80-.). 266 (1994) 2011–2015. doi:10.1126/science.7605428.

[185] M. Ivancich, Z. Schrank, L. Wojdyla, B. Leviskas, A. Kuckovic, A. Sanjali, N. Puri, Treating cancer by targeting telomeres and telomerase, Antioxidants. 6 (2017). doi:10.3390/antiox6010015.

[186] O.E. Bechter, Y. Zou, J.W. Shay, W.E. Wright, Homologous recombination in human telomerase-positive and ALT cells occurs with the same frequency., EMBO Rep. 4 (2003) 1138–43. doi:10.1038/sj.embor.7400027.

[187] F.P. Barthel, W. Wei, M. Tang, E. Martinez-Ledesma, X. Hu, S.B. Amin, K.C. Akdemir, S. Seth, X. Song, Q. Wang, T. Lichtenberg, J. Hu, J. Zhang, S. Zheng, R.G.W. Verhaak, Systematic analysis of telomere length and somatic alterations in 31 cancer types, Nat. Genet. 49 (2017) 349–357. doi:10.1038/ng.3781.

[188] M. De Vitis, F. Berardinelli, A. Sgura, Telomere length maintenance in cancer: At the crossroad between telomerase and alternative lengthening of telomeres (ALT), Int. J. Mol. Sci. 19 (2018). doi:10.3390/ijms19020606.

[189] M.A. Cerone, J.A. Londono-Vallejo, S. Bacchetti, Telomere maintenance by telomerase and by recombination can coexist in human cells, Hum. Mol. Genet. 10 (2001) 1945–1952. doi:10.1093/hmg/10.18.1945.

[190] R.A.A. Alnafakh, M. Adishesh, L. Button, G. Saretzki, D.K. Hapangama, Telomerase and telomeres in endometrial cancer, Front. Oncol. 9 (2019). doi:10.3389/fonc.2019.00344.

[191] F.L. Zhong, L.F.Z. Batista, A. Freund, M.F. Pech, A.S. Venteicher, S.E. Artandi, TPP1 OB-fold domain controls telomere maintenance by recruiting telomerase to chromosome ends., Cell. 150 (2012) 481–94. doi:10.1016/j.cell.2012.07.012.

[192] K. Cleal, K. Norris, D. Baird, Telomere length dynamics and the evolution of cancer genome architecture, Int. J. Mol. Sci. 19 (2018) 1–17. doi:10.3390/ijms19020482.

[193] S. Neidle, G. Parkinson, Telomere maintenance as a target for anticancer drug discovery, Nat. Rev. Drug Discov. 1 (2002) 383–393. doi:10.1038/nrd793.

[194] E. Fathi, H.N. Charoudeh, Z. Sanaat, R. Farahzadi, Telomere shortening as a hallmark of stem cell senescence, Stem Cell Investig. 6 (2019). doi:10.21037/sci.2019.02.04.

[195] R. Leão, J.D. Apolónio, D. Lee, A. Figueiredo, U. Tabori, P. Castelo-Branco, Mechanisms of human telomerase reverse transcriptase (hTERT) regulation: clinical impacts in cancer., J. Biomed. Sci. 25 (2018) 22. doi:10.1186/s12929-018-0422-8.

[196] D. Sun, B. Thompson, B.E. Cathers, M. Salazar, S.M. Kerwin, J.O. Trent, T.C. Jenkins, S. Neidle, L.H. Hurley, Inhibition of Human Telomerase by a G-Quadruplex-Interactive Compound, J. Med. Chem. 40 (1997) 2113–2116. doi:10.1021/jm970199z.

[197] A.M. Zahler, J.R. Williamson, T.R. Cech, D.M. Prescott, Inhibition of telomerase by G-quartet DNA structures, Nature. 350 (1991) 718–720. doi:10.1038/350718a0.

[198] Z.Y. Sun, X.N. Wang, S.Q. Cheng, X.X. Su, T.M. Ou, Developing novel G-quadruplex ligands: From interaction with nucleic acids to interfering with nucleic acid–protein interaction, Molecules. (2019). doi:10.3390/molecules24030396.

[199] G. Wu, L. Chen, W. Liu, D. Yang, Molecular recognition of the hybrid-type G-quadruplexes in human telomeres, Molecules. (2019). doi:10.3390/molecules24081578.

[200] M.A. Harris, J. Clark, A. Ireland, J. Lomax, M. Ashburner, R. Foulger, K. Eilbeck, S. Lewis, B. Marshall, C. Mungall, J. Richter, G.M. Rubin, J.A. Blake, C. Bult, M. Dolan, H. Drabkin, J.T. Eppig, D.P. Hill, L. Ni, M. Ringwald, R. Balakrishnan, J.M. Cherry, K.R. Christie, M.C. Costanzo, S.S. Dwight, S. Engel, D.G. Fisk, J.E. Hirschman, E.L. Hong, R.S. Nash, A. Sethuraman, C.L. Theesfeld, D. Botstein, K. Dolinski, B. Feierbach, T. Berardini, S. Mundodi, S.Y. Rhee, R. Apweiler, D. Barrell, E. Camon, E. Dimmer, V. Lee, R. Chisholm, P. Gaudet, W. Kibbe, R. Kishore, E.M. Schwarz, P. Sternberg, M. Gwinn, L. Hannick, J. Wortman, M. Berriman, V. Wood, N. de la Cruz, P. Tonellato, P. Jaiswal, T. Seigfried, R. White, Gene Ontology Consortium, The Gene Ontology (GO) database and informatics resource., Nucleic Acids Res. 32 (2004) D258-61. doi:10.1093/nar/gkh036.

[201] J.L. Huppert, S. Balasubramanian, G-quadruplexes in promoters throughout the human genome, Nucleic Acids Res. 35 (2007) 406–413. doi:10.1093/nar/gkl1057.

[202] S. Balasubramanian, L.H. Hurley, S. Neidle, Targeting G-quadruplexes in gene promoters: A novel anticancer strategy?, Nat. Rev. Drug Discov. 10 (2011) 261–275. doi:10.1038/nrd3428.

[203] F. Blombach, K.L. Smollett, D. Grohmann, F. Werner, Molecular Mechanisms of Transcription Initiation - Structure, Function, and Evolution of TFE/TFIIE-Like Factors and Open Complex Formation, J. Mol. Biol. 428 (2016) 2592–2606. doi:10.1016/j.jmb.2016.04.016.

[204] P. Armas, A. David, N.B. Calcaterra, Transcriptional control by G-quadruplexes: In vivo roles and perspectives for specific intervention, Transcription. 8 (2017) 21–25. doi:10.1080/21541264.2016.1243505.

[205] N. Kim, The interplay between G-quadruplex and Transcription, Curr. Med. Chem. 25 (2018) 2898–2917. doi:10.2174/0929867325666171229132619.

[206] J. Eddy, N. Maizels, Gene function correlates with potential for G4 DNA formation in the human genome, Nucleic Acids Res. 34 (2006) 3887–3896. doi:10.1093/nar/gkl529.

[207] T.A. Brooks, S. Kendrick, L. Hurley, Making sense of G-quadruplex and i-motif functions in

oncogene promoters, FEBS Jopurnal. 277 (2010) 3459–3469. doi:10.1111/j.1742-4658.2010.07759.x.Making.

[208] J. Jana, S. Mondal, P. Bhattacharjee, P. Sengupta, T. Roychowdhury, P. Saha, P. Kundu, S. Chatterjee, Chelerythrine down regulates expression of VEGFA, BCL2 and KRAS by arresting G-Quadruplex structures at their promoter regions., Sci. Rep. 7 (2017) 40706. doi:10.1038/srep40706.

[209] P. Podbevšek, J. Plavec, KRAS promoter oligonucleotide with decoy activity dimerizes into a unique topology consisting of two G-quadruplex units., Nucleic Acids Res. 44 (2016) 917–25. doi:10.1093/nar/gkv1359.

[210] S. Cogoi, L.E. Xodo, G-quadruplex formation within the promoter of the KRAS proto-oncogene and its effect on transcription, Nucleic Acids Res. 34 (2006) 2536–2549. doi:10.1093/nar/gkl286.

[211] S. Cogoi, A. Ferino, G. Miglietta, E.B. Pedersen, L.E. Xodo, The regulatory G4 motif of the Kirsten ras (KRAS) gene is sensitive to guanine oxidation: implications on transcription., Nucleic Acids Res. 46 (2018) 661–676. doi:10.1093/nar/gkx1142.

[212] E. Ruggiero, S.N. Richter, G-quadruplexes and G-quadruplex ligands: targets and tools in antiviral therapy, Nucleic Acids Res. 46 (2018) 3270–3283. doi:10.1093/nar/gky187.

[213] S. Zhang, H. Sun, D. Yang, Y. Liu, X. Zhang, H. Chen, Q. Li, A. Guan, Y. Tang, Evaluation of the selectivity of G-quadruplex ligands in living cells with a small molecule fluorescent probe, Anal. Chim. Acta X. 2 (2019) 100017. doi:10.1016/j.acax.2019.100017.

[214] B.J. Chen, Y.L. Wu, Y. Tanaka, W. Zhang, Small molecules targeting c-Myc oncogene: Promising anti-cancer therapeutics, Int. J. Biol. Sci. 10 (2014) 1084–1096. doi:10.7150/ijbs.10190.

[215] D. Monchaud, M.P. Teulade-Fichou, A hitchhiker's guide to G-quadruplex ligands, Org. Biomol. Chem. 6 (2008) 627–636. doi:10.1039/b714772b.

[216] E. Izbicka, R.T. Wheelhouse, E. Raymond, K.K. Davidson, R.A. Lawrence, D. Sun, B.E. Windle, L.H. Hurley, D.D. Von Hoff, Effects of cationic porphyrins as G-quadruplex interactive agents in human tumor cells., Cancer Res. 59 (1999) 639–44. http://www.ncbi.nlm.nih.gov/pubmed/9973212 (accessed August 30, 2019).

[217] C.L. Grand, H. Han, R.M. Muñoz, S. Weitman, D.D. Von Hoff, L.H. Hurley, D.J. Bearss, The cationic porphyrin TMPyP4 down-regulates c-MYC and human telomerase reverse transcriptase expression and inhibits tumor growth in vivo., Mol. Cancer Ther. 1 (2002) 565–73. http://www.ncbi.nlm.nih.gov/pubmed/12479216 (accessed August 30, 2019).

[218] C. Pérez-Arnaiz, N. Busto, J. Santolaya, J.M. Leal, G. Barone, B. García, Kinetic evidence for interaction of TMPyP4 with two different G-quadruplex conformations of human telomeric DNA, Biochim. Biophys. Acta - Gen. Subj. 1862 (2018) 522–531. doi:10.1016/j.bbagen.2017.10.020.

[219] S.M. Gowan, J.R. Harrison, L. Patterson, M. Valenti, M.A. Read, S. Neidle, L.R. Kelland, A G-quadruplex-interactive potent small-molecule inhibitor of telomerase exhibiting in vitro and in vivo antitumor activity., Mol. Pharmacol. 61 (2002) 1154–62. doi:10.1124/mol.61.5.1154.

[220] A.M. Burger, F. Dai, C.M. Schultes, A.P. Reszka, M.J. Moore, J.A. Double, S. Neidle, The G-Quadruplex-Interactive Molecule BRACO-19 Inhibits Tumor Growth, Consistent with Telomere Targeting and Interference with Telomerase Function, Cancer Res. 65 (2005) 1489–1496. doi:10.1158/0008-5472.CAN-04-2910.

[221] G. Zhou, X. Liu, Y. Li, S. Xu, C. Ma, X. Wu, Y. Cheng, Z. Yu, G. Zhao, Y. Chen, Telomere targeting with a novel G-quadruplex-interactive ligand BRACO-19 induces T-loop disassembly and telomerase displacement in human glioblastoma cells, Oncotarget. 7 (2016) 14925–39. doi:10.18632/oncotarget.7483.

[222] F.-C. Huang, C.-C. Chang, J.-M. Wang, T.-C. Chang, J.-J. Lin, Induction of senescence in cancer cells by the G-quadruplex stabilizer, BMVC4, is independent of its telomerase inhibitory activity., Br. J. Pharmacol. 167 (2012) 393–406. doi:10.1111/j.1476-5381.2012.01997.x.

[223] R. Rodriguez, S. Müller, J.A. Yeoman, C. Trentesaux, J.-F. Riou, S. Balasubramanian, A novel small molecule that alters shelterin integrity and triggers a DNA-damage response at telomeres., J. Am. Chem. Soc. 130 (2008) 15758–9. doi:10.1021/ja805615w.

[224] J.F. Moruno-Manchon, E.C. Koellhoffer, J. Gopakumar, S. Hambarde, N. Kim, L.D. McCullough, A.S. Tsvetkov, The G-quadruplex DNA stabilizing drug pyridostatin promotes DNA damage and downregulates transcription of Brca1 in neurons., Aging (Albany. NY). 9 (2017) 1957–1970. doi:10.18632/aging.101282.

[225] M.-Y. Kim, H. Vankayalapati, K. Shin-ya, K. Wierzba, L.H. Hurley, Telomestatin, a Potent Telomerase Inhibitor That Interacts Quite Specifically with the Human Telomeric Intramolecular G-Quadruplex, J. Am. Chem. Soc. 124 (2002) 2098–2099. doi:10.1021/ja017308q.

[226] D. Monchaud, A. Granzhan, N. Saettel, A. Guédin, J.-L. Mergny, M.-P. Teulade-Fichou, “One Ring to Bind Them All”—Part I: The Efficiency of the Macrocyclic Scaffold for G-Quadruplex DNA Recognition, J. Nucleic Acids. 2010 (2010). doi:10.4061/2010/525862.

[227] B. Machireddy, G. Kalra, S. Jonnalagadda, K. Ramanujachary, C. Wu, Probing the Binding Pathway of BRACO19 to a Parallel-Stranded Human Telomeric G-Quadruplex Using Molecular Dynamics Binding Simulation with AMBER DNA OL15 and Ligand GAFF2 Force Fields, J. Chem. Inf. Model. 57 (2017) 2846–2864. doi:10.1021/acs.jcim.7b00287.

[228] D. Drygin, A. Siddiqui-Jain, S. O’Brien, M. Schwaebe, A. Lin, J. Bliesath, C.B. Ho, C. Proffitt, K. Trent, J.P. Whitten, J.K.C. Lim, D. Von Hoff, K. Anderes, W.G. Rice, Anticancer Activity of CX-3543: A Direct Inhibitor of rRNA Biogenesis, Cancer Res. 69 (2009) 7653–7661. doi:10.1158/0008-5472.CAN-09-1304.

[229] S. Asamitsu, S. Obata, Z. Yu, T. Bando, H. Sugiyama, Recent Progress of Targeted G-Quadruplex-Preferred Ligands Toward Cancer Therapy., Molecules. 24 (2019). doi:10.3390/molecules24030429.

[230] T.A. Brooks, L.H. Hurley, Targeting MYC Expression through G-Quadruplexes, Genes Cancer. 1 (2010) 641–649. doi:10.1177/1947601910377493.

[231] S. Müller, D.A. Sanders, M. Di Antonio, S. Matsis, J.-F. Riou, R. Rodriguez, S. Balasubramanian, Pyridostatin analogues promote telomere dysfunction and long-term growth inhibition in human cancer cells., Org. Biomol. Chem. 10 (2012) 6537–46. doi:10.1039/c2ob25830g.

[232] E. Lazzerini-Denchi, A. Sfeir, Stop pulling my strings-what telomeres taught us about the DNA damage response, Nat. Rev. Mol. Cell Biol. 17 (2016) 364–378. doi:10.1038/nrm.2016.43.

[233] L.-N. Zhu, S.-J. Zhao, B. Wu, X.-Z. Li, D.-M. Kong, A new cationic porphyrin derivative (TMPipEOPP) with large side arm substituents: a highly selective G-quadruplex optical probe., PLoS One. 7 (2012) e35586. doi:10.1371/journal.pone.0035586.

[234] M.-J. Cheng, Y.-G. Cao, TMPYP4 exerted antitumor effects in human cervical cancer cells

through activation of p38 mitogen-activated protein kinase., Biol. Res. 50 (2017) 24. doi:10.1186/s40659-017-0129-4.

[235] T. Wada, J.M. Penninger, Mitogen-activated protein kinases in apoptosis regulation, Oncogene. 23 (2004) 2838–2849. doi:10.1038/sj.onc.1207556.

[236] X. Sui, N. Kong, L. Ye, W. Han, J. Zhou, Q. Zhang, C. He, H. Pan, p38 and JNK MAPK pathways control the balance of apoptosis and autophagy in response to chemotherapeutic agents, Cancer Lett. 344 (2014) 174–179. doi:10.1016/j.canlet.2013.11.019.

[237] X.-H. Zheng, X. Nie, H.-Y. Liu, Y.-M. Fang, Y. Zhao, L.-X. Xia, TMPyP4 promotes cancer cell migration at low doses, but induces cell death at high doses, Sci. Rep. 6 (2016) 26592. doi:10.1038/srep26592.

[238] N. Konieczna, A. Romaniuk-Drapała, N. Lisiak, E. Totoń, A. Paszel-Jaworska, M. Kaczmarek, B. Rubiś, Telomerase Inhibitor TMPyP4 Alters Adhesion and Migration of Breast-Cancer Cells MCF7 and MDA-MB-231., Int. J. Mol. Sci. 20 (2019). doi:10.3390/ijms20112670.

[239] P. Chilka, N. Desai, B. Datta, Small Molecule Fluorescent Probes for G- Quadruplex Visualization as Potential Cancer Theranostic Agents, Molecules. 24 (2019) 752. doi:10.3390/molecules24040752.

[240] C. Schaffitzel, I. Berger, J. Postberg, J. Hanes, H.J. Lipps, A. Pluckthun, In vitro generated antibodies specific for telomeric guanine-quadruplex DNA react with Stylonychia lemnae macronuclei, Proc. Natl. Acad. Sci. 98 (2001) 8572–8577. doi:10.1073/pnas.141229498.

[241] G. Biffi, D. Tannahill, J. McCafferty, S. Balasubramanian, Quantitative visualization of DNA G-quadruplex structures in human cells., Nat. Chem. 5 (2013) 182–6. doi:10.1038/nchem.1548.

[242] G. Biffi, M. Di Antonio, D. Tannahill, S. Balasubramanian, Visualization and selective chemical targeting of RNA G-quadruplex structures in the cytoplasm of human cells, Nat. Chem. 6 (2014) 75–80. doi:10.1038/nchem.1805.

[243] A. Henderson, Y. Wu, Y.C. Huang, E.A. Chavez, J. Platt, F.B. Johnson, R.M. Brosh, D. Sen, P.M. Lansdorp, P.M. Lansdorp, Detection of G-quadruplex DNA in mammalian cells., Nucleic Acids Res. 42 (2014) 860–9. doi:10.1093/nar/gkt957.

[244] A. Henderson, Y. Wu, Y.C. Huang, E.A. Chavez, J. Platt, F.B. Johnson, R.M. Brosh, D. Sen, P.M. Lansdorp, P.M. Lansdorp, Detection of G-quadruplex DNA in mammalian cells., Nucleic Acids Res. 45 (2017) 6252. doi:10.1093/nar/gkx300.

[245] H.G. Kazemier, K. Paeschke, P.M. Lansdorp, Guanine quadruplex monoclonal antibody 1H6 cross-reacts with restrained thymidine-rich single stranded DNA., Nucleic Acids Res. 45 (2017) 5913–5919. doi:10.1093/nar/gkx245.

[246] E. Largy, A. Granzhan, F. Hamon, D. Verga, M.-P. Teulade-Fichou, Visualizing the quadruplex: from fluorescent ligands to light-up probes., Top. Curr. Chem. 330 (2013) 111–77. doi:10.1007/128_2012_346.

[247] M.I. Umar, D. Ji, C.Y. Chan, C.K. Kwok, G-quadruplex-based fluorescent turn-on ligands and aptamers: From development to applications, 2019. doi:10.3390/molecules24132416.

[248] C.K. Kwok, C.J. Merrick, G-Quadruplexes: Prediction, Characterization, and Biological Application., Trends Biotechnol. 35 (2017) 997–1013. doi:10.1016/j.tibtech.2017.06.012.

[249] D. Hernandez-Verdun, P. Roussel, M. Thiry, V. Sirri, D.L.J. Lafontaine, The nucleolus: Structure/function relationship in RNA metabolism, Wiley Interdiscip. Rev. RNA. 1 (2010) 415–

431. doi:10.1002/wrna.39.

[250] Y.W. Lam, L. Trinkle-Mulcahy, New insights into nucleolar structure and function., F1000Prime Rep. 7 (2015) 48. doi:10.12703/P7-48.

[251] S. Zhang, H. Sun, H. Chen, Q. Li, A. Guan, L. Wang, Y. Shi, S. Xu, M. Liu, Y. Tang, Direct visualization of nucleolar G-quadruplexes in live cells by using a fluorescent light-up probe, Biochim. Biophys. Acta - Gen. Subj. 1862 (2018) 1101–1106. doi:10.1016/j.bbagen.2018.01.022.

[252] S. Xu, Q. Li, J. Xiang, Q. Yang, H. Sun, A. Guan, L. Wang, Y. Liu, L. Yu, Y. Shi, H. Chen, Y. Tang, Thioflavin T as an efficient fluorescence sensor for selective recognition of RNA G-quadruplexes, Sci. Rep. 6 (2016) 24793. doi:10.1038/srep24793.

[253] A. Laguerre, K. Hukezalie, P. Winckler, F. Katranji, G. Chanteloup, M. Pirrotta, J.-M. Perrier-Cornet, J.M.Y. Wong, D. Monchaud, Visualization of RNA-Quadruplexes in Live Cells, J. Am. Chem. Soc. 137 (2015) 8521–8525. doi:10.1021/jacs.5b03413.

[254] A. Laguerre, J.M.Y. Wong, D. Monchaud, Direct visualization of both DNA and RNA quadruplexes in human cells via an uncommon spectroscopic method, Sci. Rep. 6 (2016) 1–10. doi:10.1038/srep32141.

[255] O. Domarco, D. Lötsch, J. Schreiber, C. Dinhof, S. Van Schoonhoven, M.D. García, C. Peinador, B.K. Keppler, W. Berger, A. Terenzi, Self-assembled Pt2L2 boxes strongly bind G-quadruplex DNA and influence gene expression in cancer cells., Dalton Trans. 46 (2017) 329–332. doi:10.1039/c6dt03876j.

[256] T. Mosmann, Rapid colorimetric assay for cellular growth and survival: Application to proliferation and cytotoxicity assays, J. Immunol. Methods. 65 (1983) 55–63. doi:10.1016/0022-1759(83)90303-4.

[257] Cell Viability and Proliferation Assays | Sigma-Aldrich, (n.d.). https://www.sigmaaldrich.com/technical-documents/articles/biofiles/cell-viability-and-proliferation.html?utm_source=Google&utm_medium=cpc&utm_campaign=CellBio - Stem Cells - SIAL&utm_content=Cell Viability and Proliferation&gclid=Cj0KCQjw1 (accessed March 16, 2018).

[258] T. Riss, R. Moravecs, A. Niles, S. Duellman, H. Benink, T. Worzella, L. Minor, Cell viability assays, Assay Guid. Man. (2016) 1–31. doi:10.1016/j.acthis.2012.01.006.

[259] T.T. Puck, P.I. Marcus, Action of x-rays on mammalian cells., J. Exp. Med. 103 (1956) 653–66. http://www.ncbi.nlm.nih.gov/pubmed/13319584 (accessed March 16, 2018).

[260] H. Rafehi, C. Orlowski, G.T. Georgiadis, K. Ververis, A. El-Osta, T.C. Karagiannis, Clonogenic assay: adherent cells., J. Vis. Exp. (2011). doi:10.3791/2573.

[261] Getting Started with FlowJo | FlowJo, LLC, (n.d.). https://www.flowjo.com/learn/flowjo-university/flowjo/getting-started-with-flowjo/58 (accessed March 16, 2018).

[262] Fluorescence Assisted Cell Sorting (FACS) - Diamantina Institute - University of Queensland, (n.d.). https://di.uq.edu.au/community-and-alumni/sparq-ed/sparq-ed-services/fluorescence-assisted-cell-sorting-facs (accessed March 16, 2018).

[263] Flow cytometry introduction | Abcam, (n.d.). http://www.abcam.com/protocols/introduction-to-flow-cytometry (accessed March 16, 2018).

[264] K.H. Kim, J.M. Sederstrom, Assaying Cell Cycle Status Using Flow Cytometry., Curr. Protoc.

Mol. Biol. 111 (2015) 28.6.1–11. doi:10.1002/0471142727.mb2806s111.

[265] Z. Darzynkiewicz, H.D. Halicka, H. Zhao, Analysis of cellular DNA content by flow and laser scanning cytometry., Adv. Exp. Med. Biol. 676 (2010) 137–47. http://www.ncbi.nlm.nih.gov/pubmed/20687474 (accessed March 19, 2018).

[266] Propidium Iodide, (n.d.). https://www.thermofisher.com/at/en/home/life-science/cell-analysis/fluorophores/propidium-iodide.html (accessed March 19, 2018).

[267] U. Prabhakar, M. Kelley, Wiley InterScience (Online service), Validation of cell-based assays in the GLP setting : a practical guide, Wiley, 2008. https://books.google.at/books?id=Tg1WTIMgXbkC&pg=PA78&lpg=PA78&dq=PI+intercalates+into+DNA&source=bl&ots=UOc5sW_LFR&sig=dJ_fD5shUyn9LG5OsyLJr04wRII&hl=de&sa=X&ved=0ahUKEwicusGOjPjZAhUD2SwKHYvND9QQ6AEIVDAE#v=onepage&q=PI intercalates into DNA&f=false (accessed March 19, 2018).

[268] Propidium Iodide Flow Cytometry Kit for Cell Cycle Analysis Instructions for Use, (n.d.). http://www.abcam.com/ps/products/139/ab139418/documents/ab139418_Propidium Iodide Flow Cytometry Kit_Booklet_djs_08-Oct-2012 v2 (website).pdf (accessed March 19, 2018).

[269] J. Walker-Daniels, Live Cell Imaging Methods Review, Mater. Methods. 2 (2012). doi:10.13070/mm.en.2.124.

[270] Preparing for Live-Cell Imaging, (n.d.). https://www.thermofisher.com/at/en/home/life-science/cell-analysis/cell-analysis-learning-center/molecular-probes-school-of-fluorescence/imaging-basics/sample-considerations/live-cell-imaging.html (accessed March 22, 2018).

[271] J. Icha, M. Weber, J.C. Waters, C. Norden, Phototoxicity in live fluorescence microscopy, and how to avoid it, BioEssays. 39 (2017) 1700003. doi:10.1002/bies.201700003.

[272] H. Shroff, P.P. Laissue, R.A. Alghamdi, P. Tomancak, E.G. Reynaud, Assessing phototoxicity in live fluorescence imaging, Nat. Methods. 14 (2017). doi:10.1038/nmeth.4344.

[273] A. Nwaneshiudu, C. Kuschal, F.H. Sakamoto, R. Rox Anderson, K. Schwarzenberger, R.C. Young, Introduction to Confocal Microscopy, J. Invest. Dermatol. 132 (2012) 1–5. doi:10.1038/jid.2012.429.

[274] Ucla Brain Research Institute Microscopy Core Facilities, The Confocal Microscope, (n.d.). http://www.gonda.ucla.edu/bri_core/confocal.htm (accessed March 26, 2018).

[275] ZEISS LSM700 Confocal Microscope (Room #108), (n.d.). https://krebsforschung.meduniwien.ac.at/intranet/technik-edv/mikroskope/zeiss-lsm700-confocal-microscope-room-108/ (accessed March 27, 2018).

[276] Confocal Laser Scanning Microscope (CLSM) — Uni Oldenburg, (n.d.). https://www.uni-oldenburg.de/en/chemistry/physical-chemistry-wittstock/seiten/confocal-laser-scanning-microscope-clsm/ (accessed March 27, 2018).

[277] Introduction to Confocal Laser Scanning Microscopy (LEICA), (n.d.). https://www.umassmed.edu/globalassets/maps/documents/confocal-explanation.pdf (accessed March 26, 2018).

[278] University of Rhode Island, Imaging, (n.d.). https://web.uri.edu/gsc/imaging/ (accessed March 27, 2018).

[279] Confocal Imaging Modes | MicroscopyU, (n.d.). https://www.microscopyu.com/techniques/confocal/confocal-imaging-modes#olhead12 (accessed March 27, 2018).

[280] Chromosome Biology - Rudi Appels, R. Morris, Bikram S. Gill, C. E. May - Google Books, (n.d.). https://books.google.at/books?id=7OXTBwAAQBAJ&pg=PA37&lpg=PA37&dq=metaphase+chromosomes+Colchicum+autumnale+(autumn+crocus&source=bl&ots=f_vLNHW-P_&sig=TQ9_BIqJnI-oVHthW9GiPocRVSw&hl=de&sa=X&ved=0ahUKEwi-x_egzYnaAhVCCCwKHQq9Dt8Q6AEIWjAK#v=onepage&q=metaph (accessed March 26, 2018).

[281] S.K. Bardal, J.E. Waechter, D.S. Martin, S.K. Bardal, J.E. Waechter, D.S. Martin, Chapter 20 – Neoplasia, Appl. Pharmacol. (2011) 305–324. doi:10.1016/B978-1-4377-0310-8.00020-8.

[282] V. Oestergaard, Immunostaining of Formaldehyde-fixed Metaphase Chromosome from Untreated and Aphidicolin-treated DT40 Cells, BIO-PROTOCOL. 7 (2017). doi:10.21769/BioProtoc.2259.

[283] U. Claussen, S. Michel, P. Mühlig, M. Westermann, U.-W. Grummt, K. Kromeyer-Hauschild, T. Liehr, Demystifying chromosome preparation and the implications for the concept of chromosome condensation during mitosis, Cytogenet. Genome Res. 98 (2002) 136–146. doi:10.1159/000069817.

[284] R. Thavarajah, V.K. Mudimbaimannar, J. Elizabeth, U.K. Rao, K. Ranganathan, Chemical and physical basics of routine formaldehyde fixation., J. Oral Maxillofac. Pathol. 16 (2012) 400–5. doi:10.4103/0973-029X.102496.

[285] Thermo Fisher Scientific, Fixation Strategies and Formulations, (n.d.). https://www.thermofisher.com/at/en/home/life-science/protein-biology/protein-biology-learning-center/protein-biology-resource-library/pierce-protein-methods/fixation-strategies-formulations.html (accessed March 28, 2018).

[286] Aldehyde fixation and its mechanism | I am a novice, (n.d.). https://iamanovice.wordpress.com/2014/02/16/aldehyde-fixation-and-its-mechanism/ (accessed March 28, 2018).

[287] Aldehyde Fixatives | National Diagnostics, (n.d.). https://www.nationaldiagnostics.com/histology/article/aldehyde-fixatives (accessed March 28, 2018).

[288] Cell Signaling Technology, A guide to successful immunofluorescene, (2014). http://media.cellsignal.com/www/pdfs/resources/product-literature/application-if-brochure.pdf (accessed March 28, 2018).

[289] P. Held, Key Tips on Sample Preparation for Immunofluorescence | Biocompare Bench Tips, (2016). https://www.biocompare.com/Bench-Tips/184672-Key-Tips-on-Sample-Preparation-for-Immunofluorescence/ (accessed March 28, 2018).

[290] P. Held, Sample Preparation for Fluorescence Microscopy: An Introduction Concepts and Tips for Better Fixed Sample Imaging Results Cell Fixation, (n.d.). www.biotek.com (accessed March 28, 2018).

[291] Comparing fixing agents: methanol vs acetone for IF | CiteAb Blog, (n.d.). https://blog.citeab.com/comparing-fixing-agents/ (accessed March 28, 2018).

[292] Thermo Fisher Scientific, Physical Properties That Define Fluorescence, (n.d.). https://www.thermofisher.com/at/en/home/life-science/cell-analysis/cell-analysis-learning-

center/molecular-probes-school-of-fluorescence/imaging-basics/fundamentals-of-fluorescence-microscopy/physical-properties-that-define-fluorescence.html (accessed April 3, 2018).

[293] Invitrogen by Thermo Fisher Scientific, Anatomy of Fluorescence Spectra, (n.d.). https://www.thermofisher.com/at/en/home/life-science/cell-analysis/cell-analysis-learning-center/molecular-probes-school-of-fluorescence/fluorescence-basics/anatomy-fluorescence-spectra.html (accessed April 3, 2018).

[294] J.R. Lakowicz, Fluorophores, in: Princ. Fluoresc. Spectrosc., Springer US, Boston, MA, 2006: pp. 63–95. doi:10.1007/978-0-387-46312-4_3.

[295] Sigma-Aldrich, DAPI 4',6-Diamidino-2-phenylindole, (n.d.). https://www.sigmaaldrich.com/content/dam/sigma-aldrich/docs/Sigma/Product_Information_Sheet/d8417pis.pdf (accessed April 3, 2018).

[296] Thermo Fisher Scientific, DAPI (4',6-Diamidino-2-Phenylindole, Dihydrochloride), (n.d.). https://www.thermofisher.com/order/catalog/product/D1306 (accessed April 3, 2018).

[297] Molecular Probes, SYTO RNASelect™ Green Fluorescent Cell Stain, (2004). https://assets.thermofisher.com/TFS-Assets/LSG/manuals/mp32703.pdf (accessed April 3, 2018).

[298] Carl Zeiss Microscopy, Spectral Separation of Multifluorescence Labels with the LSM 510 META, (n.d.). http://www.well.ox.ac.uk/_asset/file/spectral-seperation-with-510-meta.pdf (accessed April 18, 2018).

[299] J.M. Larson, S.A. Schwartz, A.M. Rainey, M.W. Davidson, Lambda Stacks and Spectral Signatures | MicroscopyU, (n.d.). https://www.microscopyu.com/tutorials/lambda-stacks-and-spectral-signatures (accessed April 18, 2018).

[300] T.B. Gines, M.W. Davidson, Emission Fingerprinting with Lambda Stacks, (n.d.). http://zeiss-campus.magnet.fsu.edu/tutorials/spectralimaging/lambdastack/indexflash.html (accessed April 18, 2018).

[301] G. McNamara, J.M. Larson, S.A. Schwartz, M.W. Davidson, Spectral Imaging and Linear Unmixing | MicroscopyU, (n.d.). https://www.microscopyu.com/techniques/confocal/spectral-imaging-and-linear-unmixing (accessed April 18, 2018).

[302] Direct vs indirect immunofluorescence | Abcam, (n.d.). http://www.abcam.com/secondary-antibodies/direct-vs-indirect-immunofluorescence (accessed March 29, 2018).

[303] Thermo Fisher Scientific, Immunolabeling, (n.d.). http://www.thermofisher.com/at/en/home/life-science/cell-analysis/cell-analysis-learning-center/molecular-probes-school-of-fluorescence/imaging-basics/labeling-your-samples/immunolabeling.html (accessed April 11, 2018).

[304] A. Allaire, F. Picard-Jean, M. Bisaillon, Immunofluorescence to Monitor the Cellular Uptake of Human Lactoferrin and its Associated Antiviral Activity Against the Hepatitis C Virus., J. Vis. Exp. (2015). doi:10.3791/53053.

[305] Fixation and Permeabilization in ICC IF: Novus Biologicals, (n.d.). https://www.novusbio.com/support/fixation-and-permeabilization-in-icc-if (accessed March 29, 2018).

[306] J. Redig, Immunohistochemistry Basics: Blocking Non-Specific Staining - Bitesize Bio, (n.d.). https://bitesizebio.com/13466/immunohistochemistry-basics-blocking-non-specific-staining/ (accessed March 29, 2018).

[307] Thermo Fisher Scientific, Blocking Strategies for IHC, (n.d.). https://www.thermofisher.com/at/en/home/life-science/protein-biology/protein-biology-learning-center/protein-biology-resource-library/pierce-protein-methods/blocking-strategies-ihc.html (accessed March 29, 2018).

[308] A.L. Tarca, R. Romero, S. Draghici, Analysis of microarray experiments of gene expression profiling., Am. J. Obstet. Gynecol. 195 (2006) 373–88. doi:10.1016/j.ajog.2006.07.001.

[309] Promega, M-MLV Reverse Transcriptase, (n.d.). https://at.promega.com/-/media/files/resources/protocols/product-information-sheets/g/m-mlv-reverse-transcriptase-protocol.pdf (accessed April 9, 2018).

[310] Sigma-Aldrich, Reverse Transcription - PCR Technologies Guide, (n.d.). https://www.sigmaaldrich.com/technical-documents/articles/biology/reverse-transcription.html (accessed April 9, 2018).

[311] Scitable by Nature Education, microarray, (2014). https://www.nature.com/scitable/definition/microarray-202 (accessed April 5, 2018).

[312] Y. Grigoryev, Introduction to DNA Microarrays - Bitesize Bio, (n.d.). https://bitesizebio.com/7206/introduction-to-dna-microarrays/ (accessed April 5, 2018).

[313] Agilent Technologies, One-Color Microarray-Based Expression Analyses, 2015. http://www.agilent.com/genomics/protocolvideos. (accessed April 9, 2018).